ENERGY-BASED AND MICROMECHANICS MODELS ON THE PREDICTION OF DISTRESSES IN FLEXIBLE PAVEMENTS

A Dissertation

by

YADONG GUO

Submitted to the Graduate and Professional School of
Texas A&M University
in partial fulfillment of the requirements for the degree of

DOCTOR OF PHILOSOPHY

Chair of Committee,	Bjorn Birgisson
Co-Chair of Committee,	Dallas Little
Committee Members,	Goong Chen
	Marcelo-Javier Sanchez Castilla
Head of Department,	Zachary Grasley

May 2023

Major Subject: Civil Engineering

ABSTRACT

Flexible pavements consist of the asphalt concrete layer, base layer and subbase layer, and these three layers are made of asphalt concrete, unbound granular aggregates and compacted soils, respectively. In flexible pavements, there are two main distresses, fatigue cracking and rutting. Fatigue cracking only happens in the asphalt concrete layer, while rutting can occur in every layer. The distress development is related to the material properties in each layer.

In Chapters 2-4, three energy-based models are proposed to predict the fatigue cracking in asphalt concrete and plastic deformation in asphalt concrete and unbound granular aggregates. In the fatigue cracking model, the damage evolution is connected with the mass specific volume of asphalt concrete, so the model is independent of the reference configuration. In the rutting model for asphalt concrete, the proposed model is incorporated into a framework. In this framework, the mechanical properties of asphalt concrete can be obtained from its microstructure and properties of its components. The effects of temperature, aging and seasonal changing of rutting resistance are considered. In the rutting model for unbound granular aggregates, the effects of moisture and microstructure of the material are considered. By doing numerical simulation and comparing model predictions with test data, the proposed models can capture the distress development accurately.

In the fifth chapter, a micromechanics model for soils is proposed to predict the soil-water characteristic curve (SWCC), and this curve plays an important role on the

prediction of soils' performance. The proposed model can account for the adsorption and capillary contributions on the accumulation of water in soils. The contact angle hysteresis is considered to capture the SWCC hysteresis, and the concept of equivalent grain radius is proposed to consider the effect of grain-size distribution. Every parameter in the model has a clear physical meaning and is measurable easily. The proposed model can capture the SWCC well, and model predictions show that positive and negative matric suction contribute to the shrinkage and swelling of expansive soils respectively.

The last chapter summarizes the main findings.

ACKNOWLEDGEMENTS

I would like to thank my committee chair, Dr. Bjorn Birgisson, for his guidance and support throughout the course of this research. Without his guidance, I could have not finished this work. It has been a great pleasure to work with him. I also want to extend my gratitude to my committee co-chair, Dr. Dallas Little, and committee members, Dr. Goong Chen and Dr. Marcelo-Javier Sanchez Castilla, for their insightful comments and feedback on my research.

Thanks also go to my friends and colleagues and the college faculty and staff for making my time at Texas A&M University a great experience. By taking classes, I increased my knowledge and learnt some teaching methods. By working as a graduate teaching assistant, I had opportunities to use these teaching methods and found the fun of teaching. The experiences in these four years are memorable, and they make me better and smarter.

Finally, thanks to my mother and father for their encouragement and love.

CONTRIBUTORS AND FUNDING SOURCES

Contributors

This work was supervised by a thesis (or) dissertation committee consisting of Professors Bjorn Birgisson (advisor), Dallas Little (co-advisor) and Marcelo-Javier Sanchez Castilla of the Zachry Department of Civil and Environmental Engineering and Professor Goong Chen of the Department of Mathematics.

Funding Sources

This work was made possible in part by Texas Department of Transportation under Grant Number (0-7124). Its contents are solely the responsibility of the author and do not necessarily represent the official views of Texas Department of Transportation.

TABLE OF CONTENTS

Page

LIST OF FIGURES

Page

LIST OF TABLES

Page

1. INTRODUCTION

The structure of a flexible pavement usually consists of three layers, the asphalt concrete layer, base layer and subgrade layer, as shown in Figure 1.1. These three layers are made of asphalt concrete, unbound granular materials and compacted soil, respectively. Fatigue damage and rutting are two main distresses in flexible pavements, and the distress development is related to the material properties in each layer. Fatigue cracking only happens in the asphalt concrete layer, while rutting can occur in each layer of the pavement. The development of these distresses is seasonal dependent, because asphalt concrete is temperature dependent. During summer, due to high temperature, asphalt concrete is soft, so it can bear less stress and transfer more stress into sublayers, and high stress in each layer can cause rutting. During winter, due to low temperature, asphalt concrete is stiff, so it can sustain more stress and transfer less stress to sublayers, and large stress in the asphalt concrete layer can cause fatigue cracking. Accurate prediction of these distresses plays an important role in the decision making about pavement design, maintenance and rehabilitation [1-5].

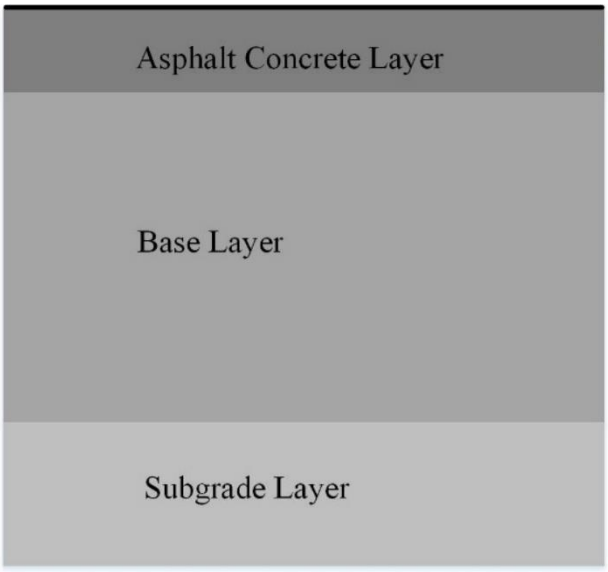

Figure 1.1 Typical cross section of flexible pavements.

To predict the rutting and fatigue cracking in pavements, many stress or strain based models are proposed. However, the main drawback of these models is that they are not independent of loading modes, and the parameter values determined from controlled-stress tests may not be applied to the prediction of material behavior under controlled-strain loading. For example, if there are two asphalt concrete mixtures, and one has a high stiffness while the other has a low stiffness. Under the same controlled-stress loading, the mixture with a high stiffness suffers higher strain, so it fails ealier than the mixture with a low stiffness. Similarly, under the same controlled-strain loading, the mixture with a low stiffness suffers higher stress, so it fails ealier than the mixture with a high stiffness. Stress-based models may not be able to capture the performance difference of these two mixtures under controlled-stress loading, and strain-based models may not be able to capture the

performance difference of these two mixtures under controlled-strain loading. Therefore, the distress development is related to both the stress level and the strain level. Compared with stress or strain based models, the energy based model can consider the effect of loading modes.

The soil-water characteristic curve (SWCC) plays an important role on the prediction of soil performance. However, most existing SWCC models contains empirical parameters and these parameters do not have clear physical meanings. This may cause that soils with different components or gradation may correspond to different parameter values. Therefore, these model may performs well on the fitting of SWCC, they cannot be used to do accurate prediction.

1.1. Research objectives

The objectives of this research are as follows:

(1) To predict fatigue cracking in asphalt concrete, a new mass specific volume-based viscoelastic damage model will be proposed. This model can be independent of the choice of reference configuration and consider the change of material resistance to damage under destructive loading.

(2) To predict the plastic deformation in asphalt concrete, a new energy-based plasticity model is proposed and incorporated in a predictive framework. The mechanical properties of asphalt concrete can be obtained based on its microstructure and properties of its components. The effects of temperature, loading frequencies and aging can be considered.

(3) To predict the plastic deformation in unbound granular aggregates, a new energy-based plasticity model is proposed. This model can consider the effect of the material structure on the material performance. The coordination number of the primary load-carrying structure will be included to predict the evolution of the plasticity resistance.

(4) To predict the soil-water characteristic curve (SWCC), a new micromechanics model is proposed. In the model, the adsorptive and capillary contributions on the accumulation of water in soils will be considered. Every parameter will have a clear physical meaning and can be measured easily, so the model will perform well on the accurate prediction of SWCC. The model can consider the effect of microstructure and gradation of soils. It can also capture the SWCC hysteresis arising from the contact angle hysteresis.

1.2. References

[1] M. Tia, B. Ruth, B. Birgisson, Influence of Aggregate Characteristics on Asphalt Mixture Properties and Performance, Bearing Capacity of Roads, Railways and Airfields, CRC Press2020, pp. 943-953.

[2] I. Onifade, B. Birgisson, Improved models for the prediction of asphalt binder dynamic shear modulus and phase angle, Construction and Building Materials 250 (2020) 118753.

[3] I. Onifade, K. Huang, B. Birgisson, Evaluation of models for binder dynamic shear modulus and phase angle, Advances in Materials and Pavement Performance Prediction II, CRC Press2020, pp. 462-466.

[4] D. Zhang, B. Birgisson, X. Luo, A new dynamic modulus predictive model for asphalt mixtures based on the law of mixtures, Construction and Building Materials 255 (2020) 119348.

[5] X. Luo, F. Ma, B. Birgisson, Z. Huang, Coupled mechanical and kinetic modeling of recovery in asphalt mixtures, Construction and Building Materials 254 (2020) 118889.

2. A MASS SPECIFIC VOLUME-BASED VISCOELASTIC DAMAGE MODEL TO CHARACTERIZE FATIGUE DAMAGE IN ASPHALT MIXTURES[*]

2.1. Introduction

Fatigue cracking is one of the most common distresses in asphalt pavements and it only occurs in the asphalt concrete layer, if the base layer is not cement or asphalt stabilized. These cracks usually initiate from air voids and then propagate under traffic loading or a combination of traffic and environmentally induced loading. There are two types of fatigue cracking, bottom-up cracking and top-down cracking. Bottom-up cracking grows from the bottom of the asphalt concrete layer making its way upwards to the surface and lead to the pavement failure, while top-down cracking initiates at the surface and propagates downwards to the bottom. The majority of cracking reported in asphalt pavements has been found to be in the form of top-down fatigue cracking in many parts of the world [1-3]. To model damage evolution in asphalt mixtures, two approaches, fracture mechanics and continuum damage mechanics (CDM), are adopted widely.

In fracture mechanics, it is generally assumed that materials already have a flaw or a crack before the load is applied. Thus, it focuses on the study of material response arising from crack initiation and propagation, which are governed by some

[*] Guo, Yadong, Ibrahim Onifade, and Bjorn Birgisson. "A mass specific volume-based viscoelastic damage model to characterize fatigue damage in asphalt mixtures." *Construction and Building Materials* 325 (2022): 126729.

fracture criteria. In order to consider the composition of mixtures and account for some measurable physical damage phenomena like micro- and macrocracks, some researchers [4-6] proposed a finite element simulation method incorporated with cohesive zone models based on fracture mechanics to predict the cracking behavior of asphalt mixtures. In these methods, cohesive zone elements are embedded between solid elements to model crack propagation. The linear viscoelastic constitutive relationship is usually adopted for the solid elements, and the corresponding relaxation modulus is obtained by performing the creep test or frequency sweep test. For the cohesive zone element, its constitutive law, namely the relationship between the cohesive zone traction and the separation distance, is represented using an intrinsic or extrinsic cohesive zone model [7], and the corresponding fracture parameters are usually determined by performing some tests, like single-edge notched beam testing [8], tensile fracture testing [9] and semicircular bend testing [10]. However, there are some limitations with these methods. Firstly, the effect of the amount and distribution of microcracks in the asphalt concrete (HMA) layer on the cracking behavior need to be considered. There may be multiple microcracks distributed randomly in one cross section of the HMA layer. Their distribution may affect the layer behavior considerably and it is also time-consuming to build a finite element model containing such an amount of microcracks. In addition, it is hard to predict the crack propagation direction a priori. Current research mainly focuses on Mode I cracking, and assumes its propagation direction will not change, but in reality, its direction can be affected by adjacent cracks or air voids. For example, it has been shown that wing cracks exist

in asphalt mixtures under compression [11]. Thirdly, cohesive zone models are not time- and temperature-dependent. The performance of asphalt mixtures will be very different under different temperature and loading rates, so as part of the asphalt mixture, the cohesive zone should also be time- and temperature-dependent. Also, the fracture tests used to determine fracture properties are performed at low temperatures to reduce viscoelastic effects, and this may make the fracture parameters less representative of intermediate temperature fracture. Lastly, the cohesive fracture zone is microscopic, while the parameter determination test is performed in the macro level, so the parameters determined may not fully represent the fracture properties in the cohesive fracture zone.

Continuum damage mechanics (CDM) have been the most successful approaches in modelling the behavior of materials [12-17]. In CDM, the material is assumed to be an undamaged homogeneous continuum before the application of load, and some preexisting defects and air voids are not considered. The damage variable is defined as an internal state variable and it can cause stiffness reduction of the material, so even if the material is damaged, it is still a continuum but the stiffness is reduced. To characterize damage in asphalt mixtures, the extended elastic-viscoelastic correspondence principle [18] is also adopted widely and the pseudo-strain is introduced to eliminate the viscoelastic effect, so the viscoelastic damage problem can be reduced to a brittle damage problem. With the help of this correspondence principle, some researchers [19, 20] considered the existence of cracks in their CDM models, and the damage variable is defined as a function of surface energy, number

of cracks and other material properties. However, if new surfaces or boundaries form inside the body, then the body will not be a continuum, so these models do not comply with basic assumptions of CDM. Some stress or strain based CDM models [21-25] were also proposed to predict damage in asphalt mixtures. For example, Kachanov [26] expressed damage in terms of the applied stress. Cozzarelli and Bernasconi [27] and Lee et al [28] expressed the damage in terms of the creep strain. Darabi et al [29] defined damage as a function of total strain and effective driving force. However, this can lead to contradictions between different modes of loading, when the damage is expressed in terms of strain or stress. For instance, compared with a stiff mixture, a soft mixture will fail first under a controlled-stress test, because it experiences a larger deformation, but under controlled-strain test, the stiffer mixture will suffer higher stresses and fail first. Therefore, a material property that is independent of the loading mode, amplitude or rate should be used to characterize fatigue damage resistance of asphalt mixtures [30]. Krajcinovic and Lemaitre [31-33] proposed an energy-based damage law to describe the damage initiation and failure under monotonic and cyclic loading modes. The energy-based damage law unifies many particular damage modes such as ductile, creep, fatigue, quasi-brittle damage with the critical damage densities related to meso-crack initiation. This damage model was adapted and further extended for the damage characterization in viscoelastic asphalt concrete materials by Onifade et al [34, 35], where the damage evolution was obtained through an energy density-based damage surface and damage potential, so the damage variable could be expressed as a function of damage driving energy density and the corresponding

parameters could be obtained from a variety of fracture test geometries. In this formulation, the damage was assumed to be a function of strain, which is related to the choice the reference configuration. The ambiguity and subjectivity associated with the choice of the reference configuration may lead to a somewhat subjective evaluation of damage. In order to overcome this limitation, Murru et al [36, 37] defined damage directly as a function of density to predict damage, which is independent of the reference configuration.

The main objective of this paper is to present a new mass specific volume-based viscoelastic damage model which can be independent of the choice of reference configuration and consider the change of material resistance to damage under destructive loading, to predict the fatigue cracking in asphalt concrete or flexible pavements. In this work, it is assumed the deformation and rotation of asphalt concrete under loading are small, so small strain is used to represent the strain in the material.

The organization of this paper is as follows. In the next section, kinematics and balance laws are introduced briefly, and then the constitutive formulation proposed is presented. Next, tests and methods used to determine the model parameters are presented. Importantly, all the parameters, including the resistance to damage at the reference configuration, can be determined from the creep test data. In the following section, the validity of the proposed model is verified through modeling the material behavior observed from controlled-strain repeated direct tension (RDT) laboratory tests. This is followed by the modeling of a typical pavement under traffic loading to

illustrate the capacity of the model to simulate fatigue cracking in asphalt concrete pavements. Finally, some conclusions are summarized.

2.2. Preliminaries

2.2.1. Kinematics considerations

Let **x** and **X** denote the position of a typical point at the current configuration and reference configuration, respectively. Thus, the displacement of this particle can be expressed as

$$\mathbf{u} = \mathbf{x} - \mathbf{X} \tag{2.1}$$

and the corresponding displacement gradient is

$$\frac{\partial \mathbf{u}}{\partial \mathbf{X}} = \frac{\partial (\mathbf{x} - \mathbf{X})}{\partial \mathbf{X}} = \frac{\partial \mathbf{x}}{\partial \mathbf{X}} - \mathbf{I} = \mathbf{F} - \mathbf{I} \tag{2.2}$$

where **F** is named the deformation gradient and **I** is the identity tensor.

The left Cauchy-Green tensor and right Cauchy-Green tensor are expressed as:

$$\mathbf{B} = \mathbf{F}\mathbf{F}^{\mathbf{T}} \tag{2.3}$$

$$\mathbf{C} = \mathbf{F}^{\mathbf{T}}\mathbf{F} \tag{2.4}$$

The Almansi-Hamel strain and Green-St. Venant strain are defined respectively as:

$$\mathbf{e} = \frac{1}{2}(\mathbf{I} - \mathbf{B}^{-1}) = \frac{1}{2}[\frac{\partial \mathbf{u}}{\partial \mathbf{x}} + (\frac{\partial \mathbf{u}}{\partial \mathbf{x}})^T - (\frac{\partial \mathbf{u}}{\partial \mathbf{x}})^T \frac{\partial \mathbf{u}}{\partial \mathbf{x}}] \tag{2.5}$$

$$\mathbf{E} = \frac{1}{2}(\mathbf{C} - \mathbf{I}) = \frac{1}{2}[\frac{\partial \mathbf{u}}{\partial \mathbf{X}} + (\frac{\partial \mathbf{u}}{\partial \mathbf{X}})^T - (\frac{\partial \mathbf{u}}{\partial \mathbf{X}})^T \frac{\partial \mathbf{u}}{\partial \mathbf{X}}] \tag{2.6}$$

When the deformation and rotation are small, both strains can be approximated by small strain defined as follows:

$$\boldsymbol{\varepsilon} = \frac{1}{2}[\nabla \mathbf{u} + (\nabla \mathbf{u})^T] \tag{2.7}$$

2.2.2. Balance laws

The movement of a body must follow some basic physical laws, such as the balance of mass, linear momentum and angular momentum.

The balance law for mass can be expressed as

$$\frac{\partial \rho}{\partial t} + div(\rho \mathbf{v}) = 0 \tag{2.8}$$

where ρ is the mass density at current time, $\mathbf{v}$ is the velocity tensor, and $div(\ )$ is the divergence operator.

The balance law for linear momentum can be expressed as

$$\rho \frac{d\mathbf{v}}{dt} = div(\mathbf{T}) + \rho \mathbf{b} \tag{2.9}$$

where $\mathbf{T}$ is the Cauchy stress tensor and $\mathbf{b}$ is the body force tensor.

For the balance of angular momentum, if there are no body or surface couples, the balance law can be expressed as:

$$\mathbf{T}=\mathbf{T}^T \tag{2.10}$$

This means that the stress tensor should be symmetric.

However, the balance laws can be applied to any material and are insufficient to describe the mechanical behavior of any material. To complete the specification of the mechanical properties of a material, the constitutive equation is needed. Different

materials have different constitutive relationships, so constitutive equations serve to distinguish one material from another.

2.3. Viscoelastic damage constitutive model

The generalized Maxwell model is used to represent the mechanical behavior of most viscoelastic materials and it includes a time-independent part with long term equilibrium stiffness $\mathbf{E}_\infty$ and a series of time-dependent parts with different stiffness $\mathbf{E_i}$ and viscosities $\boldsymbol{\eta}_\mathbf{i}$. The total strain ($\boldsymbol{\varepsilon}$) is the sum of an elastic strain ($\boldsymbol{\varepsilon}_\mathbf{i}^\mathbf{e}$) and viscous strain ($\boldsymbol{\varepsilon}_\mathbf{i}^\mathbf{v}$). For the viscoelastic damage material, the Helmholtz free energy can be defined as [34]:

$$\psi = \frac{1}{2}(1-d)[\boldsymbol{\varepsilon} : \mathbf{E}_\infty : \boldsymbol{\varepsilon} + \sum_{i=1}^{n}(\boldsymbol{\varepsilon} - \boldsymbol{\varepsilon}_\mathbf{i}^\mathbf{v}) : \mathbf{E_i} : (\boldsymbol{\varepsilon} - \boldsymbol{\varepsilon}_\mathbf{i}^\mathbf{v})] \tag{2.11}$$

where d is the damage variable.

The stress can thus be expressed as

$$\boldsymbol{\sigma} = \frac{\partial \psi}{\partial \boldsymbol{\varepsilon}} = (1-d)[\mathbf{E}_\infty : \boldsymbol{\varepsilon} + \sum_{i=1}^{n}\mathbf{E_i} : (\boldsymbol{\varepsilon} - \boldsymbol{\varepsilon}_\mathbf{i}^\mathbf{v})] \tag{2.12}$$

For the generalized Maxwell model, it has such properties as bellow:

$$\begin{cases} \boldsymbol{\varepsilon} = \boldsymbol{\varepsilon}_\mathbf{i}^e + \boldsymbol{\varepsilon}_\mathbf{i}^\mathbf{v} \\ \mathbf{E_i} : \boldsymbol{\varepsilon}_\mathbf{i}^e = \boldsymbol{\eta}_\mathbf{i} : \dot{\boldsymbol{\varepsilon}}_\mathbf{i}^\mathbf{v} \end{cases} \tag{2.13}$$

Therefore, the relationship between the total strain and the viscous strain can be obtained as

$$\mathbf{E_i} : (\boldsymbol{\varepsilon} - \boldsymbol{\varepsilon}_\mathbf{i}^\mathbf{v}) = \boldsymbol{\eta}_\mathbf{i} : \dot{\boldsymbol{\varepsilon}}_\mathbf{i}^\mathbf{v} \tag{2.14}$$

When the material is under constant strain, the stress can be expressed as

$$\boldsymbol{\sigma} = (1-d)[\mathbf{E}_\infty : \boldsymbol{\varepsilon} + \sum_{i=1}^{n} \mathbf{E_i} e^{-t/\tau_i} : \boldsymbol{\varepsilon}] \tag{2.15}$$

where τ_i ($=\eta_i / E_i$) is the retardation time.

According to the thermodynamics, damage is work conjugate to its driving energy, and since damage can cause the dilatancy of materials, the driving energy of damage at a loading period $[t_1, t_2]$ is defined as below:

$$Y = \int_{t_1}^{t_2} \sigma_v \cdot \dot{v} dt \tag{2.16}$$

with

$$\sigma_v = \sqrt{\sigma_1^2 + \sigma_2^2 + \sigma_3^2} \tag{2.17}$$

where v is the mass specific volume and σ_i (i=1,2,3) are principal stresses.

Therefore, damage can be defined as a power function of the driving energy as follows:

$$d = k_1 (\frac{Y}{S})^{k_2} \tag{2.18}$$

where k_1 and k_2 are material constants and S is the resistance to damage and has the same unite as that of the driving energy.

Under loading the resistance to damage of materials decreases with the increase of damage, and damage can cause the dilatancy of the material, so damage can be expressed as a function of mass specific volume and at every mass specific

volume, the resistance to damage is unique. Here we express S as an exponential function of mass specific volume as below.

$$S = S_0 \cdot e^{-av} \tag{2.19}$$

with

$$v = \det \mathbf{F} \cdot v_R \approx [1 + tr(\boldsymbol{\varepsilon})] \cdot v_R \tag{2.20}$$

where S_0 corresponds to the resistance to damage when the mass specific volume approaches to 0, a is a material constant, v and v_R are the mass specific volumes at current and reference configurations respectively, det(**F**) is the determinant of deformation gradient and $tr(\cdot)$ means trace of a matrix.

Therefore, the damage evolution function can be expressed as

$$\dot{d} = k_1 k_2 (YS^{-1})^{k_2 - 1} (\dot{Y}S^{-1} - YS^{-2}\dot{S}) \tag{2.21}$$

2.4. Materials and testing

Two types of asphalt mixtures were tested, designated as Nustar and Valero mixtures, respectively. Each type of mixture was laboratory prepared and compacted. These two mixtures use different types of asphalt binders, Nustar binder and Valero binder respectively, but use the same aggregate. The aggregate consists of Hanson limestone shipped from New Braunfels, Texas and it satisfies the specification requirements of Texas Department of Transportation (TxDOT). The gradation of the aggregate was determined based on a Type C (coarse surface) dense gradation specifies by TxDOT. The mixtures were mixed following the same mixture design procedure specified by TxDOT. Cylindrical specimens with 152 mm in diameter and 178 mm in height were cast, from which cylindrical cores of 102 mm diameter were

extracted to ensure that the specimen is homogeneous. The cores were then cut to lengths of 150 mm to remove irregularity. The target air void contents are 4.0% and 7.0%.

Two types tests, the creep test and controlled-strain repeated direct tension (RDT) test, were performed on these specimens, and the creep test is a part of the creep and step-loading recovery (CSR) test. For the creep test, a nondestructive test with a constant low load level was performed first to obtain the material properties, like the creep compliance, and then a destructive test with a high load level was performed on the same specimen to study the mechanical behavior of the damaged material. For the RDT test, a destructive RDT test was performed on these undamaged specimens, and the loading frequency is 1 Hz.

These tests were performed using the Material Test System (MTS) on unaged specimens at different temperature, including 10 ºC, 20ºC and 30 ºC. The specimen is glued to a pair of end-caps through which the tensile load is applied. To apply a pure direct load while avoiding possible bending moment to the specimen, the loading frame of the MTS should be aligned. Three axial linear variable differential transformers (LVDTs) are mounted 120 degrees apart around the specimen surface to measure the axial deformation of the specimen. The gage length of the axial LVDT is 90 mm. The average measurement of the three axial LVDTs is used as the axial deformation of the test specimen.

It should be noted that all the test data used in this work are from a previous study [38].

2.5. Model calibration

All the material parameters in the model can be determined from the creep test data. Firstly, we determined the creep compliance or relaxation modulus from the nondestructive creep test data. Then, by determining the initial resistance to damage of specimens with different air void contents, the relationship between resistance to damage and mass specific volume can be obtained. Finally, we fitted model predictions to the destructive test data, the rest parameters, k_1 and k_2 in Equation 2.18, were obtained.

(1) Determination of mixture viscoelastic properties

For asphalt concrete, it is easy to carry out a constant-stress creep test while a constant-strain relaxation test is difficult to run. However, the relaxation modulus is used more widely in the performance prediction of asphalt concrete, such as in the finite-element simulations and other computational programs. The relaxation modulus for linear viscoelastic materials can be determined based on the creep test results using the interconversion law as follow.

$$\bar{E}_0(s)\bar{J}_0(s) = \frac{1}{s^2} \tag{2.22}$$

where $\bar{E}_0(s)$ and $\bar{J}_0(s)$ are the Laplace transform of the relaxation modulus and the creep compliance respectively, and s is the transform parameter. The Laplace transform or inverse Laplace transform of a function can be easily solved with the help of some programming software, like MATLAB. The corresponding relaxation modulus parameters are summarized in Table 2.1.

Table 2.1 Coefficients of Relaxation Modulus Obtained from Test Data

Binder type	Aging periods	Air void content	Temperature	E_∞ (GPa)	E_1(GPa)	E_2 (GPa)	τ_1 (s)	τ_2 (s)
Nustar	0 months	4%	10 ºC	2.131	12.47	3.673	0.95	25.46
			20 ºC	0.59	6.55	1.39	0.82	15.32
			30 ºC	0.1961	3.721	0.6528	0.5112	8.477
		7%	10 ºC	2.636	6.653	4.814	1.504	22.37
			20 ºC	0.9828	10.13	2.191	0.5191	13.96
			30 ºC	0.3717	3.842	0.606	0.769	11.95
Valero	0 months	4%	10 ºC	3.821	13.01	4.759	0.6209	15.05
			20 ºC	0.7765	7.693	1.909	0.7515	15.36
		7%	10 ºC	2.271	19.37	4.303	0.3702	15.58
			20 ºC	0.4305	14.08	1.339	0.3344	13.87

(2) Determination of resistance to damage

In Equation 2.19, there are two parameters, S_0 and a, so their values can be determined using two groups of test data, namely the initial resistance to damage, which is the resistance to damage at the reference configuration, of specimens with two air void contents, 4% and 7%. Here we assume that the density of asphalt concrete without air voids is 2700 kg/m^3, so the corresponding mass specific volume is 3.7×10^{-4}m^3/kg. Therefore, for specimens whose air void content is 4%, their mass specific volume at the reference configuration is 3.848×10^{-4}m^3/kg, while for the specimen whose air void content is 7%, the value is 3.959×10^{-4}m^3/kg. Then, to obtain the value of the initial resistance to damage, we simulated its viscoelastic behavior under the same age, temperature and load level as that in the corresponding destructive test, and the simulation result is compared with the test data. As shown in Figure 2.1, the behavior of unaged asphalt concrete under a load level of 109.8 kPa at 20°C is simulated without considering damage, and the simulation result is compared with the test data. Since damage is the only contribution to the difference between the red curve

and the blue curve, the damage initiation position is defined as the position where the two lines begin to diverge. Once the damage initiation position is be determined and the corresponding damage initial resistance to damage can be obtained using stress and strain test data. The values of $S(v_R)$ under different conditions are represented in Table. 3. It can be seen that Valero mixtures have a higher resistance to damage than that of Nustar mixtures under the same condition, and when the change of mass specific volume is the same, a stiffer mixture typically sees a larger decrease of $S(v_R)$. Then, by fitting the test data of the specimens with the same binder but different air void contents, the relationship between the resistance to damage and the mass specific volume at the specific condition can thus be determined. Figure 2.2 shows the evolution of resistance to damage of unaged asphalt concrete with Nustar binder at 20^0C and the coefficients for the evolution of resistance to damage are summarized in Table 2.2.

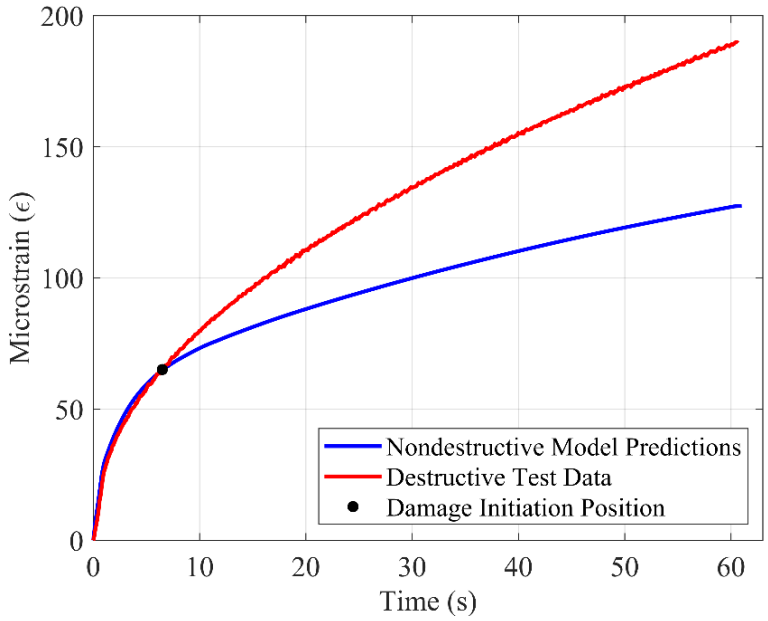

Figure 2.1 Determination of Damage Initiation Position. The creep tension test performed on the unaged asphalt mixture with 4.0% air void and a load level of 109.8kPa at 20°C.

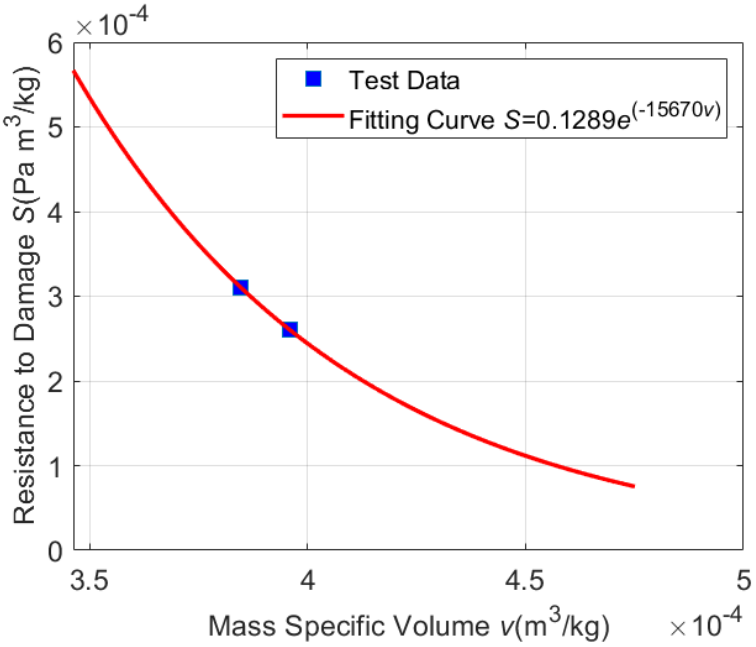

Figure 2.2 Evolution of resistance to damage of unaged asphalt concrete with Nustar binder at 20°C.

Table 2.2 Coefficients for the Evolution of Resistance to Damage

Binder type	Aging periods	Temperature	S_0 (Pa·m^3/kg)	a
Nustar	0 months	10 ºC	0.0139	-5462
		20 ºC	0.1289	-15670
		30 ºC	0.0245	-12260
Valero	0 months	10 ºC	0.4977	-13370
		20 ºC	0.3563	-17630

(3) Determination of damage parameters

After determining the relaxation modulus and the relationship between the resistance to damage and mass specific volume, we can obtain the parameters, k_1 and k_2, by fitting the test data. The fits obtained for asphalt concrete under different conditions are presents in Figures 3-6. They show that the model fits the experimental results very well at different conditions and the corresponding values of k_1 and k_2 are summarized in Table 2.3. It can be seen that the value of k_2 increases with the increase of stiffness, and this shows the damage develops faster in a stiffer mixture, because compared with that in the mixture at low temperature, more energy in the mixture at high temperature is dissipated due to viscoelasticity, so less energy is used to cause damage.

In this work, the nominal configuration is adopted to build the damage model. However, many researchers prefer to build CDMs in the effective configuration and use the concept of effective stress, and define the damage variable as the ratio of the lost cross section area to the initial area [39, 40], so under uniaxial loading, the stress on the lost area is zero, while the effective stress is uniformly distributed on the intact area. In this case, the values of state variables will not be continuous in the material

and the material is not a continuum anymore, so this kind of definition of damage is problematic. Therefore, CDMs should be built in the nominal configuration.

Table 2.3 Damage Evolution Parameters Obtained from Test Data

Binder type	Aging periods	Air void content	Temperature	Load Level (kPa)	$S(Y_R)$ (Pa·m^3/kg)	k_1	k_2
Nustar	0 months	4%	10 ºC	384.2	0.0017	0.17	0.47
			20 ºC	109.8	3.10×10^{-4}	0.11	0.40
			30 ºC	27.4	2.18×10^{-4}	0.19	0.37
		7%	10 ºC	653.2	0.0016	0.06	0.43
			20 ºC	103.4	2.61×10^{-4}	0.11	0.35
			30 ºC	81.6	1.91×10^{-4}	0.06	0.32
Valero	0 months	4%	10 ºC	544.3	0.0029	0.11	0.63
			20 ºC	130.6	4.04×10^{-4}	0.12	0.48
		7%	10 ºC	435.5	0.0025	0.17	0.51
			20 ºC	76.2	3.32×10^{-4}	0.21	0.39

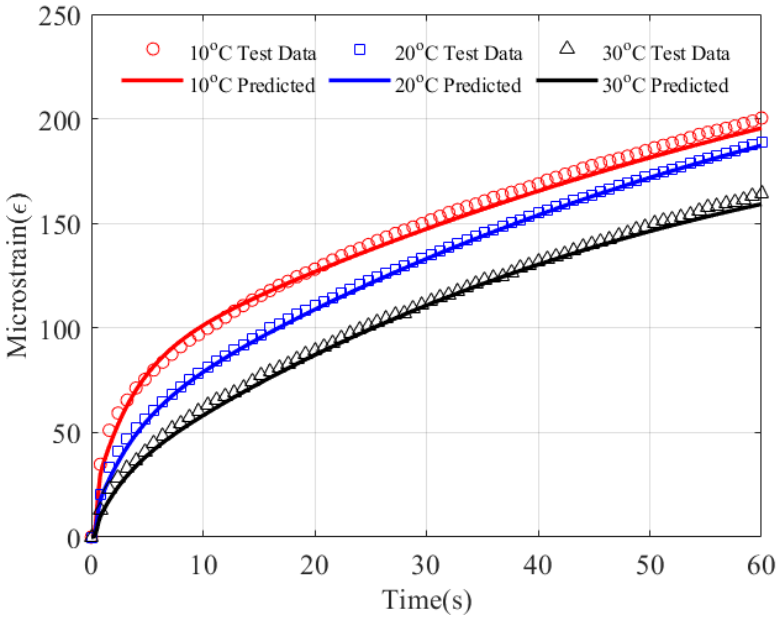

Figure 2.3 Comparison between model predictions with creep tension test data on unaged Nustar asphalt mixtures (4% air void content) at different temperatures.

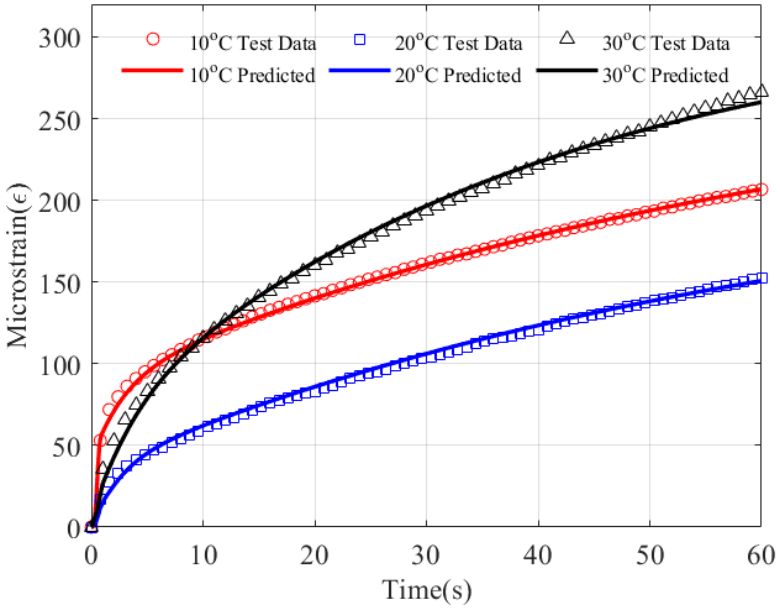

Figure 2.4 Comparison between model predictions with creep tension test data on unaged Nustar asphalt mixtures (7% air void content) at different temperatures.

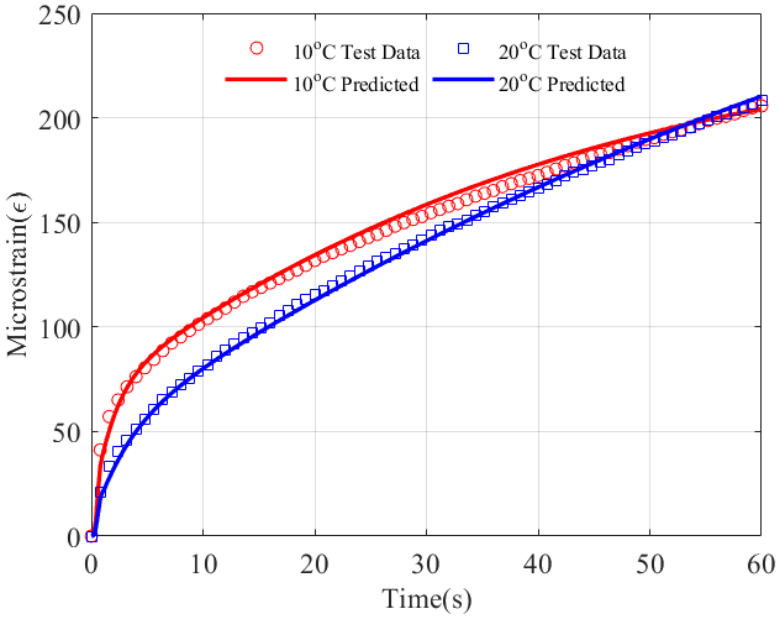

Figure 2.5 Comparison between model predictions with creep tension test data on unaged Valero asphalt mixtures (4% air void content) at different temperatures.

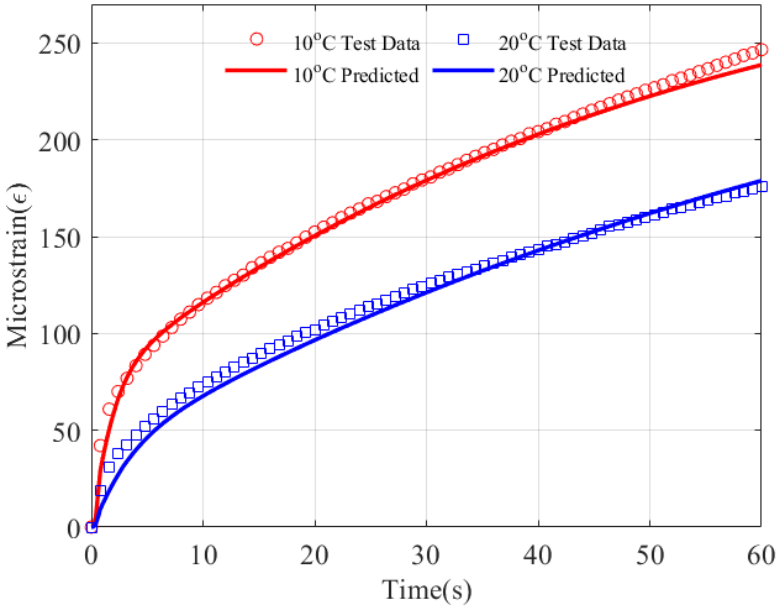

Figure 2.6 Comparison between model predictions with creep tension test data on unaged Valero asphalt mixtures (7% air void) at different temperatures.

2.6. Model verification

(1) Cyclic loading

After obtaining the values of all the model parameters, we simulated the behavior of asphalt concrete under controlled-strain RDT to validate the accuracy of the proposed viscoelastic damage model. All the simulations in this work are performed using COMSOL Multiphysics. The weak form partial differential equation (PDE) method can be used to implement the viscoelastic constitutive model and details about this method can be found in a previous study [41]. In addition, the previous solution operator is used and two additional features are included in the model tree to implement the damage model. The first feature is the Domain ODEs and DAEs interface, and it is added to the model to keep track of the maximum value of damage, because in this work the healing effect of

asphalt concrete is not considered and the damage in the material under loading does not decrease. The second feature is the Previous Solution feature and it is added to the Time-Dependent Solver.

Figures 2.7(a) and 2.8(a) show the test data of strain measured and the damage predicted using the proposed model, and it can be seen that damage increases monotonically under cyclic loading, and compared with stress, the strain contributes more to the development of damage, because once the volumetric energy reaches the resistance to damage, damage will increase with increasing strain, even though the corresponding stress has shown decrease. It is because the driving energy we defined is related to strain energy density. Figures 2.7(b) and 2.8(b) show the comparisons between the model predictions and measured stress data for the asphalt mixtures with two air void content and two binders. It can be seen that the predicted stress matches the test result well, and the reason why the match is not perfect may be that plastic deformation occurs in the material, which is not represented in the proposed model. Figures 2.7(c) and 2.8(c) show the damage evolution in the material, and it can be seen that the rate of damage increases first and then decrease in each cyclic loading period and the damage increment in the first loading cycle is largest. These findings show that the proposed model can predict the mechanical behavior of asphalt concrete reliably.

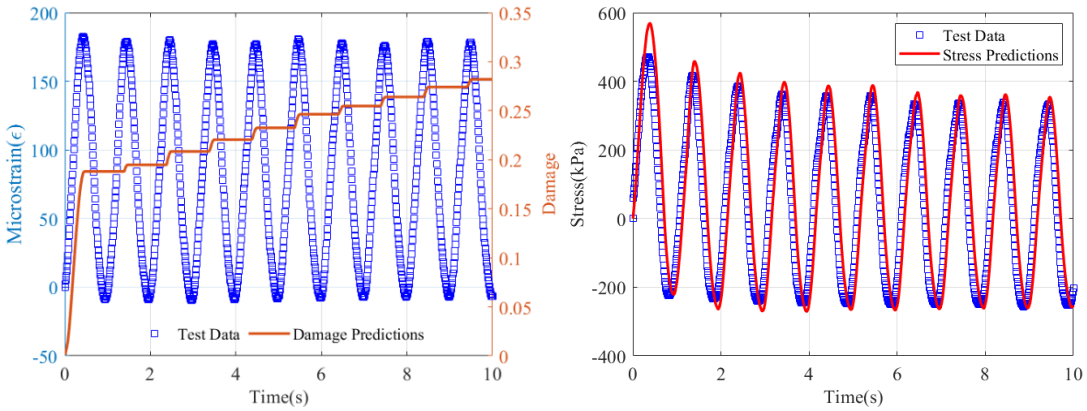

(a)

(b)

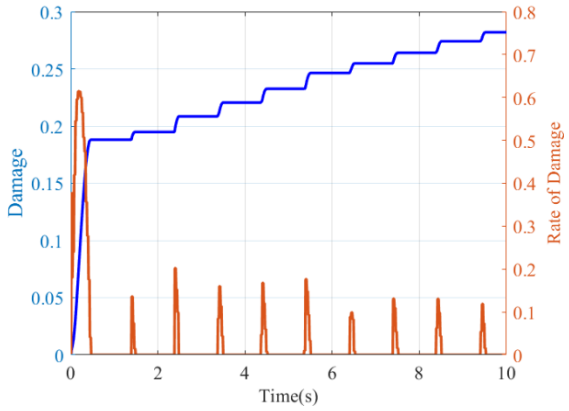

(c)

Figure 2.7 Behavior of unaged Nustar asphalt mixture (7% air void content) at 20ºC in the RDT test. (a) Measured strain data, (b) comparison between measured stress data and model predictions, (c) Damage evolution predicted.

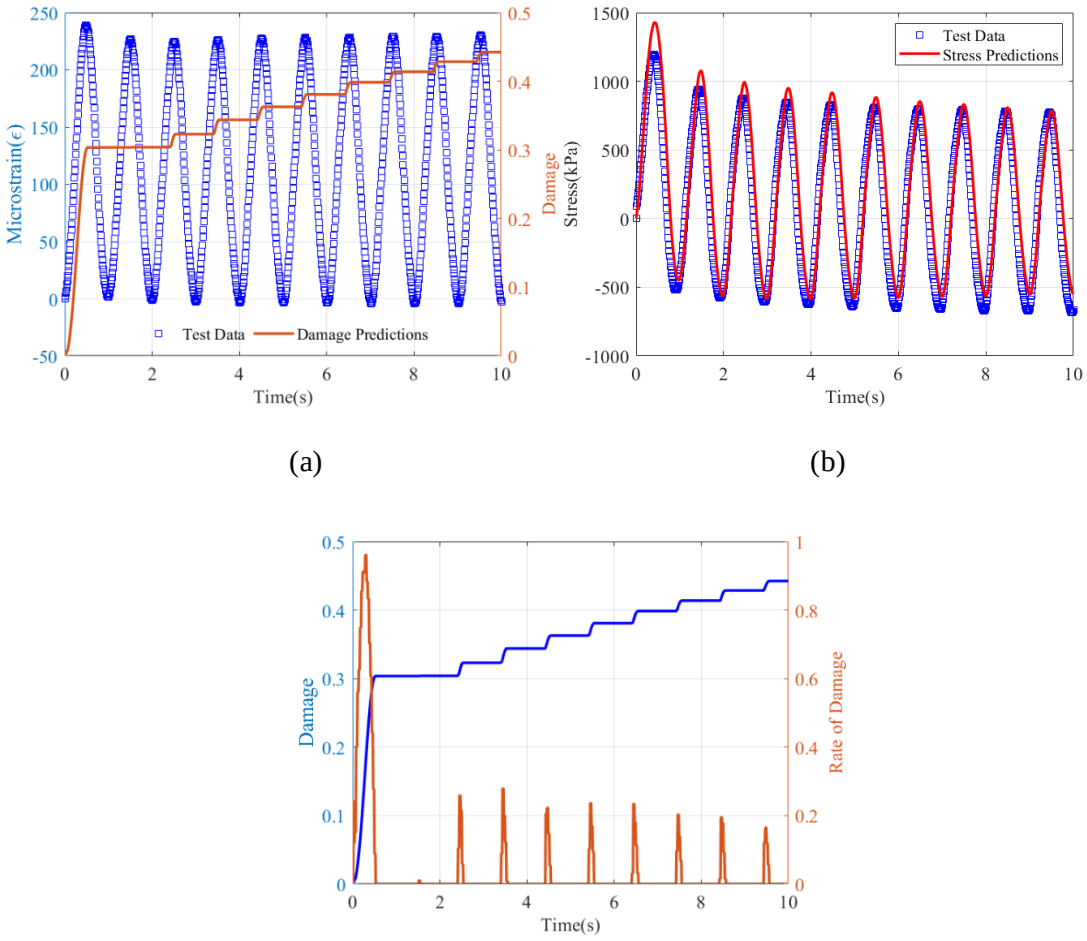

Figure 2.8 Behavior of unaged Valero asphalt mixtures (4% air void content) at 20ºC in the RDT test. (a) Measured strain data, (b) comparison between measured stress data and model predictions, (c) Damage evolution predicted.

(2) Modeling of an actual pavement with repeated loads

Top-down fatigue cracking is a major form of premature degradation and failure in flexible pavements, especially thick flexible pavements [42]. In order to demonstrate that the model proposed is able to capture the fatigue cracking of asphalt concrete pavements under traffic loading, a three-layer 2-D axial symmetric model is

adopted to idealize the pavement. The dimensions of the pavement are shown in Figure 2.9, and it can be seen that the thickness of the asphalt concrete layer, base layer and subgrade layer are 200mm, 750mm and 350mm respectively. The radius of the representative pavement structure is 1400mm, and the radius of the contact area between the tire and pavement is 140mm. For boundary conditions, we assume the bottom edge of the pavement is fixed, and the right edge is constrained in the *r* direction but free in the vertical direction. The structure is axial symmetry about the left edge (r=0), and on the surface of the pavement, a traffic loading applied is in the form of sinusoidal wave with the amplitude of 600 kPa, as shown in Figure 2.10. In addition, the HMA layer is modelled using the constitutive relationship proposed in this work and the material properties are the same as that of unaged Nustar asphalt mixtures with 4% air void contents at 20^0C as shown in Tables. 1, 2 and 3. The unbounded base and subgrade layers are assumed to be elastic. The corresponding resilient moduli are 275 MPa and 100 MPa respectively and the Poisson's ratio are 275MPa and 0.24 respectively.

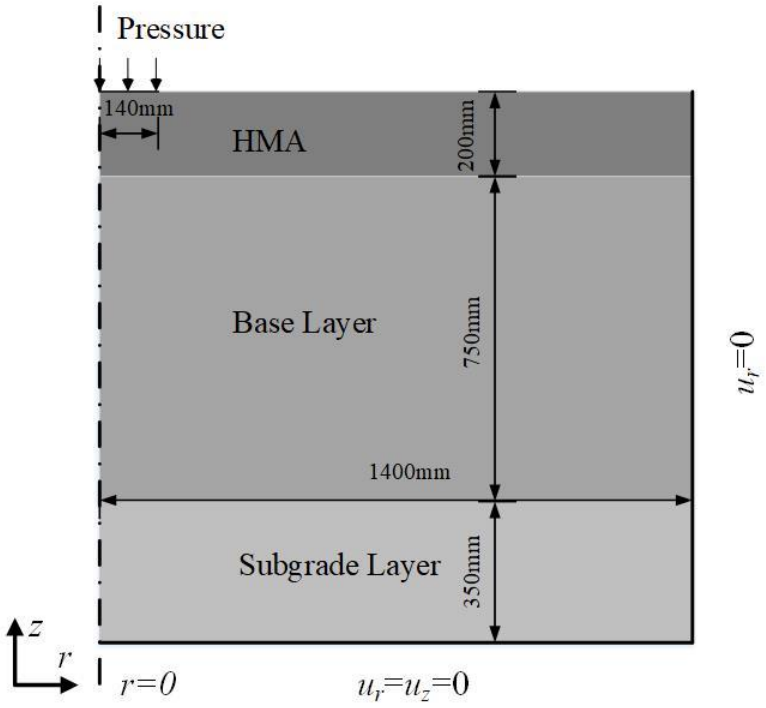

Figure 2.9 Finite-element model of asphalt pavement with associated boundary conditions.

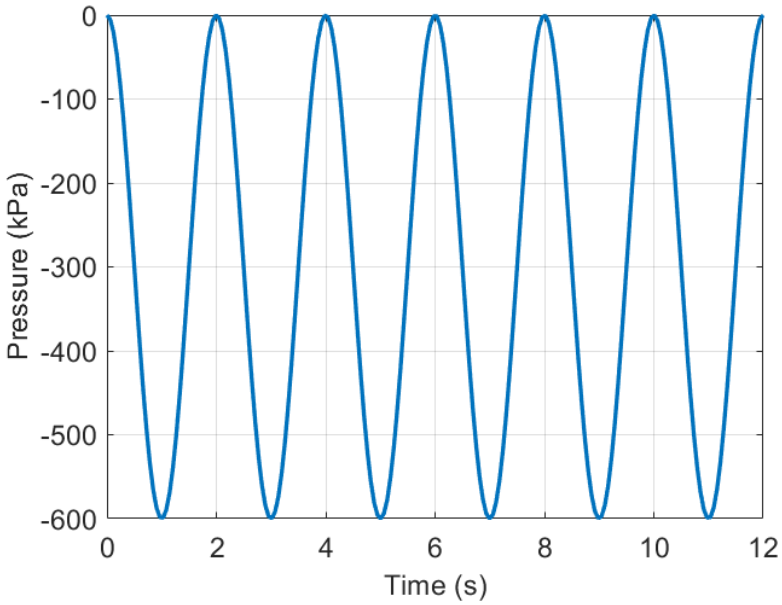

Figure 2.10 Pressure applied on the surface of the pavement.

The simulation is performed using COMSOL Multiphysics and the axial symmetry of the structure is considered to save memory and computation time. The pavement behavior after 500 cycles of loading is simulated and the simulation results are shown in Figures. 2.11-2.13. Figure 2.11 represents the damage distribution in the pavement, and it can be seen that cracks could happen at the bottom of HMA under the wheel and then propagate upwards leading to bottom-up cracking, and top-down cracking as a major form of failure in thick flexible pavements happens on the surface near the wheel. Figure 2.12 shows the driving energy of damage distribution in the pavement during the 500^{th} cycle of loading, and it shows that the driving energy is high in the bottom-up and top-down cracking areas, and the highest driving energy happens in the top-down cracking area. Figure 2.13 represents the vertical stress distribution in the pavement during the 500^{th} loading cycle and the result shows that the largest compressive stress happens on the contact surface between the pavement and tire, and with depth the stress decays. All these findings show that the proposed model can characterize fatigue cracking reasonably.

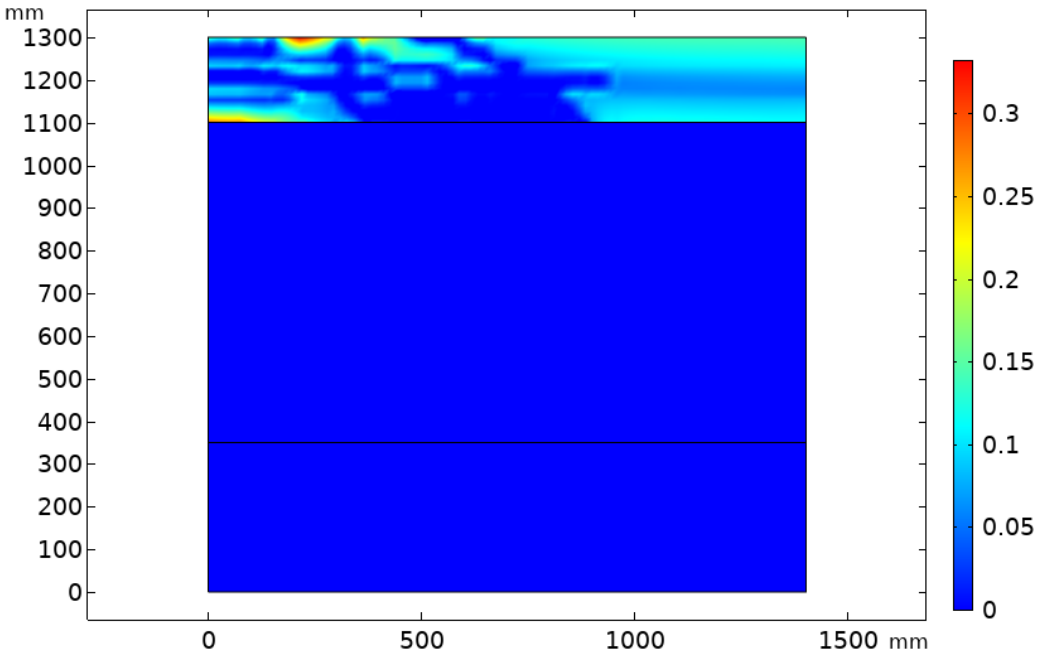

Figure 2.11 Damage distribution in the pavement when time=1000s.

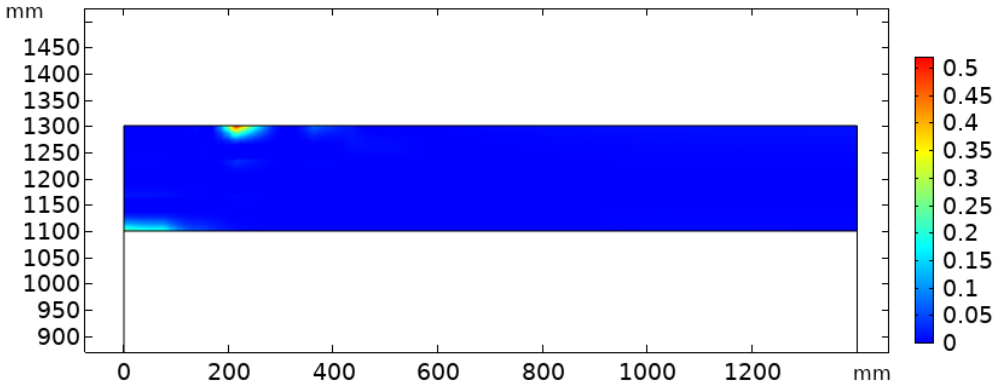

Figure 2.12 Distribution of the driving energy of damage in the pavement when time=999s (Unit: Pa).

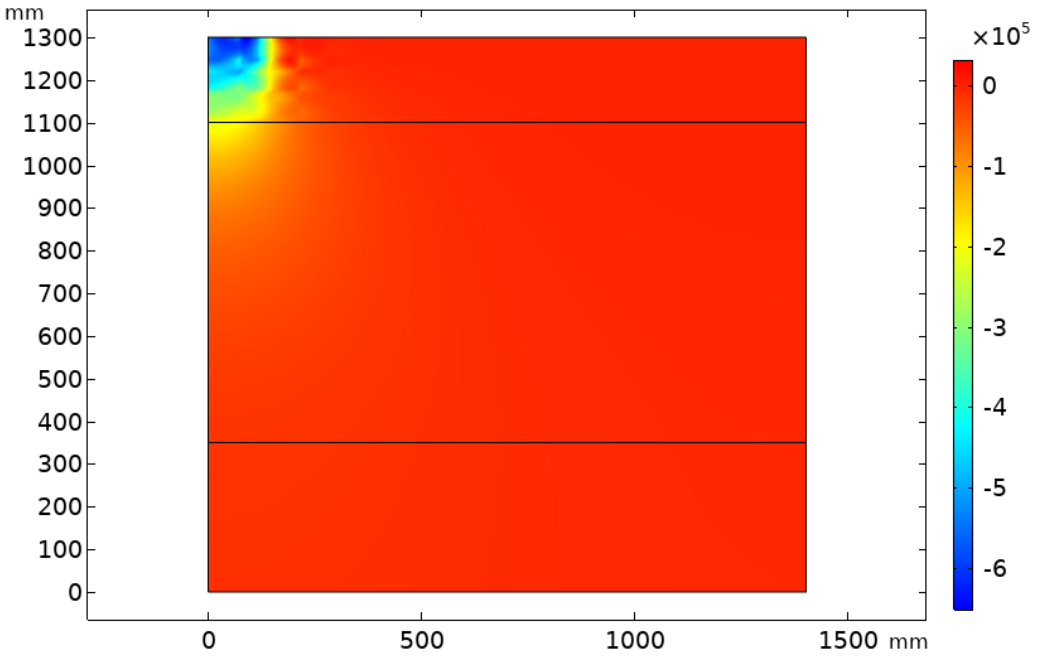

Figure 2.13 Vertical stress distribution in the pavement when time=999s (Unit: Pa).

2.7. Summary and conclusions

This paper presents a new viscoelastic damage model to accurately simulate damage of asphalt mixtures under destructive loading. The damage evolution function is expressed as a power function of the mass specific volume, which is independent of reference configuration. The resistance to damage is defined as an exponential function of mass specific volume to represent decrease of resistance to damage with increase of damage, because damage can cause the dilatancy of the material and increase the mass specific volume.

All the parameters in the model can be determined from creep tests. Nondestructive creep test data are used to obtain the relaxation modulus, while destructive creep test data are used to determine the change of resistance to damage

with mass specific volume, and other parameters. In addition, the destructive RDT test were performed and the corresponding test data are used to verify the validity of the model. It shows that the rate of damage increases first and then decreases in each cyclic loading period and the first loading cycle sees the largest damage increment. The simulation of pavement behavior under traffic loading shows that the proposed model can capture fatigue cracking in the pavement well and in thick flexible pavements, both top-down cracking and bottom-up cracking occurs, but top-down cracking is dominant.

2.8. References

[1] Y.H. Dinegdae, I. Onifade, D. Jelagin, B. Birgisson, Mechanics-based top-down fatigue cracking initiation prediction framework for asphalt pavements, Road Materials and Pavement Design 16(4) (2015) 907-927.

[2] R. Roque, B. Birgisson, C. Drakos, B. Dietrich, Development and field evaluation of energy-based criteria for top-down cracking performance of hot mix asphalt (with discussion), Journal of the Association of Asphalt Paving Technologists 73 (2004).

[3] B. Birgisson, J. Wang, R. Roque, Implementation of the Florida cracking model into the mechanistic-empirical pavement design, 2006.

[4] M. Rahmani, Y.R. Kim, Y.B. Park, J.S. Jung, Mechanistic Analysis of Pavement Damage and Performance Prediction Based on Finite Element Modeling with Viscoelasticity and Fracture of Mixtures, LHI Journal of Land, Housing, and Urban Affairs 11(2) (2020) 95-104.

[5] S. Ahmed, E.V. Dave, W.G. Buttlar, M.K. Exline, Cracking resistance of thin-bonded overlays using fracture test, numerical simulations and early field performance, International Journal of Pavement Engineering 14(6) (2013) 540-552.

[6] A. Bekele, R. Balieu, D. Jelagin, N. Ryden, A. Gudmarsson, Micro-mechanical modelling of low temperature-induced micro-damage initiation in asphalt concrete based on cohesive zone model, Construction and Building Materials 286 (2021) 122971.

[7] Y.R. Kim, F.T. Aragao, D.H. Allen, D.N. Little, Damage modeling of bituminous mixtures considering mixture microstructure, viscoelasticity, and cohesive zone fracture, Canadian Journal of Civil Engineering 37(8) (2010) 1125-1136.

[8] M.P. Wagoner, W.G. Buttlar, G.H. Paulino, Development of a single-edge notched beam test for asphalt concrete mixtures, Journal of Testing and Evaluation 33(6) (2005) 452-460.

[9] F.A.C.d. Freitas, A theoretical and experimental technique to measure fracture properties in viscoelastic solids, 2007.

[10] H. Ban, S. Im, Y.R. Kim, J.S. Jung, Laboratory tests and finite element simulations to model thermally induced reflective cracking of composite pavements, International Journal of Pavement Engineering 19(3) (2018) 220-230.

[11] Y. Zhang, X. Luo, R. Luo, R.L. Lytton, Crack initiation in asphalt mixtures under external compressive loads, Construction and Building Materials 72 (2014) 94-103.

[12] Y.D. Wang, B. Keshavarzi, Y.R. Kim, Fatigue performance prediction of asphalt pavements with FlexPAVETM, the S-VECD model, and DR failure criterion, Transportation Research Record 2672(40) (2018) 217-227.

[13] M.E. Kutay, M. Lanotte, Viscoelastic continuum damage (VECD) models for cracking problems in asphalt mixtures, International journal of pavement engineering 19(3) (2018) 231-242.

[14] D.J. Mensching, R. Rahbar-Rastegar, B.S. Underwood, J.S. Daniel, Identifying indicators for fatigue cracking in hot-mix asphalt pavements using viscoelastic continuum damage principles, Transportation Research Record 2576(1) (2016) 28-39.

[15] R. Balieu, N. Kringos, F. Chen, E. Córdoba, Multiplicative viscoelastic-viscoplastic damage-healing model for asphalt-concrete materials, 8th RILEM International

Conference on Mechanisms of Cracking and Debonding in Pavements, Springer, 2016, pp. 235-240.

[16] H. Liu, X. Yang, L. Jiang, S. Lv, T. Huang, Y. Yang, Fatigue-creep damage interaction model of asphalt mixture under the semi-sine cycle loading, Construction and Building Materials 251 (2020) 119070.

[17] Z. Zhang, Q. Liu, Q. Wu, H. Xu, P. Liu, M. Oeser, Damage evolution of asphalt mixture under freeze-thaw cyclic loading from a mechanical perspective, International Journal of Fatigue 142 (2021) 105923.

[18] R.A.J.I.j.o.f. Schapery, Correspondence principles and a generalized J integral for large deformation and fracture analysis of viscoelastic media, 25(3) (1984) 195-223.

[19] Y. Zhang, F. Gu, B. Birgisson, R.L. Lytton, Modelling cracking damage of asphalt mixtures under compressive monotonic and repeated loads using pseudo J-integral Paris' law, Road Materials and Pavement Design 19(3) (2018) 525-535.

[20] X. Luo, R. Luo, R. L. Lytton, Characterization of fatigue damage in asphalt mixtures using pseudostrain energy, Journal of Materials in Civil Engineering 25(2) (2013) 208-218.

[21] J. Zhang, Y.D. Wang, Y. Su, Fatigue damage evolution model of asphalt mixture considering influence of loading frequency, Construction and Building Materials 218 (2019) 712-720.

[22] S. Lv, L. Hu, C. Xia, X. Wang, M.B. Cabrera, S. Guo, J. Chen, Development of fatigue damage model of asphalt mixtures based on small-scale accelerated pavement test, Construction and Building Materials 260 (2020) 119930.

[23] J. Zhang, Z. Li, H. Chu, J. Lu, A viscoelastic damage constitutive model for asphalt mixture under the cyclic loading, Construction and Building Materials 227 (2019) 116631.

[24] M.K. Darabi, R.K.A. Al-Rub, E.A. Masad, D.N. Little, Constitutive modeling of fatigue damage response of asphalt concrete materials with consideration of micro-damage healing, International Journal of Solids and Structures 50(19) (2013) 2901-2913.

[25] O.E. Gungor, I.L. Al-Qadi, A. Gamez, J.A. Hernandez, In-situ validation of three-dimensional pavement finite element models, The roles of accelerated pavement testing in pavement sustainability, Springer, 2016, pp. 145-159.

[26] L.M. KACHANOV, Time of the rupture process under creep conditions, Izy Akad, Nank SSR Otd Tech Nauk 8 (1958) 26-31.

[27] F. Cozzarelli, G. Bernasconi, Non-linear creep damage under one-dimensional variable tensile stress, International Journal of Non-Linear Mechanics 16(1) (1981) 27-38.

[28] C. Lee, F. Cozzarelli, K. Burke, One-dimensional strain-dependent creep damage in inhomogeneous materials, International journal of non-linear mechanics 21(4) (1986) 303-314.

[29] M.K. Darabi, R.K.A. Al-Rub, E.A. Masad, C.W. Huang, D.N. Little, A thermo-viscoelastic–viscoplastic–viscodamage constitutive model for asphaltic materials, International Journal of Solids and Structures 48(1) (2011) 191-207.

[30] D.N. Little, D.H. Allen, A. Bhasin, Modeling and design of flexible pavements and materials, Springer, 2018.

[31] D. Krajcinovic, J. Lemaitre, Continuum damage mechanics: theory and applications, Springer, 1987.

[32] J. Lemaitre, R. Desmorat, Engineering damage mechanics: ductile, creep, fatigue and brittle failures, Springer Science & Business Media, 2005.

[33] J. Lemaitre, J. Sermage, R. Desmorat, A two scale damage concept applied to fatigue, International Journal of fracture 97(1) (1999) 67-81.

[34] I. Onifade, B. Birgisson, R. Balieu, Energy-based damage and fracture framework for viscoelastic asphalt concrete, Engineering Fracture Mechanics 145 (2015) 67-85.

[35] I. Onifade, B. Birgisson, Damage and fracture characterization of asphalt concrete mixtures using the equivalent micro-crack stress approach, Construction and Building Materials 148 (2017) 521-530.

[36] P.T. Murru, C. Torrence, Z. Grasley, K. Rajagopal, P. Alagappan, E.J.I.J.o.P.E. Garboczi, Density-driven damage mechanics (D3-M) model for concrete I: mechanical damage, (2020) 1-14.

[37] P.T. Murru, Study of Damage in Concrete Based on Microscopic Changes in Density, 2019.

[38] X. Luo, Characterization of fatigue cracking and healing of asphalt mixtures, 2012.

[39] N. Hansen, H. Schreyer, A thermodynamically consistent framework for theories of elastoplasticity coupled with damage, International Journal of Solids and Structures 31(3) (1994) 359-389.

[40] L. Kachanov, Introduction to continuum damage mechanics, Springer Science & Business Media, 1986.

[41] Y. Zhang, B. Birgisson, R.L. Lytton, Weak form equation–based finite-element modeling of viscoelastic asphalt mixtures, Journal of Materials in Civil Engineering 28(2) (2016) 04015115.

[42] H. Wang, I.L. Al-Qadi, Combined effect of moving wheel loading and three-dimensional contact stresses on perpetual pavement responses, Transportation research record 2095(1) (2009) 53-61.

3. AN ENERGY-BASED PLASTICITY MODEL TO PREDICT THE RUTTING PERFORMANCE OF FLEXIBLE PAVEMENTS

3.1. Introduction

Rutting is one of the main distresses in flexible pavements and accurate prediction of rutting plays an important role in the decision making about pavement design, maintenance and rehabilitation [1-5]. Rutting arises from the accumulation of plastic deformation under traffic loading, and plastic deformation can occur in each layer of the pavement, including the asphalt concrete layer, base layer and subgrade layer. Apart from traffic loading, the pavement structure and the microstructure of pavement materials, the rutting performance of flexible pavements is also affected by temperature [6-8]. It is because asphalt concrete is temperature-dependent. During summer, due to high temperature, asphalt concrete is soft, so it can bear less stress and transfer more stress into sublayers. However, during winter, due to low temperature, asphalt concrete is stiff, so it can sustain more stress and transfer less stress to sublayers. This explains why rutting mainly happens in summer.

To predict the rutting development in flexible pavements, many empirical models are proposed. For example, many researchers [9-14] built rutting models based on the experimental data and correlate rut depth with the number of loading cycles. However, these models did not consider the effect of material properties. Once one component property is changed, existing relationship in these models will not work, so prediction on materials' behavior should be based on fundamental material properties, instead of

performance indicators [15]. Some studies tried to correlate rutting in the asphalt concrete layer with the property of asphalt binder based on experimental data. For example, Zhang et al. [16] tried to use G^*/δ (where G^* is the complex modulus and δ is the phase angle of asphalt binder) and J_{nr} (nonrecoverable creep compliance of asphalt binder) respectively to predict the rut depth in the asphalt concrete layer, and it was found that J_{nr} has a higher correlation with the Hamburg wheel-tracking test data and the repeated load permanent deformation test data. However, the deterioration mechanism of in-service pavements, like aging, may not be represented well by laboratory tests. In this case, some studies tried to build rutting models based on field data. For example, Chen and Tsai [17] correlated G^*/δ with the rutting in the asphalt concrete layer of in-service pavement sections. Walubita et al. [18] tried to correlate the binder properties determined based on the multiple stress creep and recovery test, with the rutting performance in the laboratory and field. However, the permanent deformation of asphalt concrete is affected by many factors, like the gradation, and stiffness of aggregates [19-22]. For example, it is found that fine aggregates and small maximum aggregate size is good for the rutting resistance in concrete [23, 24]. Another drawback of the models mentioned above is that they can hardly reflect the mechanism of plastic development in the material.

Apart from empirical models, mechanical models based on plasticity theory are wildly used to predict rutting in flexible pavements. Some researchers [25-29] built stress-based yield models, and the yield surface function was expressed as a function of stress invariants. Once the stress surpasses the initial yield surface, plastic deformation occurs. The evolution of the yield surface is governed by the hardening parameter, and the

hardening parameter was usually expressed as a function of temperature and strain rate to capture the temperature- and frequency- dependent properties of asphalt concrete. Apart from stress-based models, energy-based plasticity models have been used to predict the distress development in asphalt concrete [30-35]. In the energy-based models, the energy resistance for asphalt concrete under different loading frequencies is the same, so one energy-based plasticity criterion can be used to predict plastic deformation of the material under various loading frequencies. Compared with the stress-based plasticity model, one advantage of the energy-based plasticity model is that it can simplify the modelling process and can be applied easily, because in the stress-based plasticity models, the coupling of loading rate and temperature sometimes have to be considered and this can make the determination of material parameters complicated. However, the models mentioned above were verified based on experimental data instead of the field data, and most of these models did not consider the effect of aging. Huang et al. [36] proposed an energy-based plasticity model and incorporated it to a predictive framework to predict the rutting performance of flexible pavement. In this framework, the effect of aging, temperature and loading rate were considered. To verify the validity of the predictive framework, field test data obtained from WesTrack project [37] was adopted. In the WesTrack project, the corresponding full-scale test was performed near Reno, Nevada. The precipitation in the site is less than 100 mm per year and there is no frost penetration, so the effect of precipitation on the rutting performance is negligible. Furthermore, the pavement structure was well designed to guarantee that plastic deformation mainly occurred in the asphalt concrete layer. Therefore, the project is well suited for evaluating

the effect of the composition and property of asphalt concrete on the pavement performance. However, in the energy-based plasticity model [36], the plasticity resistance was expressed as a function of time. Although it can reflect the effect of aging, it cannot reflect seasonal variation of the resistance, and the plasticity resistance in winter is usually higher than that in summer.

In this work, a new plasticity model is proposed and incorporated in a framework to predict the rutting in the asphalt concrete layer of pavements. The effects of loading frequencies, temperature and aging are considered, and the plasticity resistance is expressed as a function of the scalar modulus to capture the seasonal variation of the resistance. This work is organized as follows. In next section, a new energy-based plasticity model is proposed. Then, the plasticity model is incorporated into a predictive framework, and the mechanical properties of asphalt concrete can be determined based on its microstructure and properties of each component. Next, the WesTrack project is briefly introduced and the field data from this project are used to verify the plasticity model and the predictive framework. The last section summarizes the main findings.

3.2. Model formulation

Asphalt concrete is a temperature- and frequency- dependent material, in this section, an energy-based plasticity model is proposed to predict the behavior of asphalt concrete under different frequencies. Then, the plasticity model is incorporated into a predictive framework, and the framework can account for the effect of temperature, frequencies and aging on the behavior of the asphalt concrete layer in flexible pavements.

3.2.1. Energy-based plasticity model

For asphalt concrete, under different loading frequencies, its behavior and yield stress are different. To capture the plastic behavior under different loading frequencies, an energy-based plasticity model is proposed. When the driving energy for plasticity exceeds a critical energy threshold, plastic deformation happens. Before the introduction of the driving energy, an energy tensor is first defined as

$$\mathbf{W} = \boldsymbol{\sigma}\varepsilon_{eq} \tag{3.1}$$

with

$$\varepsilon_{eq} = \sqrt{\frac{(\varepsilon_1 - \varepsilon_2)^2 + (\varepsilon_2 - \varepsilon_3)^2 + (\varepsilon_1 - \varepsilon_2)^2}{2(1+\nu)^2}} \tag{3.2}$$

where $\boldsymbol{\sigma}$ is the stress tensor, ε_{eq} the equivalent strain, ε_1, ε_2 and ε_3 principal strain, and ν the Poisson's ratio.

Similar to the stress decomposition, the energy tensor can also be decomposed into volumetric part and deviatoric part as below.

$$W_{ij} = W_{ij}^D + W_{ij}^V = W_{ij}^D + \frac{1}{3}W_{ij}\delta_{ij} \tag{3.3}$$

where W_{ij}^D and W_{ij}^V are the deviatoric and volumetric energy tensor components respectively, and δ_{ij} is the Kronecker delta.

Since for pressure-dependent materials, their plasticity is mainly driven by the deviatoric driving energy and is related to the volumetric driving energy, the driving energy for plasticity is expressed as the sum of these two types of driving energy as below.

$$Y_p = Y_p^d + aY_p^v = \sqrt{\frac{3}{2} W_{ij}^D W_{ij}^D} + a\sqrt{W_{ij}^V W_{ij}^V} \tag{3.4}$$

where Y_p^d and Y_p^v are the deviatoric and volumetric driving energy respectively, and a is called the pressure sensitivity parameter and it is used to consider tension and compression stress states. It is defined as below.

$$a = \text{sgn}\left(tr\left(\mathbf{W}\right)\right) = \begin{cases} -1, \text{ for } tr\left(\mathbf{W}\right) < 0 \\ 0, \text{ for } tr\left(\mathbf{W}\right) = 0 \\ 1, \text{ for } tr\left(\mathbf{W}\right) > 0 \end{cases} \tag{3.5}$$

where $tr(\cdot)$ means the trace of a matrix.

Since the initial resistance to plasticity can change with temperature and aging of the asphalt binder, the initial resistance to plasticity is defined as a function of scalar modulus as below.

$$Y_0 = Ap \cdot S_M \tag{3.6}$$

where Ap is a material parameter, and S_M is the scalar modulus of materials. The scalar modulus is expressed as the ratio of linear viscoelastic stress and the pseudo-strain given as:

$$S_M = \frac{\sigma(t)}{\varepsilon^R} \tag{3.7}$$

with

$$\varepsilon^R = \frac{f(r)}{E_\infty} \cdot \frac{d\varepsilon}{dt} \cdot \left(E_\infty t + \sum_{i=1}^{N} E_i \rho_i \left(1 - e^{-\frac{t}{\rho_i}}\right)\right) \tag{3.8}$$

where E_i and E_∞ correspond to the moduli in the generalized Maxwell model, and ρ_i is the corresponding relaxation time.

To consider the load-dependency, a load-dependency parameter is introduced in the energy-based yield criterion, which is defined as:

$$f = \frac{Y_p}{Y_0} \cdot \left(\frac{W_i}{W_{s0}} \right)^{L_p} - 1 - P \geq 0 \tag{3.9}$$

where W_i the axle load of i_{th} axle in kN, W_{s0} equals 80 kN and is the standard axle load, L_p the load-dependency parameter, and P is the plasticity variable and it is defined in Equation 3.10.

To facilitate the implementation of the plasticity model, some simplification is needed. When f is larger than 0, the vertical plasticity flow rule is defined as below.

$$\dot{P} = Kp \cdot \left\langle \frac{Y_p}{Y_0} \cdot \left(\frac{W_i}{W_{s0}} \right)^{L_p} - 1 \right\rangle^{Np} \tag{3.10}$$

where Kp and Np are material parameters.

The rate form of the plastic strain is defined as

$$\dot{\varepsilon}_p = \dot{P}\varepsilon_{eq} + P\dot{\varepsilon}_{eq} \tag{3.11}$$

Therefore, the total vertical strain is as below.

$$\varepsilon_p = \int_0^t \dot{\varepsilon}_p ds \tag{3.12}$$

3.2.2. Temperature- and frequency- dependent predictive framework

To consider the effect of temperature and aging on the rutting of pavements, a short-term aging model [38] and a long-term aging model [39] is first adopted to predict the viscosity of asphalt binder. Then, a complex modulus model for asphalt binder [2] is

used to obtained the dynamic modulus and phase angle based on the viscosity obtained in the first step. Next, a micromechanics model [40] is used and the complex modulus of asphalt concrete can be obtained based on the volume fraction and properties of each component in the mixture. Finally, the rutting of pavement can be predicted using the plasticity model proposed based on the property of asphalt concrete. The flowchart of rutting prediction is shown in Figure 3.1, and all the material properties needed as model inputs are summarized in Table 3.1. In this work, we assume that plastic deformation mainly happens in the asphalt concrete layer.

Table 3.1 Material properties needed as model inputs of asphalt concrete

Maximum specific gravity	Specific gravity of bitumen
Absorbed bitumen content	Percentage of air voids
Voids in mineral aggregates	Binder type
Bulk specific gravity of aggregates	Bitumen content
Voids filled with asphalt	Aggregate gradation
Viscosity temperature susceptibility parameters	Temperature

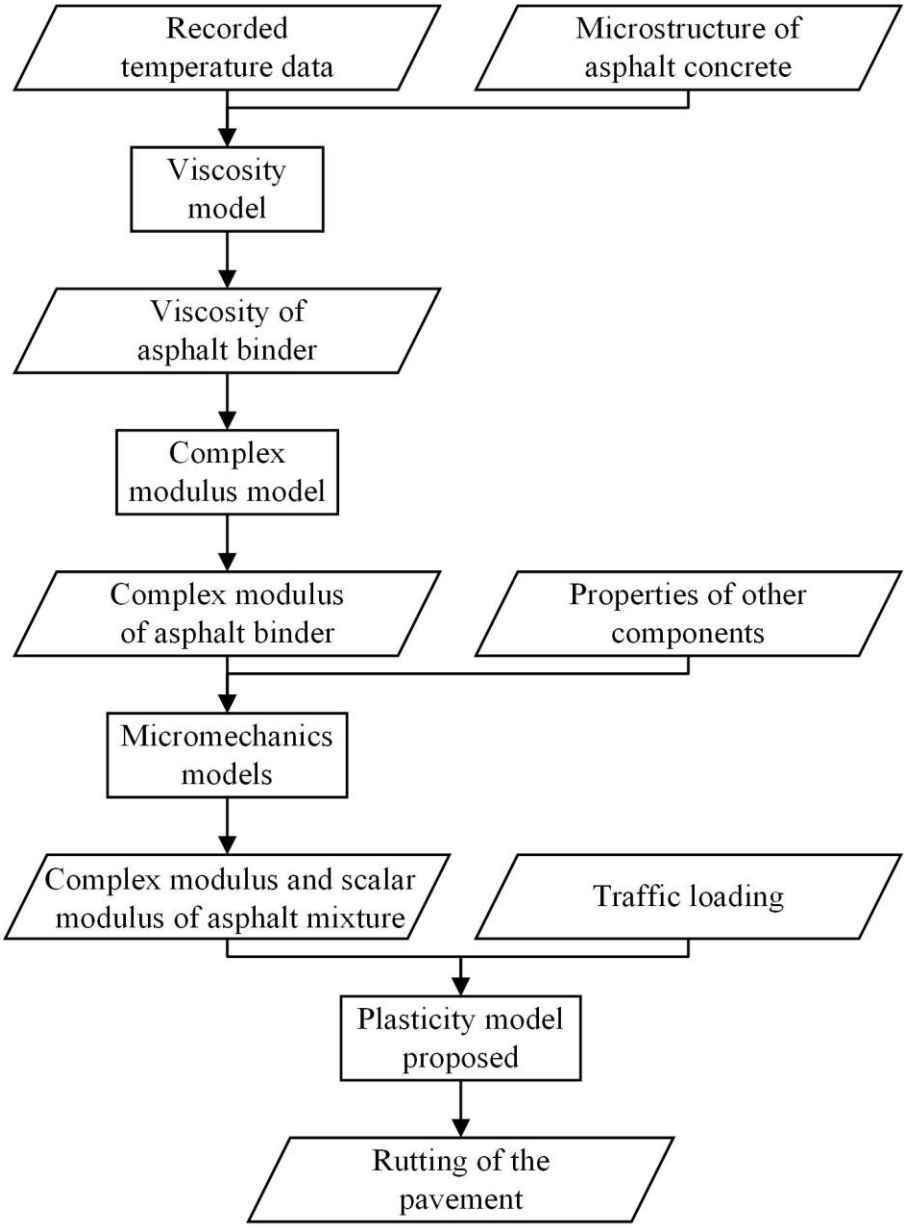

Figure 3.1 Flowchart for the rutting prediction of pavements.

3.3. Results and discussion

In this section, data from the WesTrack project [37] are adopted to verify the validity of the predictive framework, so we first do a brief introduction about the project, and then the predictive framework is verified based on the collected data.

3.3.1. Brief introduction about the WesTrack project

The main objective of WesTrack project was to evaluate the direct effects of deviation of materials and construction properties on hot mixed asphalt (HMA) pavement performance in a full-scale, accelerated field test. The test track was designed and constructed between October 1994 and October 1995. Traffic was initiated in March 1996 and was completed in February 1999. Two types of distress of the HMA, rutting and fatigue cracking, were well monitored and documented.

The structure of the test pavement was composed of four layers, an HMA layer of 150 mm, a base layer of 300 mm, a subbase layer of 460 mm and a subgrade layer of 150 mm. The reason why such layer thicknesses were selected was to reduce or prevent the permanent deformation in the base, subbase and subgrade layers. Thus, rutting mainly occurred in the HMA layer. To apply load on the pavement, four triple-trailer trailers pulled by 4 driverless tandem axle class 8 tractors were used. The cold inflation pressure of the tires was 690 kPa. Each axle of the vehicle train was loaded to 89 kN, except for the front axle which was 53 kN. The test speed around the track was 64 km/h, and the vehicle combinations were operated an average of 15 hours per day over the 2.5-year period.

In the test pavement, there were totally 26 test sections and the main difference was the composition of the asphalt concrete used in the HMA layer. One type of asphalt binder (PG 64-22) and one type of aggregates (partially crushed water-deposited gravel) were used to prepare the asphalt concrete, but there were 3 different aggregate gradations, 3 different asphalt binder content and 3 different air void contents in the asphalt concrete as shown in Table 3.2. The resilient modulus of subgrade layer was determined by doing falling weight deflectometer (FWD) tests and FWD measurements were taken at three different times prior to the initiation of track construction. The last two rounds of FWD data collection were in response to the slight alignment shifts of the track. The corresponding resilient modulus is as shown in Table 3.3. The corresponding resilient modulus tests for the base layer material and subbase layer material were performed in the laboratory and the corresponding values were documented [37].

Table 3.2 Experimental design for original 26 WesTrack sections

Design air void content	Aggregate gradation designation								
	Fine			Fine plus			Coarse		
	Design asphalt content								
	Low	Opt.	High	Low	Opt.	High	Low	Opt.	High
Low	-	04	18	-	12	09/12	-	23	25
Medium	02	01/15	14	22	11/19	13	08	05/24	07
High	03/16	17	-	10	20	-	26	06	-

*Numbers shown in each cell represent WesTrack section numbers.
*Sections whose section numbers are in blue are used for model calibration in this work.

Table 3.3 Summary of the backcalculated resilient modulus for subgrade materials

Test date	Resilient modulus (kPa)		
	North tangent	South tangent	Combined
October 1994	113,492	102,985	108,239
February 1995	40,182	32,858	36,520
April 1995	68,618	25,335	46,977

To collect data in the pavement, strain gages were installed in the HMA layer of each test section to measure the deformation in the HMA layer, and thermocouple temperature gages were installed in section 19 after construction at depths of 12.7 mm, 38.1 mm, 88.9 mm, 114.5 mm and 139.7 mm in the HMA layer. A device was also installed to measure permanent deformation at the interface of the subbase layer and base layer and at the interface of the base layer and HMA.

3.3.2. Model calibration and verification

To determine the parameters in the plasticity model, test sections are divided into two parts. 13 sections are used for model calibration and these sections include all the three different aggregate gradations, as shown in Table 3.2. The remaining sections are used for model verification. The time frame of material property predictions starts from October 1995 when the original construction was finished to March 1999 when all traffic stopped, while the time frame of rutting prediction starts from January 1996 when all traffic started to March 1999. Figure 3.2 shows the change of temperature of the pavement at the depth of 12.7 mm and Figure 3.3 shows the change of scalar modulus of section 4 at the depth of 12.7 mm. It can be seen that with the increase of temperature, the value of scalar modulus decreases. This is why we define the resistance to plasticity as a function of scalar modulus. During winter, low temperature can lead to a high scalar modulus, and a high scalar modulus corresponds to high resistance to rutting, so this captures that rutting rarely happens in winter.

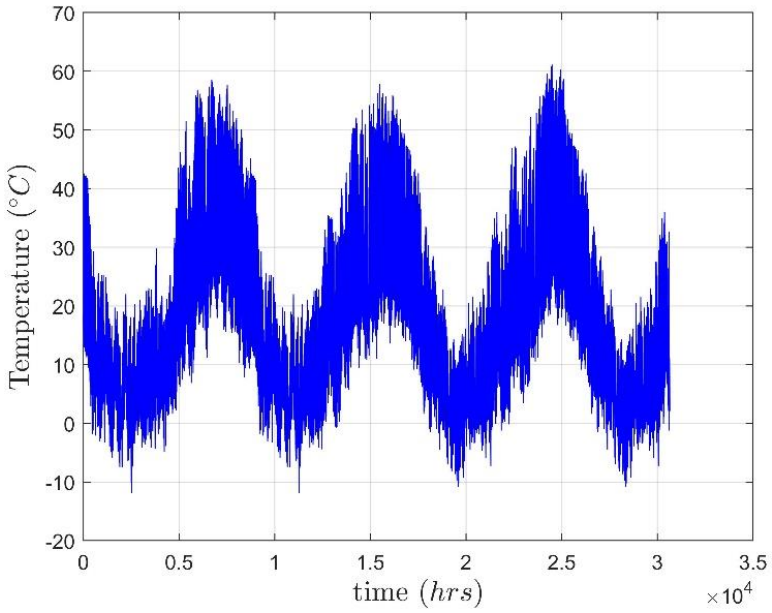

Figure 3.2 Temperature of the WesTrack pavement at the depth of 12.7 mm from October 1995 to March 1999.

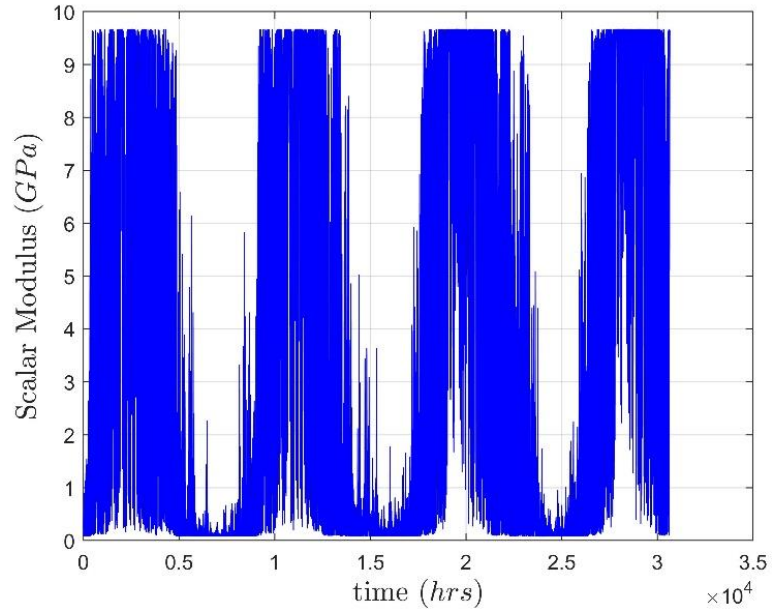

Figure 3.3 Scalar modulus of WesTrack section 4 at the depth of 12.7 mm from October 1995 to March 1999.

Figure 3.4 shows the relationship between the material parameters and scalar modulus. The scalar modulus corresponds to that of the 3635th hour after the construction of the pavement and the corresponding temperature at the depth of 12.7 mm is 49.5 °*C*. It can be seen from Figure 3.4(a) that *Ap* increases with the increase of the scalar modulus. This is because the resistance to rutting is a product of *Ap* and scalar modulus and it increases with the increase of scalar modulus or decrease with temperature. From Figures 4(a) and 4(b), it can be seen that *Kp* and *Np* have a negative relationship with the scalar modulus. It is because *Kp* and *Np* are related to the rate of rutting, and the rate of rutting decreases with the increase of scalar modulus or the decrease of temperature.

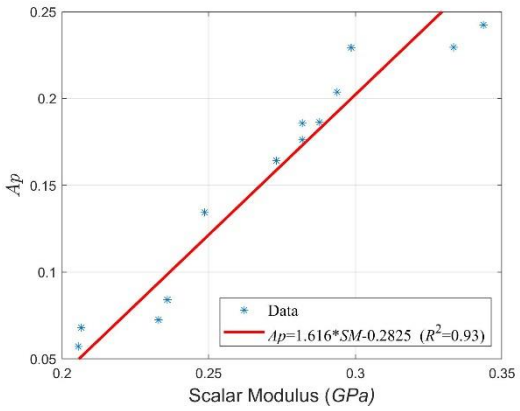

(a)

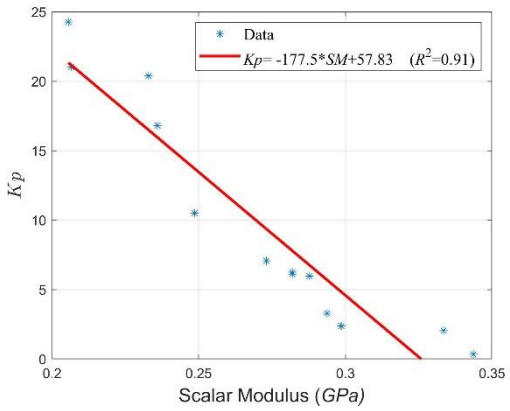

(b)

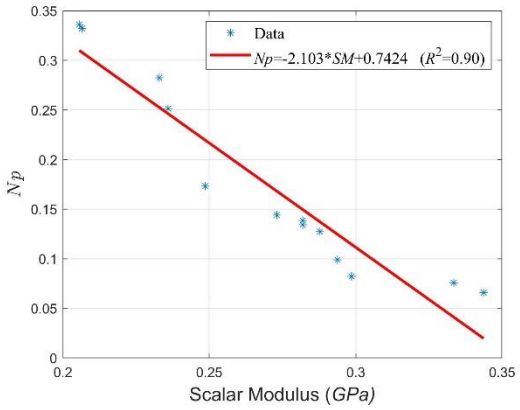

(c)

Figure 3.4 Relationships between material parameters and scalar modulus at 18.3℃.

Then, the relationships between material parameters and scalar modulus obtained during model calibration are used to do model verification. Figure 3.5 shows the comparison between test data and model predictions. It can be seen that the proposed model can capture the rutting of pavement well and it applies to pavements with different aggregate gradations.

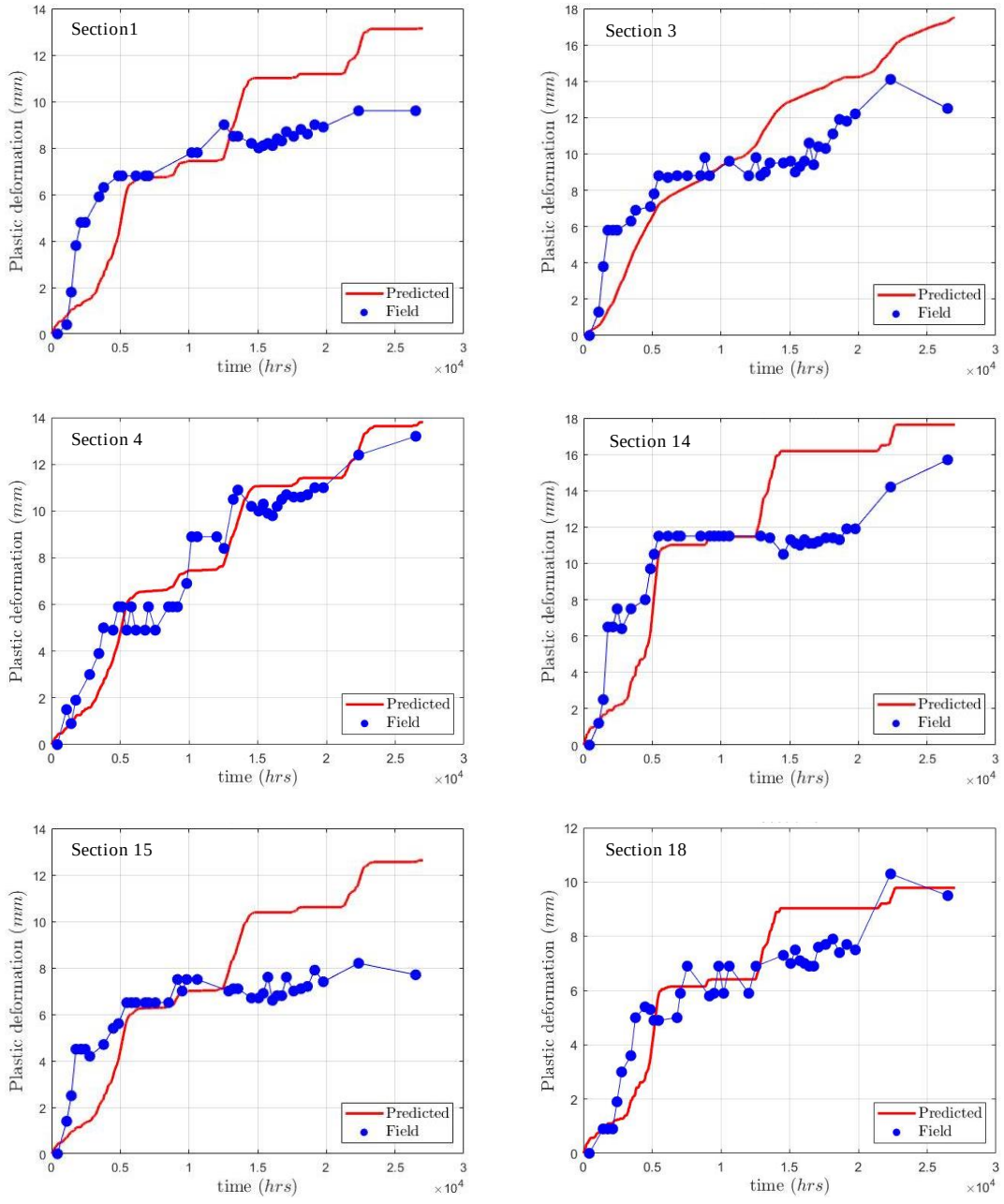

(a) Sections with fine aggregate gradation

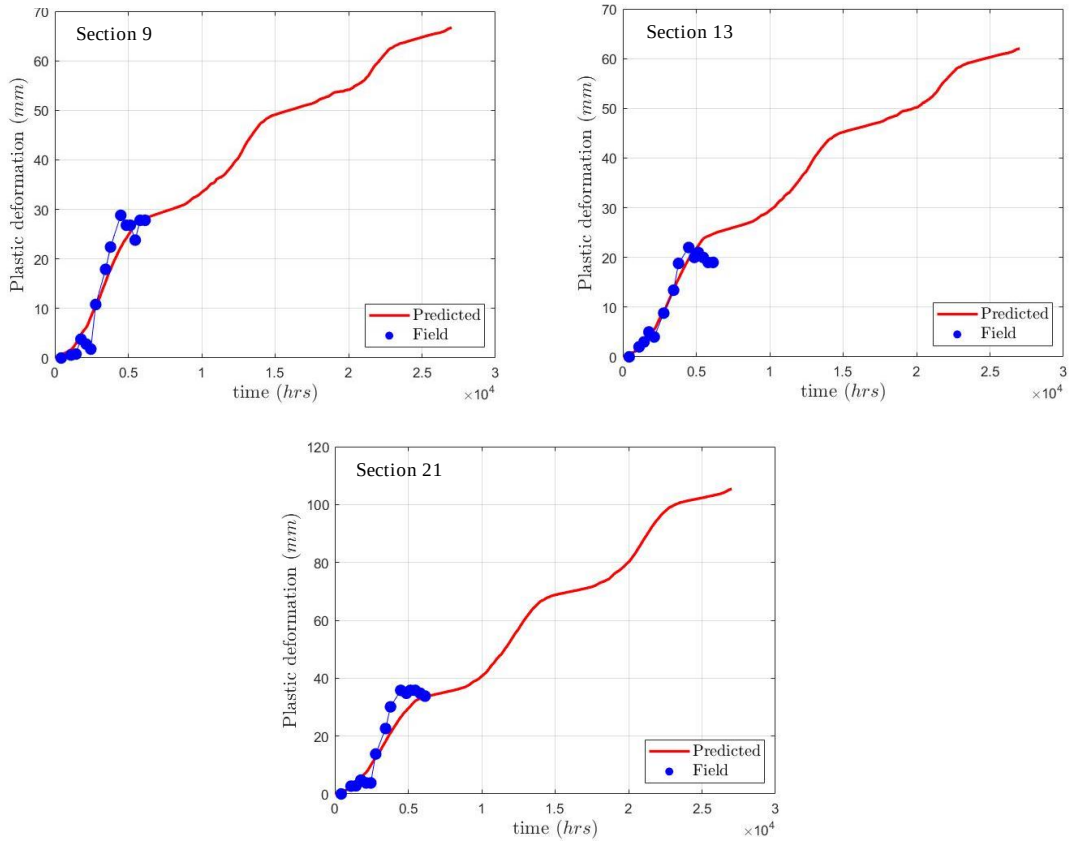

(b) Sections with fine plus aggregate gradation

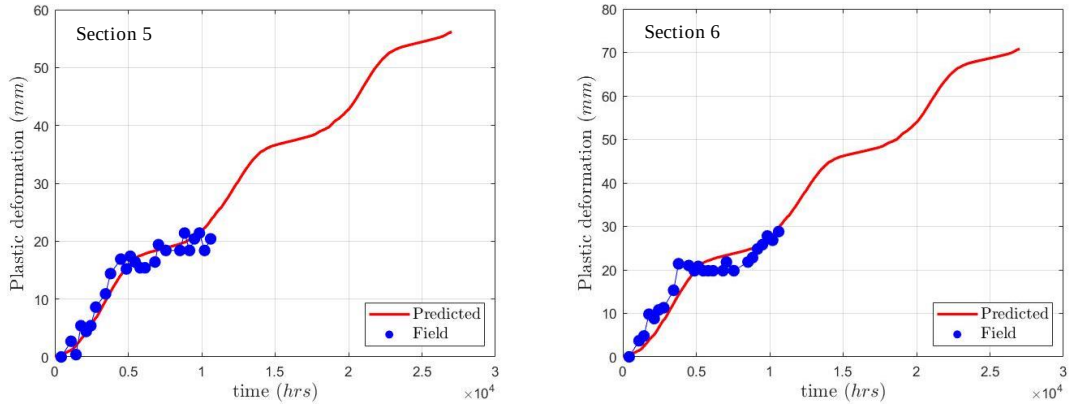

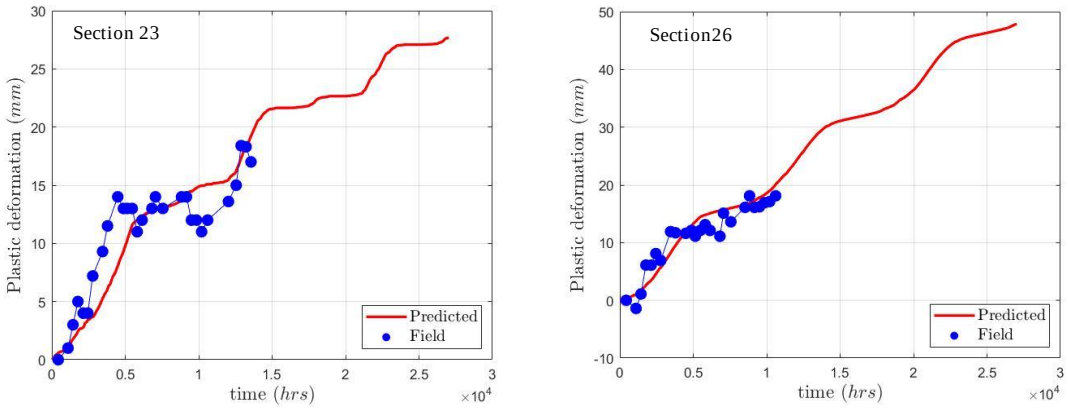

(c) Sections with coarse aggregate gradation

Figure 3.5 Comparison between WesTrack test data from January 1996 to March 1999 and model predictions for different test sections.

3.4. Conclusions

A new energy-based plasticity model is proposed and incorporated into a predictive framework to predict the rutting performance in the asphalt concrete layer of flexible pavements. The effect of loading rate, temperature and aging on the rutting performance can be considered and field test data is adopted to verify the validity of the plasticity model and predictive framework. The main findings are as below:

(1) The plasticity model and framework predict the rutting performance well, and they can be used to predict the rutting performance of asphalt concrete with different asphalt binder content, different aggregate gradation and different air void contents.

(2) The scalar modulus has a negative relation with temperature, and expressing plasticity resistance as a function of scalar modulus can capture the seasonal variation of the resistance to plasticity.

(3) The model parameters related to the rutting rate decrease with the increase of the scalar modulus, and this shows that the model can capture the phenomenon that rutting mainly happens in summer.

3.5. References

[1] M. Tia, B. Ruth, B. Birgisson, Influence of Aggregate Characteristics on Asphalt Mixture Properties and Performance, Bearing Capacity of Roads, Railways and Airfields, CRC Press2020, pp. 943-953.

[2] I. Onifade, B. Birgisson, Improved models for the prediction of asphalt binder dynamic shear modulus and phase angle, Construction and Building Materials 250 (2020) 118753.

[3] I. Onifade, K. Huang, B. Birgisson, Evaluation of models for binder dynamic shear modulus and phase angle, Advances in Materials and Pavement Performance Prediction II, CRC Press2020, pp. 462-466.

[4] D. Zhang, B. Birgisson, X. Luo, A new dynamic modulus predictive model for asphalt mixtures based on the law of mixtures, Construction and Building Materials 255 (2020) 119348.

[5] X. Luo, F. Ma, B. Birgisson, Z. Huang, Coupled mechanical and kinetic modeling of recovery in asphalt mixtures, Construction and Building Materials 254 (2020) 118889.

[6] Y. Dinegdae, I. Onifade, B. Birgisson, Reliability-Based Specification for Asphalt Concrete Pavements, Journal of Testing and Evaluation 48(1) (2019) 41-51.

[7] A. Bekele, N. Ryden, A. Gudmarsson, B. Birgisson, Automated non-contact resonance excitation method to assess low temperature dynamic modulus of asphalt concrete, Journal of nondestructive evaluation 38(2) (2019) 1-9.

[8] Y. Zhang, X. Luo, I. Onifade, X. Huang, R.L. Lytton, B. Birgisson, Mechanical evaluation of aggregate gradation to characterize load carrying capacity and rutting resistance of asphalt mixtures, Construction and Building Materials 205 (2019) 499-510.

[9] A.R. Archilla, S. Madanat, Development of a pavement rutting model from experimental data, Journal of transportation engineering 126(4) (2000) 291-299.

[10] G. Cerni, F. Cardone, A. Virgili, S. Camilli, Characterisation of permanent deformation behaviour of unbound granular materials under repeated triaxial loading, Construction and Building Materials 28(1) (2012) 79-87.

[11] Y.T. Choi, V. Subramanian, M.N. Guddati, Y.R. Kim, Incremental model for prediction of permanent deformation of asphalt concrete in compression, Transportation research record 2296(1) (2012) 24-35.

[12] Y.T. Choi, Y.R. Kim, Development of characterisation models for incremental permanent deformation model for asphalt concrete in confined compression, Road materials and pavement design 14(sup2) (2013) 266-288.

[13] F. Zhou, T. Scullion, L. Sun, Verification and modeling of three-stage permanent deformation behavior of asphalt mixes, Journal of Transportation Engineering 130(4) (2004) 486-494.

[14] H. Fang, Q. Liu, L. Mo, B. Javilla, B. Shu, S. Wu, Characterization of three-stage rutting development of asphalt mixtures, Construction and Building Materials 154 (2017) 340-348.

[15] D.N. Little, D.H. Allen, A. Bhasin, Modeling and design of flexible pavements and materials, Springer2018.

[16] J. Zhang, L.F. Walubita, A.N. Faruk, P. Karki, G.S. Simate, Use of the MSCR test to characterize the asphalt binder properties relative to HMA rutting performance–A laboratory study, Construction and Building Materials 94 (2015) 218-227.

[17] J.S. Chen, C.J. Tsai, How good are linear viscoelastic properties of asphalt binder to predict rutting and fatigue cracking?, Journal of materials engineering and performance 8(4) (1999) 443-449.

[18] L.F. Walubita, M. Ling, L.M.R. Pianeta, L. Fuentes, J.J. Komba, G.M. Mabrouk, Correlating the Asphalt-Binder MSCR Test Results to the HMA HWTT and Field Rutting Performance, Journal of Transportation Engineering, Part B: Pavements 148(3) (2022) 04022047.

[19] E. Masad, D. Olcott, T. White, L. Tashman, Correlation of fine aggregate imaging shape indices with asphalt mixture performance, Transportation Research Record 1757(1) (2001) 148-156.

[20] P.S. Kandhal, L. Cooley Jr, Coarse-versus fine-graded Superpave mixtures: comparative evaluation of resistance to rutting, Transportation research record 1789(1) (2002) 216-224.

[21] M. Singh, P. Kumar, A.K. Anupam, Effect of type of aggregate on permanent deformation of bituminous concrete mixes, Road Materials and Pavement Design 17(2) (2016) 417-433.

[22] M.M. Alamnie, E. Taddesse, I. Hoff, Advances in Permanent Deformation Modeling of Asphalt Concrete—A Review, Materials 15(10) (2022) 3480.

[23] R. Delgadillo, H.U. Bahia, The relationship between nonlinearity of asphalt binders and asphalt mixture permanent deformation, Road Materials and Pavement Design 11(3) (2010) 653-680.

[24] E. İskender, Rutting evaluation of stone mastic asphalt for basalt and basalt–limestone aggregate combinations, Composites Part B: Engineering 54 (2013) 255-264.

[25] Y. Zhang, M. Bernhardt, G. Biscontin, R. Luo, R.L. Lytton, A generalized Drucker–Prager viscoplastic yield surface model for asphalt concrete, Materials and Structures 48(11) (2015) 3585-3601.

[26] Y. Zhang, F. Gu, B. Birgisson, R.L. Lytton, Viscoelasticplastic–Fracture Modeling of Asphalt Mixtures under Monotonic and Repeated Loads, Transportation Research Record 2631(1) (2017) 20-29.

[27] Y. Deng, Y. Zhang, X. Shi, S. Hou, R.L. Lytton, Stress–strain dependent rutting prediction models for multi-layer structures of asphalt mixtures, International Journal of Pavement Engineering (2021) 1-18.

[28] E. Masad, S. Dessouky, D. Little, Development of an elastoviscoplastic microstructural-based continuum model to predict permanent deformation in hot mix asphalt, International Journal of Geomechanics 7(2) (2007) 119-130.

[29] T. You, R.K.A. Al-Rub, M.K. Darabi, E.A. Masad, D.N. Little, Three-dimensional microstructural modeling of asphalt concrete using a unified viscoelastic–viscoplastic–viscodamage model, Construction and Building Materials 28(1) (2012) 531-548.

[30] Y. Guo, I. Onifade, B. Birgisson, A mass specific volume-based viscoelastic damage model to characterize fatigue damage in asphalt mixtures, Construction and Building Materials 325 (2022) 126729.

[31] I. Onifade, Development of energy-based damage and plasticity models for asphalt concrete mixtures, KTH Royal Institute of Technology, 2017.

[32] I. Onifade, B. Birgisson, R. Balieu, Energy-based damage and fracture framework for viscoelastic asphalt concrete, Engineering Fracture Mechanics 145 (2015) 67-85.

[33] I. Onifade, R. Balieu, B. Birgisson, Interpretation of the Superpave IDT strength test using a viscoelastic-damage constitutive model, Mechanics of Time-Dependent Materials 20(3) (2016) 421-439.

[34] I. Onifade, Continuum Plasticity Mechanics (CPM)-An energy-based plasticity model-Application to asphalt concrete mixtures, International Journal of Solids and Structures (2016).

[35] K. Huang, I. Onifade, B. Birgisson, Calibration of mechanics-based pavement predictive framework for top-down cracking performance of flexible pavement considering wheel wander effect, Construction and Building Materials 306 (2021) 124792.

[36] K. Huang, I. Onifade, B. Birgisson, Rutting performance of flexible pavements using new energy-based potentials, Construction and Building Materials 266 (2021) 120896.

[37] J.A. Epps, Recommended performance-related specification for hot-mix asphalt construction: Results of the WesTrack project, Transportation Research Board2002.

[38] D. Zhang, B. Birgisson, X. Luo, I. Onifade, A new short-term aging model for asphalt binders based on rheological activation energy, Materials and Structures 52(4) (2019) 1-22.

[39] D. Zhang, B. Birgisson, X. Luo, I. Onifade, A new long-term aging model for asphalt pavements using morphology-kinetics based approach, Construction and Building Materials 229 (2019) 117032.

[40] I. Onifade, B. Birgisson, Microstructural integrity characterization of cement-based construction materials, Construction and Building Materials 307 (2021) 125012.

4. AN ENERGY-BASED PLASTICITY MODEL TO PREDICT THE PLASTIC DEFORMATION OF UNBOUND GRANUALAR MATERIALS

4.1. Introduction

The unbound granular material (UGM) consists of air voids, aggregate particles and water. It is widely used in the base layer of pavements, and the characteristics of UGMs can affect the performance of pavements considerably. For example, rutting of pavements is closely related to the plastic deformation in the base layer. UGMs exhibit an elastoplastic behavior and the total strain is composed of resilient strain and plastic strain. The resilient response is described using the resilient modulus, and it is defined as the ratio of the deviatoric stress to the resilient strain [1-3]. The plastic deformation arises from consolidation, distortion and attrition of granular materials [4, 5]. Therefore, the response of UGMs is related to its stress history, the current stress and strain level, microstructure and the degree of saturation [6]. According to the shakedown theory [7], under a low stress level, the plastic deformation develops quickly in the first few loading cycles, but the plastic deformation rate decreases with the load repetition and the permanent deformation approaches to a stable value. Therefore, the resilient modulus is obtained under a low stress level after a large number of loading cycles. However, if the load applied exceeds a limiting value called the shakedown load, the permanent deformation accumulates continuously with increasing load cycles and the material is prone to collapse [8].

To predict the plastic deformation of UGMs, many models have been proposed and these models can be divided into three categories, numerical models [9, 10], mechanistic-empirical models [11-15] and mechanics-based models [16, 17]. Due to the rapid development of microscale measuring devices, numerical methods have been adopted by many researchers. For example, Li et al. [18] did Monte Carlo simulations to analyze the effect of the morphology of randomly distributed aggregates on the deformation of UGMs. The shape and size of aggregates were determined using the X-ray CT technique [19, 20]. Although the numerical method considers the microstructure of aggregates well, it is time-consuming and expensive to acquire the digital images of aggregates and do simulations [21]. To save the calculation time, many mechanistic-empirical models [22-28] have been proposed. For example, in the MEPDG model [29], the plastic strain was expressed as a function of resilient strain imposed in the laboratory, average vertical strain in the base layer, and number of load cycles. To characterize the stress-dependent permanent deformation of UGMs, Gu et al. [30] introduced invariants of stress tensor to the MEPDG model. To further facilitate the determination of parameters in the MEPDG model, Gu et al. [31] analyzed test data and expressed the model parameters as functions of some easy-to-measure variables, like the dry density, aggregate gradation, moisture content, and morphological properties. Alnedawi et al. [32] proposed an artificial neural model to predict the plastic deformation of UGMs, and the model inputs included the number of load cycles, deviatoric stress, moisture content, coefficient of curvature, and coefficient of uniformity. Although mechanistic-empirical models can be implemented easily and are time-saving in rutting prediction, they can only be used to

predict the vertical plastic strain of the material and cannot reflect the mechanism of rutting. Compared with the other two methods mentioned above, mechanics-based models are developed based on traditional plasticity mechanics and can show the mechanism of rutting well. In the traditional plasticity theory, the yield surface or yield potential are usually expressed as a function of stress invariants, and associated or non-associated flow rules are adopted to show the evolution of plasticity in the material. However, UGMs are different from other elastoplastic materials, like steels. Traditional plasticity models, such as Drucker-Prager model [33], are not able to fully capture the behavior of UGMs. For example, under repeated loading tests, if the peak of stress in each load cycle is equal, the plastic deformation in a steel bar only happens in the first load cycle because of the strain-hardening effect [34]. This phenomenon can be captured by traditional plasticity models. For UGMs, under repeated load triaxial tests, the plastic deformation increases with load repetitions, as mentioned above. Therefore, traditional plasticity models are not able to predict the elastoplastic behavior of UGMs. To overcome this drawback, many researchers improved traditional plasticity models. For example, Chen et al. [35] proposed a cyclic plasticity model based on fuzzy plasticity theory to model the behavior of UGMs, and a memory function expressed as a function of the number of load cycles was included in the model. Chazallon et al. [36] proposed an elastoplastic model. The yield surface, plastic potential and isotropic hardening parameter were built based on a model for sands, where the shape function was expressed as a function of the number of load cycles. However, the main drawback of existing mechanics-based models is that they focus on the prediction of the macro-behavior of the material, and did not consider the effect of the material's

microstructure, like the gradation of the material. Experiments [37-40] have shown that the characteristics of UGMs influence the plastic deformation considerably. For example, the existence of some fine aggregates is good for the stability of UGMs, and a low content of fine aggregates can cause a low plasticity resistance of the material. However, if the content is very high, some fine aggregates will work as the lubricant, and the material resistance to plasticity will decrease [41, 42]. In addition, the number of load cycles is usually incorporated in existing models so that the plastic strain predicted could increase with the load cycles. However, according to the viewpoint in a study [43], the number of load cycles is a performance indicator instead of a material property, and it is not good at predicting the material performance. In the study [43], the material property was defined as a property that is not affected by the geometry or other extraneous conditions used to measure the property and it belongs to the material. The difference between the performance indicator and the material property can be illustrated using an example below. The maximum load of a steel bar can sustain is a performance indicator, while the maximum stress that the steel bar can sustain is a material property. Once the diameter of the steel bar is changed, the performance indicator will change, but the material property does not change. Therefore, the performance indicator can be used for material quality control, but it cannot be used for material behavior prediction [43]. Another drawback of existing models is that these models are usually stress-based or strain-based, and stress- or strain- based models cannot consider the effect of loading mode [44]. Therefore, a model whose parameters are determined based on controlled-stress loading test data, may not predict the material behavior under controlled-strain loading accurately.

In this work, an energy-based plasticity model for UGMs is proposed to predict the material behavior under the stress level lower than the shakedown load. This model can consider the effect of the moisture and microstructure of UGMs. Performance indicators, like the number of load cycles, are not included in the model, so the proposed model is independent of extraneous conditions used to measure the material properties. This work is organized as below. In the next section, a resilient modulus model from a previous study is introduced and used to predict the resilient behavior of the material. In the model, the effect of moisture is considered. Then, an energy-based plasticity model is proposed. To reflect the effect of the microstructure of UGMs, the yield criterion is expressed as a function of the coordination number of the primary load-carrying structure in the material. Next, some test data is adopted for model calibration and verification. The last section summarizes the main findings.

4.2. Model formulation

In this section, a resilient modulus model is adopted to predict the resilient response of UGMs. Then, an energy-based plasticity model is proposed to predict the plastic strain of the material under monotonic and cyclic loading.

(1) Resilient modulus prediction model

The stress state and moisture content have a great influence on the resilient response of UGMs. To predict the resilient behavior of UGMs, Lytton resilient modulus prediction model [45] is adopted in this work. It can predict the resilient modulus of the

materials under any specific stress state and moisture content, and its expression is as below:

$$Mr = k_1 P_a \left(\frac{I_1 - 3\theta f h_m}{P_a}\right)^{k_2} \left(\frac{\tau_{oct}}{P_a}\right)^{k_3} \tag{4.1}$$

with

$$f = 1 + \frac{S - 85}{15}\left(\frac{1}{\theta} - 1\right) \tag{4.2}$$

where I_1 is the first stress invariant, P_a is the atmospheric pressure, θ the volumetric water content, h_m is the matric suction, and f is the saturation factor, $1 \le f \le \frac{1}{\theta}$, and S is the degree of saturation (%).

(2) Energy-based plasticity model

A new second-order energy tensor is introduced and is defined as an integral of stress tensor with respect to mass specific volume. The corresponding tensor component is expressed as:

$$W_{ij} = \int_{v_1}^{v_2} \sigma_{ij} dv \tag{4.3}$$

where v is the mass specific volume, and its formulation is shown in Equation 4.4.

$$v = \det \mathbf{F} \cdot v_R \tag{4.4}$$

where det(**F**) is the determinant of deformation gradient, and v_R is the reference mass specific volume.

For pressure-dependent materials like UGMs, the plastic deformation is primarily driven by the energy of distortion in the material and the energy related to the volumetric changes. Similar to the decomposition of stress tensor, an energy tensor can also be decomposed into deviatoric part and volumetric part as below:

$$W_{ij} = W_{ij}^{D} + \frac{1}{3} W_{kk}^{V} \delta_{ij} \tag{4.5}$$

where W_{ij}^{D} and W_{kk}^{V} are the deviatoric and volumetric tensor components of the driving energy respectively, and δ_{ij} is the Kronecker delta.

The corresponding deviatoric and volumetric driving energy of plasticity are expressed as:

$$W_d = \sqrt{\frac{3}{2} W_{ij}^{D} W_{ij}^{D}} \tag{4.6}$$

$$W_v = \sqrt{W_{kk}^{V} W_{kk}^{V}} \tag{4.7}$$

where W_d is the deviatoric driving energy and W_v is the volumetric driving energy.

Then, the yield criterion for the material is expressed as below:

$$f^{p} = W_d + \alpha_s W_v - W_\beta - K_\beta = 0 \tag{4.8}$$

with

$$\alpha_s = \alpha \cdot \mathrm{sgn}(\sigma_{kk}) \tag{4.9}$$

where W_β is the initial resistance to plasticity and K_β is the hardening parameter. It is unnecessary to use a function to show the evolution of K_β, because its value equals the maximum value of ($W_d + \alpha_s W_v - W_\beta$) in the history. During the simulation, the maximum

value can be captured using numerical computing or finite element software, like MATLAB and COMSOL Multiphysics. Therefore, the yield function is always less than or equal to 0. α_s is the moisture and stress-state sensitivity parameter and sgn(·) is the signum function. The expression for α is as below:

$$\alpha = k_4 \times cn_{PS} \left(\frac{I_1 - 3\theta fh_m}{P_a}\right)^{k_2} \left(\frac{\tau_{oct}}{P_a}\right)^{k_3} \tag{4.10}$$

with

$$cn_{PS} = 2.827 \times \left[\frac{n_{PS}}{100}\right]^{-1.069} \tag{4.11}$$

where the function of α and the resilient modulus function have the same parameters, k_2 and k_3, and cn_{PS} and n_{PS} are the coordination number and porosity of the primary structure (PS) respectively [46-48].

The PS of UGMs is the primary load carrying structure in the material, and it is composed of coarse aggregates within a range of grain size. The coordination number means the average number of contact points per aggregate particle in the PS, and its porosity is the ratio of the void volume in the PS to the volume of aggregate particles within the PS. The PS is identified based on the packing theory and consideration of the densest and loosest possible packing arrangements by assuming the particles are spherical. The interaction between two consecutive sieve sizes occurs if the following condition can be satisfied [46-48]:

$$\frac{1.1 \times D_1 D_2}{\sqrt[3]{D_2^3 + 2.36 \times D_1^3}} \le d_{w,avg} \le \frac{1.1 \times D_1 D_2}{\sqrt[3]{2.36 \times D_1^3 + D_2^3}} \tag{4.12}$$

where D_1 and D_2 are the consecutive sieve sizes, and $d_{w,avg}$ is the weighted-average particle diameter between particles in the PS.

In the traditional plasticity theory, plastic strain is work-conjugate with stress and it is determined based on a stress-based plastic potential. In this work, a plasticity tensor is defined and it is work-conjugate with energy. The plasticity tensor can be obtained based on the associated flow rule as below:

$$\mathbf{P} = \dot{\lambda} \frac{\partial f^{p}}{\partial \mathbf{W}} \tag{4.13}$$

$$\dot{\lambda} = K \cdot N \left\langle \frac{W_d + \alpha_s W_v}{W_\beta} - 1 \right\rangle^{N-1} \tag{4.14}$$

where λ is the Lagrange multiplier and $\langle \cdot \rangle$ is the Macaulay bracket.

Finally, the plastic strain tensor is expressed as:

$$\boldsymbol{\varepsilon}_{\mathbf{p}} = \mathbf{P} \varepsilon_{eq} \tag{4.15}$$

where ε_{eq} is the equivalent strain.

4.3. Results and discussion

All the test data used in this work are from a previous study [49], where the characteristics of three different types of UGMs, including unbound sandstone aggregates, unbound limestone aggregates and unbound granite aggregates, were studied. In the first part, the materials and testing are introduced. Then, resilient modulus test data and monotonic triaxial compression test data are used for model calibration. Finally, repeated load tri-axial test data is used to verify the model validity. The reference mass specific

volumes of the unbound limestone, unbound sandstone and unbound granite aggregates are 7×10^{-3} m^3/kg, 7.3×10^{-3} m^3/kg and 7.6×10^{-3} m^3/kg, respectively. The simulation is realized using COMSOL Multiphysics.

(1) Materials and testing

To study physical properties of these UGMs, different laboratory tests were conducted. They included standard proctor (ASTM D 792), sieve analysis (ASTM C136-06), specific gravity and absorption, coarse aggregate angularity (ASTM D 5821), and Micro-Deval test (ASTM D 6928). Part of the physical properties and gradation of these materials are shown in Table 4.1 and Figure 4.1 respectively. To achieve the desired water contents, the materials were first oven dried at a prespecified temperature and then mixed with water at the specified moisture content. Based on AASHTO-T307, a split mold with an inner diameter of 150 mm and a height of 350 mm, was used to prepare samples. To achieve a uniform compaction throughout the thickness, samples were compacted in six-50 mm layers. These samples were enclosed in two latex membranes with a thickness of 0.3 mm for the convenience of testing. The diameter and height of these samples were 6 inches and 12 inches respectively.

Three types of tri-axial tests were performed to study the behavior of UGMs under loading, and they included the resilient modulus test, the monotonic triaxial compression test and repeated load tri-axial test. The material testing system (MTS) 810 machine was used for the tests, and two Linearly Variable Differential Transducers (LVDT) were placed between the top platen and base of the cell to measure the axial displacement. Air

was used as the confining fluid to samples. For the resilient modulus test, it was performed based on AASHTO-T307 [50]. 10000 load cycles with a confining stress of 15 psi and a deviator stress of 14 psi were first applied on the samples. Then, the resilient modulus was calculated at specific deviator stress cycles and constant confining pressure, and it equals the ratio of the maximum deviator stress to the recoverable elastic strain. The triaxial compression test was performed at three different confining pressures, 2, 7 and 10 psi, and the axial strain rate was less than ten percent strain per hour. For the repeated load triaxial test, a haversine load with a peak stress of 30 psi and a duration of 0.1 secs, was applied. After each load cycle, there was a rest period of 0.9 seconds, as shown in Figure 4.2. Total 10000 load cycles were applied on the samples at a constant confining pressure of 3 psi. The confining pressure matches the field measurement of lateral confining pressure within the base course layer [51].

Table 4.1 Physical characteristics of the unbound granular materials

Property	Limestone	Sandstone	Granite
Specific gravity	2.708	2.642	2.671
Absorption (%)	1.7	2.1	0.9
Micro-Deval, Loss (%)	13	11.5	5.5
Maximum dry density (lb/ft^3)	142.0	136.2	132.0
Optimum moisture content (%)	6.5	7.1	6
Degree of saturation (%)	80.7	88	76.3

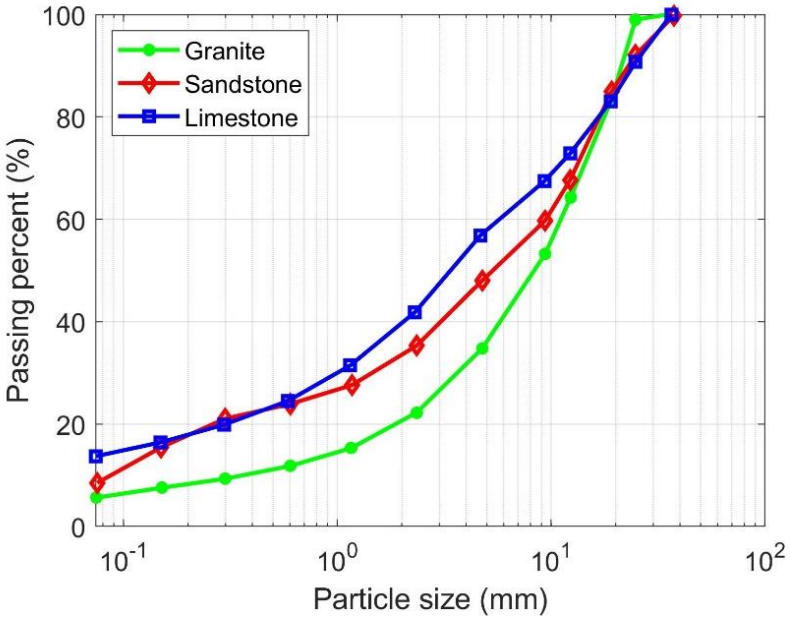

Figure 4.1 Gradation of the unbound granular materials.

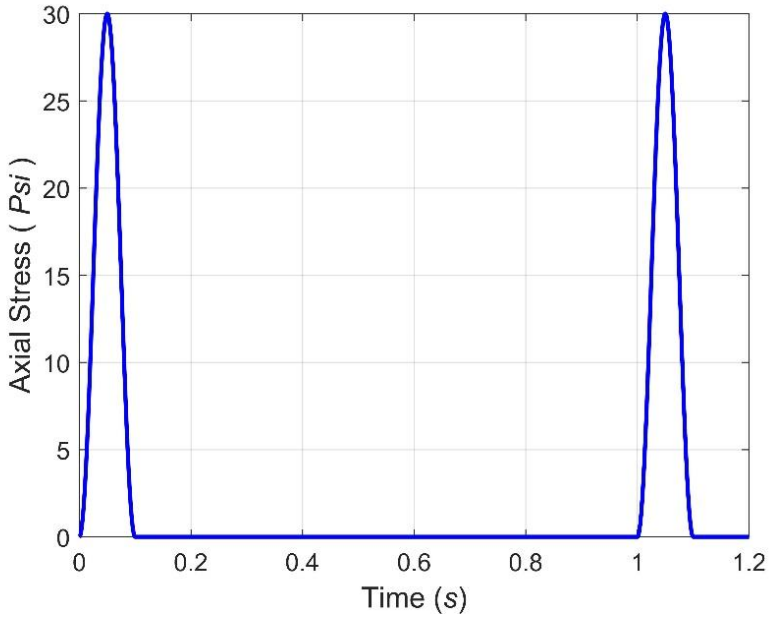

Figure 4.2 Applied axial stress on the sample under repeated load tri-axial testing.

(2) Model calibration

To determine material parameters in the proposed model, the resilient modulus test data are used first to obtain the values of k_1, k_2 and k_3, based on Equation 4.1 by doing fitting. Next, the coordination numbers of UGMs are determined based on the microstructure and gradation of the materials, and then the remaining parameters, k_4 and W_β, in the initial yield criterion are determined by fitting the test data using Equation 4.8. Finally, by fitting the stress-strain test data, parameters, K and N, are determined. Therefore, values of all the parameters can be obtained using the resilient modulus test data and the monotonic load triaxial test data.

Figure 4.3 shows the determination of the resilient modulus. It can be seen that the resilient modulus increases with the increase of bulk stress. Compared with the other two materials, unbound sandstone aggregates have the lowest resilient modulus, and this means under the same loading condition, unbound sandstone aggregates have the largest resilient strain. It can also be seen that the Lytton resilient modulus prediction model [45] captures the material property well. The corresponding parameters in the resilient modulus model are summarized in Table 4.2.

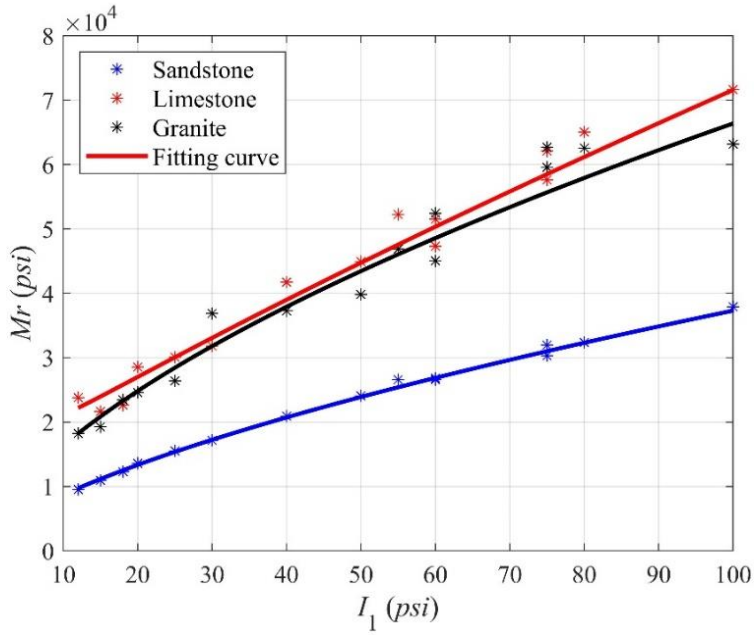

Figure 4.3 Determination of the resilient modulus determined by fitting test data [49] using the Lytton resilient modulus prediction model [45].

Figure 4.4 shows the determination of the initial yield criterion, and the values of all the parameters are summarized in Table 4.1. The value of cn_{PS} is from a former study [46], where the same test date was adopted. It can be seen from Table 4.2 that the value of W_β for the unbound sandstone aggregates is the smallest, and this means that plastic deformation happens easily in the unbound sandstone aggregates. Unbound granite aggregates have the largest value of W_β, and it is because it has the lowest porosity and the highest coordination number, so the friction force in the material is large. It can also be seen that compared with unbound limestone aggregates, unbound sandstone aggregates have a less W_β, but a larger cn_{PS}. That is because the plastic deformation in UGMs is also affected by the texture of materials and the proposed model does not consider the effect of materials' texture.

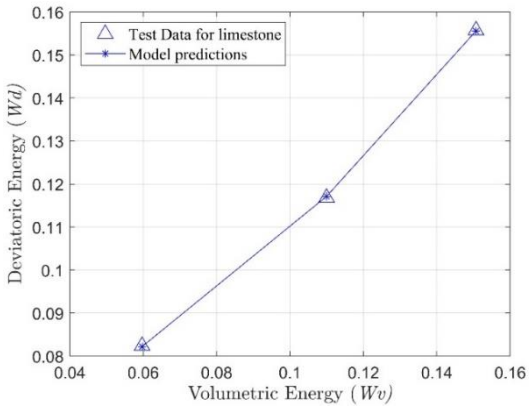

(a)

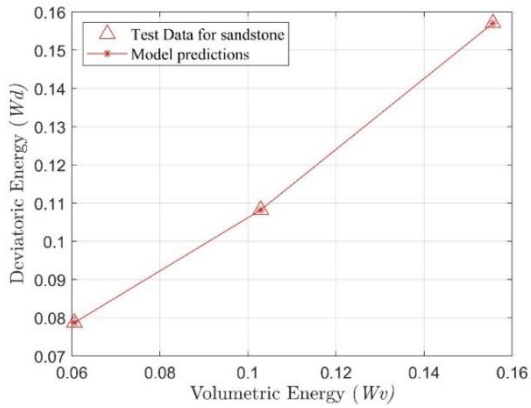

(b)

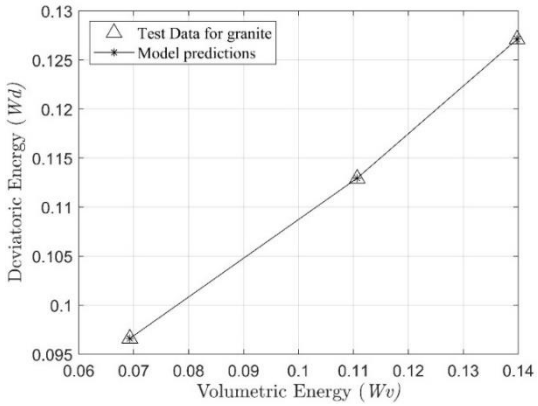

(c)

Figure 4.4 Determination of the initial yield criterion for (a) unbound limestone aggregates, (b) unbound sandstone aggregates and (c) unbound granite aggregates. (Test data is from a previous study [49]).

Table 4.2 Material parameters obtained from test data [49] in the plasticity model

Unbound materials	W_β (Pa·m^3/kg)	n_{PS} (%)	cn_{PS}	k_1	k_2	k_3	k_4	K	N
Limestone	0.062	66.68 [46]	4.4 [46]	795.2	0.905	-0.092	0.030	0.08	0.19
Sandstone	0.058	46.31 [46]	6.4 [46]	689.9	0.683	-0.036	0.034	0.12	0.25
Granite	0.083	38.22 [46]	7.9 [46]	1176.1	0.719	-0.109	0.014	0.04	0.10

Figure 4.5 shows the comparison between model predictions and test data for unbound limestone aggregates. One group of test data is used to obtain the values of K and N, and the other two groups of test data are used to verify the validity. It can be seen that there is a good match between test data and model predictions, so the proposed model performs well on the prediction of the material behavior under different stress level. Values of K and N for these three different materials are summarized in Table 4.2 and it can be seen that the values of K and N are largest for unbound sandstone aggregates. Since K and N are related to the rate of plastic deformation, this means that under loading, the plastic deformation develops very quickly in unbound sandstone aggregates, compared with other two materials.

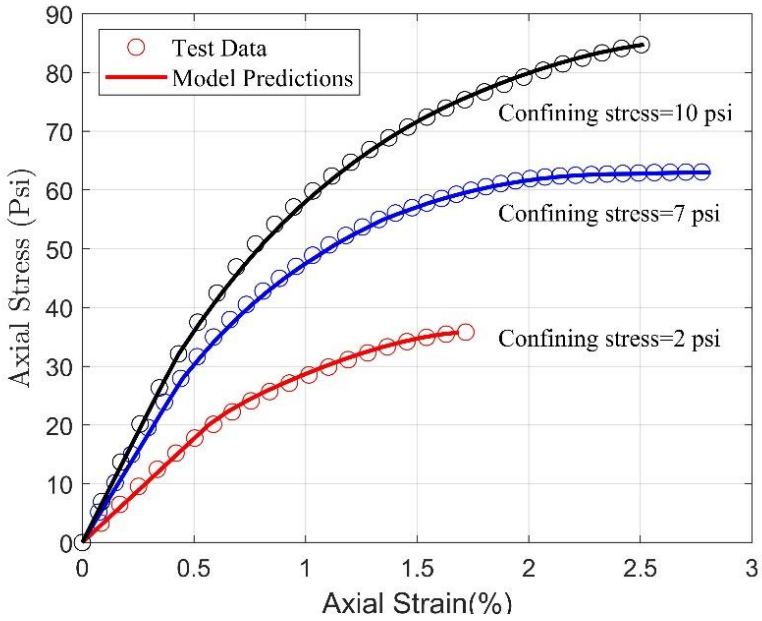

Figure 4.5 Comparison between test data for unbound limestone materials [49] and model predictions.

(3) Model verification

To verify the validity of the proposed model, the proposed plasticity model is used to predict the material behavior under repeated load triaxial testing, and the model predictions are compared with the test data. The simulation results for unbound granite aggregates in the first 12 load cycles are shown in Figures 4.6 and 4.7. It can be seen that plastic deformation develops in each loading cycle and it increases monotonically with load cycles. Figure 4.8 shows the comparison between model predictions and test data, and it can be seen that the plastic strain of unbound sandstone aggregates is largest and model predictions match the test data well.

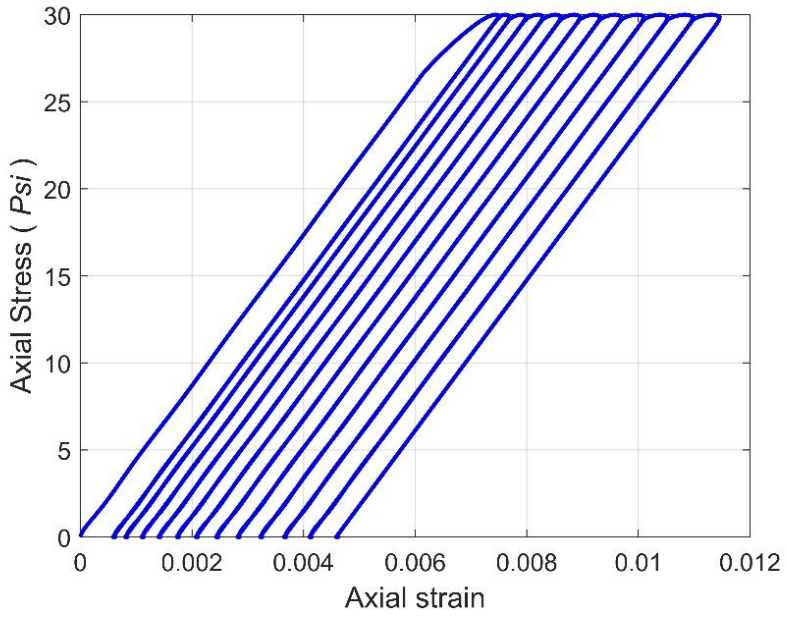

Figure 4.6 Stress-strain relationship predicted for granite materials in the first 12 loading cycles.

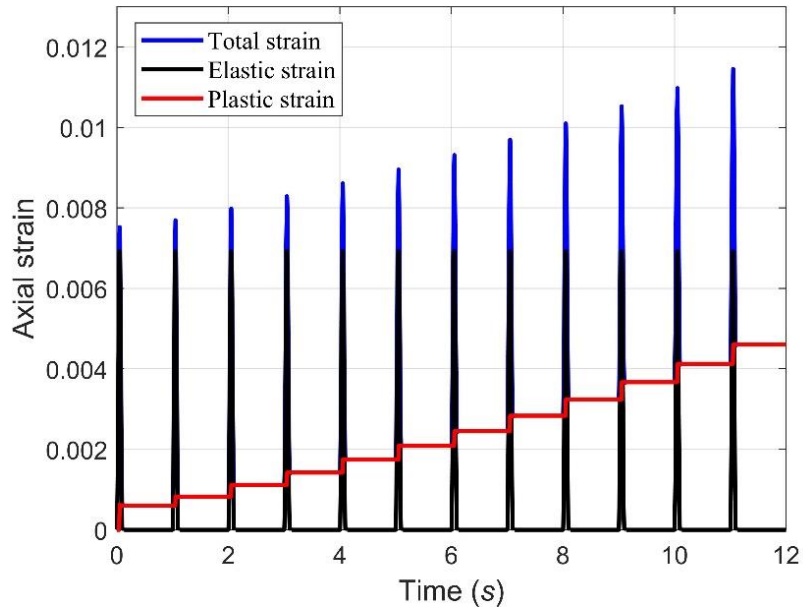

Figure 4.7 Development of strains predicted for granite materials in the first 12 loading cycles.

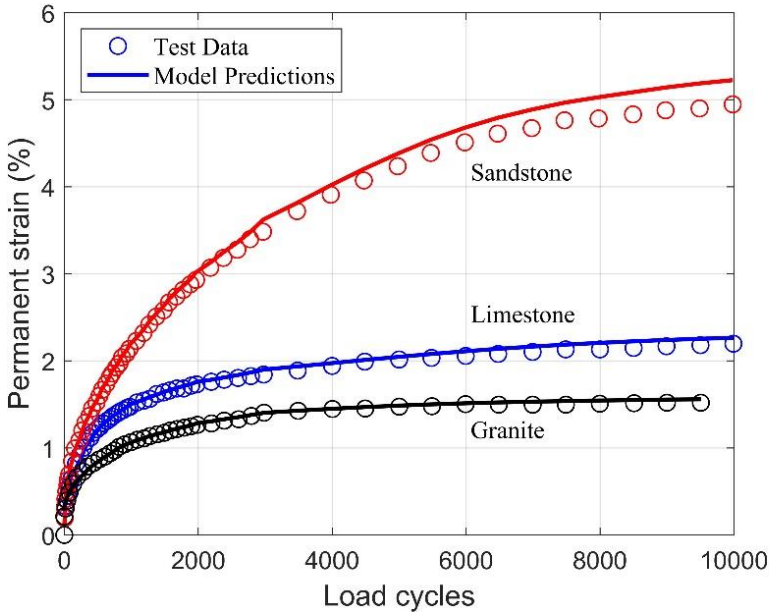

Figure 4.8 Comparison between model predictions and test data [49] under repeated loading.

4.4. Conclusions

To predict the plastic deformation of UGMs, an energy-based plasticity model is proposed. The effects of stress and strain state, moisture and microstructure of the materials are considered. The main findings are summarized as follows:

(1) The proposed model can predict the behavior of UGMs under different stress state accurately, and it can capture the increase of plastic strain under controlled-stress repeated load triaxial testing.

(2) No performance indicator is included in the proposed model, so the model is independent of the geometry and other extraneous conditions used to measure the material properties.

(3) The effect of the microstructure of the material on the rutting performance is considered by the porosity and coordination number of the primary loading carrying structure. The initial plasticity resistance of UGMs can be evaluated using the coordination number of PS, and a large coordination number corresponds to a high initial resistance.

(4) Compared with unbound granite aggregates and unbound limestone aggregates, unbound sandstone aggregates have the least resistance to plasticity and the largest rate of plastic deformation.

4.5. References

[1] F. Gu, H. Sahin, X. Luo, R. Luo, R.L. Lytton, Estimation of resilient modulus of unbound aggregates using performance-related base course properties, Journal of Materials in Civil Engineering 27(6) (2015) 04014188.

[2] I.L. Al-Qadi, H. Wang, E. Tutumluer, Dynamic analysis of thin asphalt pavements by using cross-anisotropic stress-dependent properties for granular layer, Transportation Research Record 2154(1) (2010) 156-163.

[3] E. Masad, D. Little, R. Lytton, Modeling nonlinear anisotropic elastic properties of unbound granular bases using microstructure distribution tensors, International Journal of Geomechanics 4(4) (2004) 254-263.

[4] F. Lekarp, U. Isacsson, A. Dawson, State of the art. I: Resilient response of unbound aggregates, Journal of transportation engineering 126(1) (2000) 66-75.

[5] F. Lekarp, U. Isacsson, A. Dawson, State of the art. II: Permanent strain response of unbound aggregates, Journal of transportation engineering 126(1) (2000) 76-83.

[6] A. Adu-Osei, D.N. Little, R.L. Lytton, Cross-anisotropic characterization of unbound granular materials, Transportation Research Record 1757(1) (2001) 82-91.

[7] A.T. Papagiannakis, E.A. Masad, Pavement design and materials, John Wiley & Sons, 2008.

[8] S. Saha, F. Gu, X. Luo, R.L. Lytton, Use of an artificial neural network approach for the prediction of resilient modulus for unbound granular material, Transportation Research Record 2672(52) (2018) 23-33.

[9] J. Li, J. Zhang, A. Zhang, J. Peng, Evaluation on deformation behavior of granular base material during repeated load triaxial testing by discrete-element method, International Journal of Geomechanics 22(11) (2022) 04022210.

[10] A. Adu-Osei, Characterization of unbound granular layers in flexible pavements, Texas A&M University, 2000.

[11] X. Luo, F. Gu, Y. Zhang, R.L. Lytton, D. Zollinger, Mechanistic-empirical models for better consideration of subgrade and unbound layers influence on pavement performance, Transportation Geotechnics 13 (2017) 52-68.

[12] S.S. Nagula, R.G. Robinson, J.M. Krishnan, Mechanical Characterization of Pavement Granular Materials Using Hardening Soil Model, International Journal of Geomechanics 18(12) (2018) 04018157.1-04018157.13.

[13] S. Hao, T. Pabst, Estimation of permanent deformation behaviour of crushed waste rocks using multistage repeated load triaxial and CBR tests, International Journal of Pavement Engineering (2022) 1-14.

[14] E.L. Pérez-González, J.-P. Bilodeau, G. Doré, Plastic strain rate in granular materials as a function of stress history: a probabilistic approach for the PBD model, International Journal of Pavement Engineering (2022) 1-12.

[15] A. Alnedawi, B. Kafle, S. Ullah, W. Kerr, Investigation of non-standard unbound granular materials under cyclic loads: experimental and regression analyses, International Journal of Pavement Engineering 23(9) (2022) 2998-3010.

[16] Y. Zhang, F. Gu, X. Luo, B. Birgisson, R.L. Lytton, Modeling stress-dependent anisotropic elastoplastic unbound granular base in flexible pavements, Transportation Research Record 2672(52) (2018) 46-56.

[17] R. Bonaquist, M.W. Witczak, Plasticity modeling applied to the permanent deformation response of granular materials in flexible pavement systems, Transportation research record 1540(1) (1996) 7-14.

[18] J. Li, J. Zhang, X. Yang, A. Zhang, M. Yu, Monte Carlo simulations of deformation behaviour of unbound granular materials based on a real aggregate library, International Journal of Pavement Engineering 24(1) (2023) 2165650.

[19] C. Jin, F. Zou, X. Yang, Z. You, 3D quantification for aggregate morphology using surface discretization based on solid modeling, Journal of Materials in Civil Engineering 31(7) (2019) 04019123.

[20] H. Wei, J. Li, F. Wang, J. Zheng, Y. Tao, Y. Zhang, Numerical investigation on fracture evolution of asphalt mixture compared with acoustic emission, International Journal of Pavement Engineering 23(10) (2022) 3481-3491.

[21] M.R. Pouranian, M. Shishehbor, J.E. Haddock, Impact of the coarse aggregate shape parameters on compaction characteristics of asphalt mixtures, Powder Technology 363 (2020) 369-386.

[22] K.-H. Tseng, R.L. Lytton, Prediction of permanent deformation in flexible pavement materials, Implication of Aggregates in the Design, Construction and Performance of Flexible Pavements. ASTM STP 1016 (1989) 154-172.

[23] R.D. Barksdale, Laboratory evaluation of rutting in base course materials, Presented at the Third International Conference on the Structural Design of Asphalt Pavements, Grosvenor House, Park Lane, London, England, Sept. 11-15, 1972.

[24] G.T. Sweere, Unbound granular bases for roads, (1992).

[25] A. Alsalman, R. Kareem, C.N. Dang, J.R. Martí-Vargas, W.M. Hale, Prediction of modulus of elasticity of UHPC using maximum likelihood estimation method, Structures, Elsevier, 2022, pp. 1308-1320.

[26] L. Korkiala-Tanttu, Verification of rutting calculation for unbound road materials, Proceedings of the institution of civil engineers-transport, Thomas Telford Ltd, 2009, pp. 107-114.

[27] L.C. Chow, D. Mishra, E. Tutumluer, Framework for development of an improved unbound aggregate base rutting model for mechanistic–empirical pavement design, Transportation Research Record 2401(1) (2014) 11-21.

[28] J. Zhang, J. Peng, A. Zhang, J. Li, Prediction of permanent deformation for subgrade soils under traffic loading in Southern China, International Journal of Pavement Engineering 23(3) (2022) 673-682.

[29] N.C.H.R. Program, Harmonized test methods for laboratory determination of resilient modulus for flexible pavement design, Final Rep. NCHR Project No. 1-28 A (2003).

[30] F. Gu, Y. Zhang, C.V. Droddy, R. Luo, R.L. Lytton, Development of a new mechanistic empirical rutting model for unbound granular material, Journal of Materials in Civil Engineering 28(8) (2016) 04016051.

[31] F. Gu, Y. Zhang, X. Luo, H. Sahin, R.L. Lytton, Characterization and prediction of permanent deformation properties of unbound granular materials for pavement ME design, Construction and Building Materials 155 (2017) 584-592.

[32] A. Alnedawi, R. Al-Ameri, K.P. Nepal, Neural network-based model for prediction of permanent deformation of unbound granular materials, Journal of Rock Mechanics and Geotechnical Engineering 11(6) (2019) 1231-1242.

[33] Y. Zhang, M. Bernhardt, G. Biscontin, R. Luo, R.L. Lytton, A generalized Drucker–Prager viscoplastic yield surface model for asphalt concrete, Materials and Structures 48(11) (2015) 3585-3601.

[34] P.M. Dixit, U.S. Dixit, Plasticity: Fundamentals and Applications, CRC press, 2014.

[35] C. Chen, L. Ge, J. Zhang, Modeling permanent deformation of unbound granular materials under repeated loads, International journal of geomechanics 10(6) (2010) 236-241.

[36] C. Chazallon, P. Hornych, S. Mouhoubi, Elastoplastic model for the long-term behavior modeling of unbound granular materials in flexible pavements, International Journal of Geomechanics 6(4) (2006) 279-289.

[37] Mohammad, Shafiqur, Rahman, Sigurdur, Erlingsson, Moisture influence on the resilient deformation behaviour of unbound granular materials: International Journal of Pavement Engineering: Vol 17, No 9, International Journal of Pavement Engineering (2015).

[38] J. Kwon, S.H. Kim, E. Tutumluer, M.H. Wayne, Characterisation of unbound aggregate materials considering physical and morphological properties, International Journal of Pavement Engineering 18(3-4) (2015) 303-308.

[39] J. Ren, C. Yin, Investigating mechanical characteristics of aggregate structure for road materials, International Journal of Pavement Engineering (7) (2020) 1-15.

[40] R.S. Ashtiani, D.N. Little, M. Rashidi, Neural network based model for estimation of the level of anisotropy of unbound aggregate systems, Transportation Geotechnics 15 (2018) 4-12.

[41] B.I. Siswosoebrotho, P. Widodo, E. Augusta, The influence of fines content and plasticity on the strength and permeability of aggregate for base course material, Proceedings of the Eastern Asia society for transportation studies, Citeseer, 2005, pp. 845-856.

[42] M. Ohiduzzaman, S. Lo, O. Craciun, Influence of fines content on unbound granular base materials (UGB) under cyclic axial and radial stress, GeoCongress 2012: State of the Art and Practice in Geotechnical Engineering2012, pp. 1418-1427.

[43] D.N. Little, D.H. Allen, A. Bhasin, Modeling and design of flexible pavements and materials, Springer, 2018.

[44] Y. Guo, I. Onifade, B. Birgisson, A mass specific volume-based viscoelastic damage model to characterize fatigue damage in asphalt mixtures, Construction and Building Materials 325 (2022) 126729.

[45] R. Lytton, Foundations and pavements on unsaturated soils, PROCEEDINGS OF THE FIRST INTERNATIONAL CONFERENCE ON UNSATURATED SOILS/UNSAT'95/PARIS/FRANCE/6-8 SEPTEMBER 1995. VOLUME 3, 1996.

[46] T.F. Yideti, B. Birgisson, D. Jelagin, A. Guarin, Packing theory-based framework for evaluating resilient modulus of unbound granular materials, International Journal of Pavement Engineering 15(8) (2014) 689-697.

[47] T.F. Yideti, B. Birgisson, D. Jelagin, A. Guarin, Packing theory-based framework to evaluate permanent deformation of unbound granular materials, International Journal of Pavement Engineering 14(3) (2013) 309-320.

[48] T.F. Yideti, Packing theory-based framework for performance evaluation of unbound granular materials, KTH Royal Institute of Technology, 2014.

[49] A.M. Austin, Fundamental characterization of unbound base course materials under cyclic loading, (2009).

[50] A. T307, Standard method of test for determining the resilient modulus of soils and aggregate materials, American Association of State Highway and Transportation Officials, 1999.

[51] R.D. Barksdale, J. Lago Alba, N.P. Khosla, R. Kim, P.C. Lambe, M. Rahman, Laboratory determination of resilient modulus for flexible pavement design, 1997.

5. MICROMECHANICS MODELING ON THE PREDICTION OF SOIL-WATER CHARACTERISTIC CURVES

5.1. Introduction

The soil-water characteristic curve (SWCC) is used to describe the relationship between the water content and matric suction in unsaturated soils, which is composed of soil solids, water, air and air-water interfaces [1]. The SWCC affects soil performance considerably, like the shear strength [2], aqueous diffusion [3], hydraulic conductivity [4] and deformation [5]. At a given water content, the matric suction during drying process is higher than that during wetting process. Thus, SWCCs are hysteretic and include drying SWCCs and wetting SWCCs. The difference between these two types of curves mainly arise from the contact angle hysteresis (the advancing contact angle of liquid on solid surfaces is larger the receding contact angle) [6-8]. Direct measurement of SWCCs is expensive and time-consuming, so researchers prefer to propose models to predict SWCCs and use the measured data to verify their models.

There are three different approaches on the prediction of SWCC, namely empirical methods, domain methods, and theoretical methods. The first approach is the most popular and many empirical models have been proposed. In some empirical models [9-13], SWCC equations containing empirical parameters were proposed and using these equations, the matric suction can be obtained directly once the water content is known. Other empirical models were proposed based on machine learning [14-16] and pedo-transfer functions [17, 18], so SWCC could be predicted from some easy-to-measure soil properties, like the

grain-size distribution [19], pore-size distribution [20] and density of soils [21]. However, the main drawback of the empirical approach is that it does not have a sound theoretical basis, and has substantial uncertainty and variability. The accuracy of these models will decrease if they are used to predict SWCCs of soils having different properties from those in the dataset used in model calibration. The second approach is called the domain method [22-24], and it is assumed that water in soils is stored in spherical pores with different radii. Each pore only has two states, namely water-filled or empty, and a large pore corresponds to a low suction. At a given matric suction, there is one equivalent pore radius, and the corresponding water content in soils is the volume sum of pores whose radius is less than the equivalent pore radius. Due to the 'ink-bottle' effect, during the wetting process, large pores obstruct the water soaking process, and only part of pores with radius less than the equivalent pore radius are filled with water [24-26]. Therefore, at a given suction, the water content for the drying process is larger than that for the wetting process, and the hysteresis of SWCC can thus be captured. However, the domain method cannot show the water distribution in unsaturated soils well. Apart from liquid moisture transfer, vapor transfer also contributes to the moisture migration in soils [27]. Because of thermal gradients, water vapor migrates from the high-temperature area to the low-temperature area to equalize the thermal energy of the two area. Once vapor reaches the cool area, condensation happens. Therefore, the existence of water is independent of the pore size, and it has been observed experimentally that due to adsorption and capillary contributions, water accumulates on the grain surface and around the contact points of grains [28]. The theoretical approach is the most promising to predict the SWCC of soils, and it has gained

increasing attention [29-31]. For example, Beckett & Augarde [32] used a unit cell with hexagonal close-packed structure to describe the microstructure of soils, and the pores in the unit cell were assumed to be spherical. An equation was first used to determine the equivalent pore radius based on a given matric suction, and then the corresponding water content is the volume sum of pores with radius less than the equivalent pore radius, the water bridges and water films in unit cells with pore radius larger than the equivalent pore radius. The thickness of water films was obtained by considering the effect of van der Waals forces. Since drying processes and wetting processes follow different relationships between equivalent pore radius and suction, the SWCC hysteresis could be reflected. Alves et al. [33] used a unit cell with simple cubic structure to describe the soil microstructure. Similar to the last model mentioned, each unit cell was composed of spherical grains with the same radius, and water accumulates around contact points among grains, but water films on grain surfaces were not considered. To consider the grain size distribution, the soil was divided into many fractions based on the grain size. For each fraction, the corresponding SWCC can be obtained based on its unit cell. The SWCC of the soil is the sum of SWCCs corresponding to these grain size fractions. Fu et al. [34] proposed an equivalent liquid bridge model to predict SWCCs of soils. The volume of the liquid bridge between two spheres could be derived from the water content in soils using a proposed expression. Then, based on the Young-Laplace equation, the suction could be obtained. To consider the grain size distribution, the diameter of these two spheres equals the mean size of the soil, which is defined as the sum of the product of percentage content

and minimum size limit of clay, silt, sand and gravel in the soil. By considering the contact angle hysteresis, the SWCC hysteresis was capture.

However, there are still some problems needed to be solved about existing theoretical models on the prediction of SWCC. Firstly, the proposed model should be comprehensive and good for practical application. Most existing models contain empirical parameters, so they are good at fitting, instead of predicting the SWCC. For a good predictive model, every parameter should have clearing physical meaning and their values can be determined based on some easy-to-measure soil properties. For example, Tokunaga [35] considered the effect of van der Waals forces and electric double-layer forces on the water film thickness in soils, so the model is comprehensive. However, in the model, the water film thickness is expressed as a function of matric potential, which is not easy to measure, and this is not good for the practical application. Secondly, the existing equations used to calculate the volume of liquid bridge between two spheres are questionable. In the three theoretical models mentioned above, three different equations are used to calculate the volume of liquid bridge. This means that there is still no volume calculation equation that can be accepted by most researchers. Thirdly, the mean grain size and the sum of SWCCs corresponding to every grain-size fraction do not perform good on the consideration of the effect of grain-size distribution. The size of gravel is over 1000 times larger than that of clays. If the concept of mean grain size is used, the effect of fine grains may be neglected. Similarly, experiments [36] show that suction corresponding to fine grains is over 1000 times larger than that corresponding to coarse grains. Thus, if the SWCC of soils is the sum of SWCCs corresponding to every grain-size fraction, the effect

of coarse grains will be neglected. Last but not least, the existing models cannot show some new findings. Studies have shown that engineering behavior of soils can be better interpreted if the influence of matric suction is considered [37-39], so a good SWCC model should be able to explain some phenomena in soils. For example, it is believed that the swelling of expansive soils is due to the presence of some clay minerals, like Kaolinite, Illite and Montmorillonite [40, 41]. The swelling of these clay minerals in water arises from the repulsive pressure caused by electric double-layer forces [42]. However, it is still uncertain about the shrinkage mechanism of expansive soils at a low water content [27]. If the volumetric change of expansive soils were really controlled by clay minerals, shrinkage should not happen.

In this work, to solve the problems mentioned above, a micromechanics model is proposed to predict the SWCC of unsaturated soils. In the model, every parameter has clear physical meaning and can be determined experimentally. This study is organized as follows. In the next section, a chemical model is proposed to determine the water film thickness in soils and the effects of van der Waals forces and electric double-layer forces are considered. Then, expressions for the volume calculation of the water bridge between two contacted spherical grains are derived, and the SWCC can be obtained by incorporating the liquid bridge model to the representative volume element (RVE) of soils. The contact angle hysteresis is considered to capture the SWCC hysteresis, and the concept of equivalent grain radius is proposed to consider the effect of grain-size distribution. The change of SWCC with the RVE structure is analyzed to illustrate the behavior of soils under wetting-drying cycles. In the result part, several groups of test data

are adopted to verify the validity of the proposed models. By analyzing the model predictions, new mechanisms about the swelling and shrinkage of expansive soils are found. The last section summarizes the main findings.

5.2. Model formulation

5.2.1. Water film thickness on the surface of solids

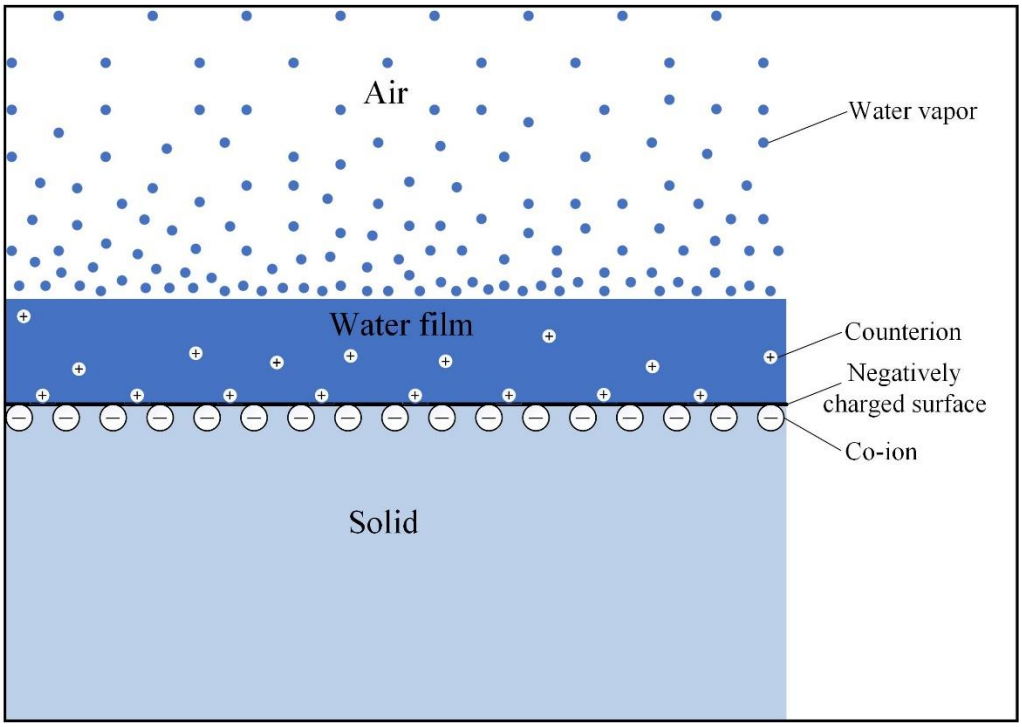

Figure 5.1 Diagram of the stable water film on the flat surface of solids.

The stability of water film on a solid surface is affected by van der Waals forces and electric double-layer forces [43]. In this section, by analyzing the effect of these two types of forces, a new chemical model is proposed to predict the thickness of water film.

For practical applications, the film thickness is expressed as a function of some easy-to-measure parameters, like the temperature, relative humidity, and solid geometry in soils.

5.2.1.1. Effect of van der Waals forces

The van der Waals force between two materials can be attractive or repulsive, and it depends on the dielectric properties of materials. Materials having similar properties in a medium always suffers attractive van der Waals forces, while dissimilar materials in a medium could be attractive or repulsive. For example, if the dielectric constant of the medium is intermediate between those of the two materials, these two materials will be repelled from each other. The van der Waals force per unit area on the air-water interface, as shown in Figure 5.1, can be expressed as:

$$P_{VDW} = -A_{132} / 6\pi d^3 \tag{5.1}$$

with

$$A_{132} = \frac{3}{4} k_B T \left(\frac{\varepsilon_1 - \varepsilon_3}{\varepsilon_1 + \varepsilon_3}\right)\left(\frac{\varepsilon_2 - \varepsilon_3}{\varepsilon_2 + \varepsilon_3}\right) + \frac{3h\nu_e}{8\sqrt{2}} \frac{(n_1^2 - n_3^2)(n_2^2 - n_3^2)}{\sqrt{(n_1^2 + n_3^2)(n_2^2 + n_3^2)}\left[\sqrt{(n_1^2 + n_3^2)} + \sqrt{(n_2^2 + n_3^2)}\right]} \tag{5.2}$$

where A_{132} is the nonretarded Hamaker constant for media 1 (solid) and 2 (air) interacting across medium 3 (water), d the thickness of the water film, ν_e the main electronic absorption frequency in the UV, k_B the Boltzmann constant, T the temperature in Kelvin, n_i and ε_i (i = 1, 2, 3) are the refractive index in the visible and the dielectric constant respectively of phase i. Equation 5.2 works only when the absorption frequencies for the three phases are the same. Here, it is defined that the sign of pressure is positive.

In some cases, combining relations are often used to approximate the Hamaker constant as below.

$$A_{132} \approx (\sqrt{A_{11}} - \sqrt{A_{33}})(\sqrt{A_{22}} - \sqrt{A_{33}}) \tag{5.3}$$

where A_{ii} is the Hamaker constant for two media i interacting across a vacuum. However, combining relations works only when the van der Waal forces dominate the interaction, and they break down when media with high dielectric constants, such as water, are involved. Therefore, Equation 5.3 cannot be used to determine the thickness of the water film as shown in Figure 5.1.

From Equation 5.1, it can be seen that the Hamaker constant is the key to the determination of van der Waals forces. Table 5.1 summarized the values of Hamaker constants for some materials interacting with air across water, and all the materials have negative values for A_{132}. This means the force between the materials and air is repulsive, and this is good for the stability of water film. From Table 5.1, it can be concluded the Hamaker constant in soils may be in the order of 10^{-20} J.

Table 5.1 Hamaker constant determined for media 1 and 2 interacting across medium 3 at room temperature

Medium 1	Medium 3	Medium 2	Hamaker constant A_{132} (10^{-20} J)
Fused silica [44]	Water	Air	-1.03
Calcite [44]	Water	Air	-2.26
Calcium fluoride [44]	Water	Air	-1.23
Soils [45]	Water	Air	-6

Note: A_{132} for soils was determined by fitting adsorption data and the effect of the electric double-layer force was not considered.

5.2.1.2. Effect of electric double-layer forces

Different from van der Waals forces, electric double-layer forces in a medium are always repulsive. The surface of some solids in water is charged, because of the dissociation of some surface groups. For example, the surface of some clay minerals in water can dissociate and give off Na^+, K^+, and Ca^{2+} ions. These cations are called counterions and the anions on the surface are called co-ions (here, we do not consider the effect of the H_3O^+ and OH^- from dissociated water). Electric double-layer forces arise from the osmotic pressure between the counterions, and they force the counterions away from the solid-water interface and from each other.

Based on the Langmuir equation [46], the disjoining pressure arising from electric double-layer forces in the water film can be expressed as

$$P_{el} = \varepsilon_0 \varepsilon (\pi k_B T / ze)^2 / 2d^2 \tag{5.4}$$

where e is the electron charge, z the ion valence, ε_0 (= 8.854×10^{-12} C^2 J^{-1} m^{-1}) the permittivity of free space, and ε (=78.2 at 25°C) the dielectric constant of water.

Therefore, based on the additivity assumption, relative to the atmospheric pressure (1 bar), the pressure imposed on the air-water interface from the solid surface is

$$P_1 = P_{el} + P_{VDW} \tag{5.5}$$

If the surface is flat, the relative pressure can be expressed as a function of relative vapor pressure as below [47].

$$P_2 = -(RT / v)\ln(p_v / p_{sat}) \tag{5.6}$$

where R (= 8.314 $J\cdot(mol\cdot K)^{-1}$) is the Avogadro constant, v the molar volume of water, and p_v and p_{sat} are the vapor pressure in the air and the saturated water vapor pressure.

Therefore, it can be seen that the water film thickness increases with the relative vapor pressure.

However, for grains in soils, they are assumed to be spherical instead of flat in this work. To account for the effect of grain curvature, the relative pressure is expressed as.

$$P_2 = -(RT / v)\ln(p_v / p_{eq}) \tag{5.7}$$

where p_{eq} is the equilibrium vapor pressure.

Since according to the Kelvin equation [47], the relationship between the equilibrium vapor pressure of a liquid and its saturated vapor pressure can be expressed as:

$$p_{eq} = p_{sat} \cdot \exp(\frac{\gamma v \kappa}{RT}) \tag{5.8}$$

where γ is the surface energy density or surface tension of water in air, and κ is the mean curvature of water film and it may be approximated using the curvature of the solid surface.

By substituting Equation 5.8 into Equation 5.7 and based on the force balance, we can obtain

$$P_1 = P_2 = -(RT / v)\ln(p_v / p_{sat}) + \gamma\kappa = -(RT / v)\ln(RH) + \gamma\kappa \tag{5.9}$$

where RH ($=p_v/p_{sat}$) is the relative humidity. Combing Equations 5.5 and 5.9, the water film thickness can be determined, once the Hamaker constant (A_{132}), the ion valence of counterions (z), temperature (T), surface tension of water in air (γ), relative humidity in soils (RH), dielectric constant (ε) and molar volume (v) of water, and the solid surface

curvature (κ) are known. Here, it is defined that the curvature for convex surfaces is positive, while that for concave surfaces is negative.

However, for soils, they contain different minerals, and different minerals have different chemical compositions and different Hamaker constants. This makes the determination of A_{132} and z complicated. To solve this problem, here it is assumed that z equals 1. To determine the value of A_{132}, adsorption data from several groups of soils are used and the constant can be obtained by fitting the test data, as shown in the result part.

5.2.2. Liquid bridge model for two contacted spheres

With the increase of relative humidity from 0, the water film forms on the surface of solids. Then, since the water meniscus around the contact point of two grains is concave ($\kappa < 0$), as shown in Figure 5.2(a), based on Equation 5.8, $p_{eq} < p_{sat}$. Thus, in the vicinity of the concave water meniscus, water vapors in air can reach an over-saturated state easily, and this is good for condensation. Water droplets may form on the surface of grains under dynamic environmental conditions. However, when the system approaches to equilibrium, these water droplets will disappear. That is because these droplets have large curvatures, and this can result in a very high p_{eq}, so they can evaporate easily. Therefore, at equilibrium conditions, with the increase of water content in soils, water accumulates around the contact points of grains.

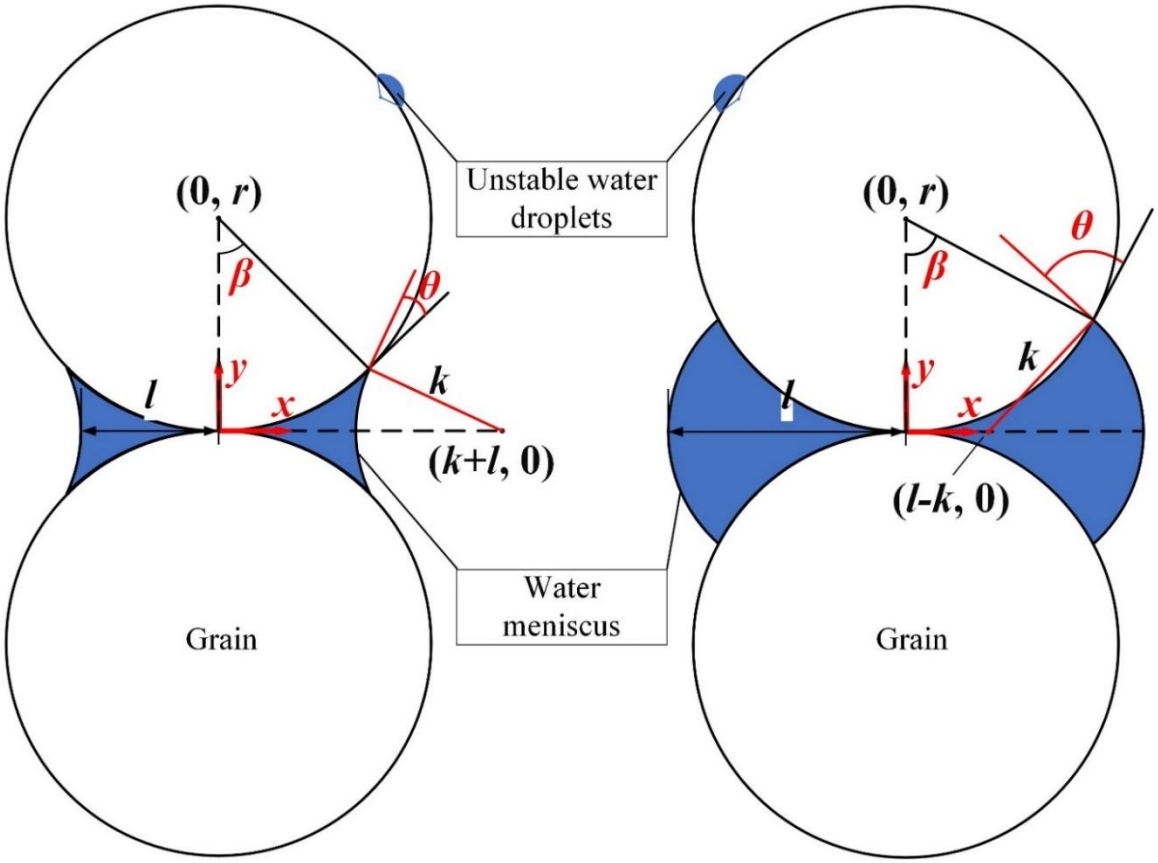

(a) (b)

Figure 5.2 The water distribution around two contacted spherical grains when (a) θ+β < 90°, and (b) θ+β > 90°.

When the water meniscus is concave, as shown in Figure 5.2(a), based on the Young-Laplace equation [48], the capillary pressure or matric suction between these two particles is as below.

$$\psi = u_a - u_w = \gamma(\frac{1}{k} - \frac{1}{l}) \tag{5.10}$$

where u_a and u_w are the atmospheric and water pressures respectively, γ the air-water surface energy density, k (≥ 0) and l (≥ 0) the meniscus radii of curvature.

Based on the shell method, the water volume between two contacted grains can be calculated as below:

$$\begin{aligned} v_w &= 2\int_0^{r\sin\beta} 2\pi x\cdot(r-\sqrt{r^2-x^2})dx - 2\int_l^{r\sin\beta} 2\pi x\cdot\sqrt{k^2-[x-(l+k)]^2}\,dx \\ &= 2\pi r^3\sin^2\beta + \frac{4\pi r^3}{3}(\cos^3\beta-1) + \frac{4\pi}{3}[k^2-(r\sin\beta-l-k)^2]^{3/2} \\ &\quad + \pi(l+k)[2(r\sin\beta-l-k)\sqrt{k^2-(r\sin\beta-l-k)^2}+\pi k^2 \\ &\quad + 2k^2\arcsin(\frac{r\sin\beta-l-k}{k})] \end{aligned} \tag{5.11}$$

with

$$k=\frac{r(1-\cos\beta)}{\cos(\theta+\beta)} \tag{5.12}$$

$$l=r\sin\beta-k+k\sin(\theta+\beta) \tag{5.13}$$

$$r=r_0+d \tag{5.14}$$

where v_w is the volume of water around the contact point, θ the contact angle, r_0 the radius of the spherical grains, d the thickness of the water film and β the angle related to the volumetric water content. Since from the result part it can be seen that the water film thickness is very small compared to the radius of grains even at high relative humidity, it is rational to approximate r using the sum of the grain radius and water film thickness.

From Equations 5.10-5.14, it can be seen that once v_w, θ and r are known, the suction can be determined and the value of β can be obtained based on Equation 5.11. From Equation 5.12, it can be found that the formula only applies to the condition when (θ+β) is less than 90º. Otherwise, k is negative and it is conflict with Equation 5.10. For hydrophilic materials, even though θ is less than 90º, with the increase of volumetric water

content, β increases. Thus, the condition when (θ+β) > 90º exists and it has been observed experimentally [28].

When the water meniscus is convex, as shown in Figure 5.2(b), (θ+β) > 90º and the capillary pressure or matric suction between these two particles is as below.

$$\psi = u_a - u_w = -\gamma(\frac{1}{k} + \frac{1}{l}) \tag{5.15}$$

The volume of water around the contact point can be calculated as below:

$$\begin{aligned} v_w &= 2\int_0^{r\sin\beta} 2\pi x \cdot (r - \sqrt{r^2 - x^2})dx + 2\int_{r\sin\beta}^{l} 2\pi x \cdot \sqrt{k^2 - [x - (l-k)]^2}\,dx \\ &= 2\pi r^3 \sin^2\beta + \frac{4\pi r^3}{3}(\cos^3\beta - 1) + \frac{4\pi}{3}[k^2 - (r\sin\beta - l + k)^2]^{3/2} \\ &\quad + \pi(l+k)[\pi k^2 - 2(r\sin\beta - l + k)\sqrt{k^2 - (r\sin\beta - l + k)^2} \\ &\quad -2k^2 \arcsin(\frac{r\sin\beta - l + k}{k})] \end{aligned} \tag{5.16}$$

with

$$k = -\frac{r(1-\cos\beta)}{\cos(\theta+\beta)} \tag{5.17}$$

$$l = r\sin\beta + k - k\sin(\theta+\beta) \tag{5.18}$$

Similarly, when the water meniscus is convex, based on Equations 5.15-5.18, once v_w, θ and r are known, the suction can be determined and its value is negative. The value of β can be determined using Equation 5.16. Arising from the chemistry and topography of solid surfaces, the advancing contact angle (θ_a) and receding contact angle (θ_r) of liquid on solid surfaces are different, and θ_a is usually larger than θ_r. Therefore, to consider the contact angle hysteresis, when it is wetting, θ_a is used to replace θ in the formula above. When it is drying, θ_r is used to replace θ in the formula.

5.2.3. Microstructure of soils

If the soil is composed of grains with only one size, the soil microstructure can be represented using one type of representative volume element (RVE). The RVE structure can be described using the body-centered cubic (BCC) structure, face-centered cubic (FCC) structure, hexagonal close-packed (HCP) structure or simple cubic (SC) structure, as shown in Figure 5.3.

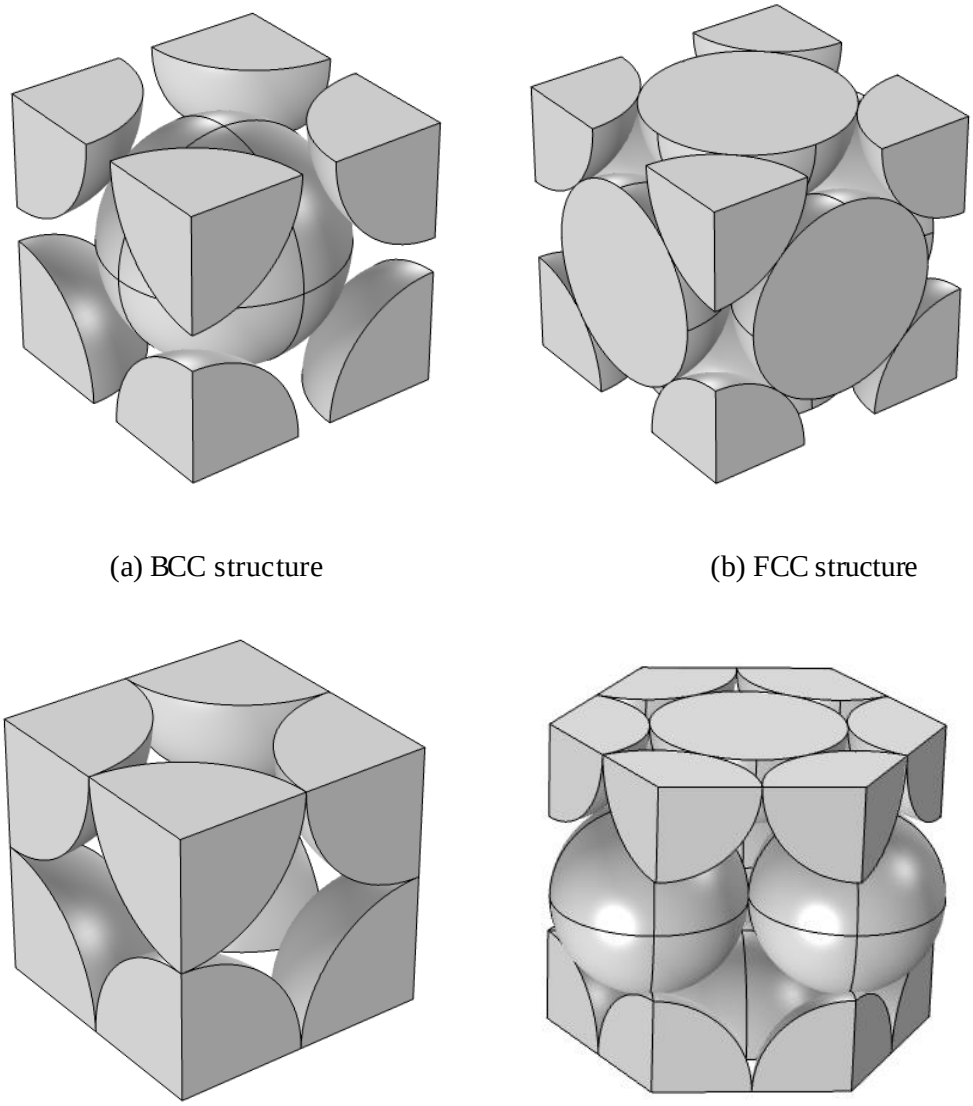

(a) BCC structure (b) FCC structure

(c) SC structure (d) HCP structure

Figure 5.3 Representative volume element structure of soils.

For the BCC structure, as shown in Figure 5.3(a), grains are located at corner and center position. The volume of the RVE is:

$$V = \frac{64 r_0^3}{3\sqrt{3}} \tag{5.19}$$

where r_0 is the radius of the grain.

The total number of grains in the RVE is:

$$N = 2 \tag{5.20}$$

Porosity n is defined as the ratio of the volume of voids to the total volume in the RVE, so the porosity of BCC is as below:

$$n = 0.32 \tag{5.21}$$

The total number of complete contact points is:

$$M = 8 \tag{5.22}$$

Therefore, once the volumetric water content (VWC) in soils is known, the water volume around each contact point (v_w) can be obtained as below. In this work, we assume v_w in each complete contact point is equal.

$$v_w = \frac{VWC \cdot V - V_{w0}}{M} \tag{5.23}$$

with

$$V_{w0} = \frac{4N}{3}\pi[(r_0 + d)^3 - r_0^3] \tag{5.24}$$

where V_{w0} is the volume of water films on the grain surface in the RVE, and it corresponds to the residual volumetric water content.

Thus, once the microstructure of the soil and the contact angles (including advancing angle and receding angle) are known, based on Equations 5.10-5.18, the relationship between v_w and ψ can be determined.

The properties for different RVE structures are summarized in Table 5.2. It can be seen that SC structure has the largest porosity, while FCC and HCP structures have the lowest porosity. It needs to be noted that the above mentioned four types of RVE structure are approximations to the real structure of soils and the most accurate way to determine the RVE of soils is by doing experiments. The microstructure of soils can be described based on the volume, porosity, grain size and number of complete contact points in the RVE.

Table 5.2 Properties of representative volume elements of soils

Microstructure	BCC	FCC	SC	HCP
Volume (V)	$64r_0^3/3\sqrt{3}$	$16\sqrt{2}r_0^3$	$8r_0^3$	$24\sqrt{2}r_0^3$
Number of grains (N)	2	4	1	6
Porosity (n)	0.32	0.26	0.48	0.26
Number of complete contact points (M)	8	24	3	27

Note: BCC: Body-centered cubic; FCC: Face-centered cubic; SC: Simple cubic; HCP: Hexagonal close-packed; r_0: Radius of the grain.

5.2.3.1. Effect of grain-size distribution

A naturally occurring soil sample usually has grains of various size, and based on the size of grains, soils can be divided into gravel, sand, silt and clay. According to the classification of the U.S. department of agriculture, the size of gravels is larger than 2 *mm*; the size of sands is from 0.05 *mm* to 2 *mm*; the size of silt is from 0.002 *mm* to 0.05 *mm*; the size of clay is less than 0.002 *mm*. The grain-size distribution of coarse-grained soils is determined by sieve analysis, and these grains are larger than 0.075 *mm*. For fine-grained soils, hydrometer analysis is used for determination of the grain-size distribution, and it is based on the principle of sedimentation of soil grains.

To consider the grain-size distribution, a concept of equivalent grain radius is proposed as below:

$$r_{eq} = 10^{x_{eq}} / 2 \tag{5.25}$$

with

$$x_{eq} = \sum_i c_i \cdot \log_{10}(L_i) \tag{5.26}$$

where r_{eq} is the equivalent grain radius in soils, L_i is the size of the i_{th} sieve, and c_i is the percentage of soils retained on the i_{th} sieve. Standardization can be realized by taking the logarithm to the grain or sieve sizes, and by taking the average of standardized sizes, the effect of very small grains can be considered.

If a soil contains several types of RVE, the matric suction of the soil can be expressed as:

$$\Psi = \sum_{j=1}^{4} p_j \psi_j(r_{eq}) \tag{5.27}$$

where j represents the type of RVE structure, and 1, 2, 3, 4 represent BCC, FCC, SC, HCP respectively; p_j represents the percentage of RVE structure type j in the soil and $\sum_{j=1}^{4} p_j = 1$; ψ_j represents the matric suction in a RVE with structure type j.

5.2.3.2. Evolution of the RVE structure

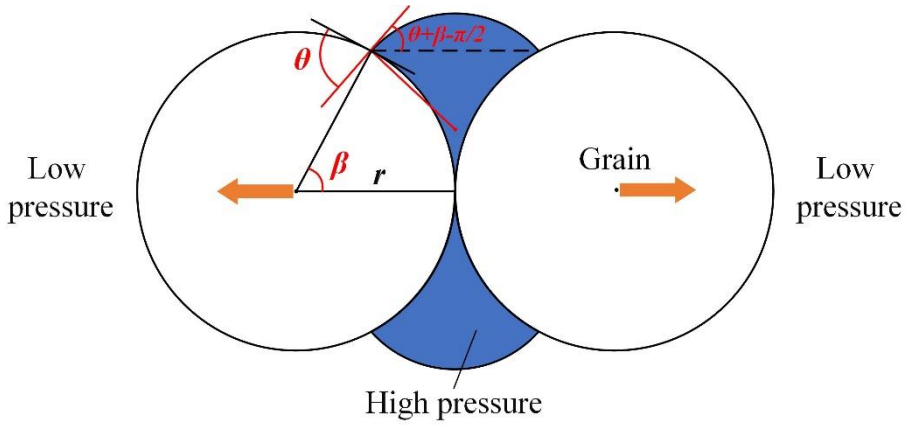

Figure 5.4 Separation of two contacted grains because of the negative matric suction.

As will be seen in the result, for fine-grained soils, when they approach to be saturated, the matric suction is negative and the pressure difference can force contacted particles separated. Figure 5.4 shows the separation of two contacted particles. Water pressure pushes two particles outwards, while surface energy pulls these two particles inwards. Therefore, the net force between two contacted grains is as below:

$$\begin{aligned} F &= (u_w - u_a)\cdot\pi(r\sin\beta)^2 - 2\pi r\sin\beta\cdot\gamma\cos(\theta+\beta-\frac{\pi}{2}) \\ &= \pi r\sin\beta\cdot[(u_w - u_a)r\sin\beta - 2\gamma\cdot\sin(\theta+\beta)] \end{aligned} \tag{5.28}$$

Therefore, if we do not consider forces from the surrounding, when F >0, these two grains start to separate. Separation may also happen between two contacted grains with a concave water meniscus. As shown in Equation 5.10, when $k > l$, the matric suction is negative, so the separation criterion can be obtained based on the procedure above.

Although during drying, high positive matric suction will bound particles together, the chaos increases with the increase of the wetting-drying cycle number, based on the second law of thermodynamics. It has been observed experimentally that wetting-drying cycles can increase the porosity of soils [49, 50]. Therefore, every wetting-drying cycle can be regarded as a process of rearrangement of grains, and the RVE structure of soils may be different in different wetting-drying cycles. This can explain the change of the soil water characteristic curve after wetting-drying cycles.

5.3. Results

5.3.1. Water film thickness

To determine the value of Hamaker constant (A_{132}) of soils and verify the validity of the water film thickness model proposed, some test data [51, 52] are adopted. These data were collected by Or and Tuller [45], and they obtained the value of A_{132} by fitting the data using a film adsorption equation they proposed. They found the water film thickness in soils with mixed clay minerals could be described by a single A_{132}. However, in their model, the effect of electric double-layer forces on the water film thickness is not considered. In this part, we follow the same procedure as that of Or and Tuller to determine the value of A_{132} in the proposed model by fitting test data. As shown in Table 5.3, the data set is composed of six groups of soils, so the data set is representative in terms of grain-size distribution and soil textures.

Table 5.3 Measured soil composition and properties [45]

Soil series	Sand	Silt	Clay	Clay minerals	Porosity
L-Soil [52]	0.888	0.061	0.051	Mixed	0.45
Royal [52]	0.536	0.319	0.145	Mixed	0.48
Walla Walla [52]	0.228	0.633	0.139	Mixed	0.52
Millville [51]	0.330	0.490	0.180	Mixed	0.47
Palouse [52]	0.113	0.682	0.205	Mixed	0.55
Palouse B [52]	0.093	0.439	0.468	Mixed	0.59

Table 5.4 Values of parameters used in the model prediction

Property	Value	Property	Value
Saturated vapor pressure (p_{sat})	3169 Pa	Water surface tension (γ)	72 mN/m
Hamaker constant (A_{132})	-3.5×10^{-20} J	dielectric constant (ε)	78.2
Ion valence (z)	1	water molar volume (v)	18.07 cm^3/mol
Temperature (T)	25ºC	Radius of spherical solids (r_0)	1 mm

Figure 5.5 shows the comparison between test data and model predictions on the water film thickness, and values of parameters used during model prediction are summarized in Table 5.4. It can be seen that when A_{132} equals -3.5×10^{-20} J, the model prediction matches the test data well, and a single A_{132} is able to describe the change of the water film thickness with vapor pressure in soils. The value of A_{132} obtained is less than the value ($A_{132}=-6\times10^{-20}$ J) obtained by Or and Tuller [45]. That is because we considered the effect of both van der Waals forces and electric double-layer forces. In the model prediction, it is assumed that soils are composed of spherical grains with radii equal 1mm. To verify the effect of grain size on the water film thickness, parameter analysis is done, as shown in Figure 5.6. It can be seen that when the relative humidity (RH) is less than 0.99, the effect of grain size on the water film thickness is negligible. This may explain why a single A_{132} applies to soils with different gradations. From Figure 5.6(b), it can be seen that when RH is higher than 0.99, the effect of grain size on the film thickness

increases and cannot be neglected. The water film thickness also increases with the increase of the grain size.

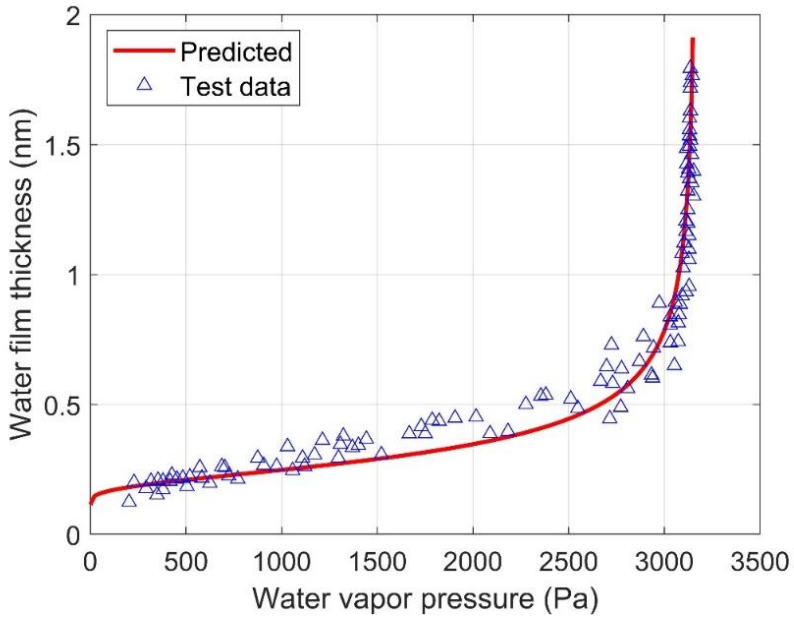

Figure 5.5 Comparison between test data [45] and model prediction on the change of water film thickness with water vapor pressure in soils.

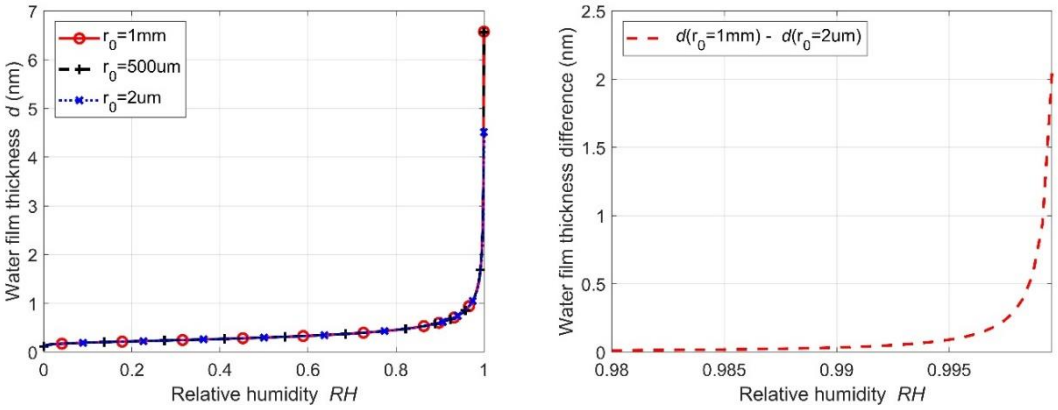

(a) (b)

Figure 5.6 Effect of grain size on the water film thickness.

5.3.2. SWCC

To verify the validity of the proposed model on the prediction of SWCC, test data from a literature [53] is adopted. In the literature, the relationships between gravimetric water content and matric suction of five types of soils were measured, and the gradations for the soils are shown in Figure 5.7. These soils were classified as CL (lean clay with sand), ML (sandy silt), SC (clayey sand with gravel), SM (silt sand with gravel), and GW-GM (well-graded gravel with silt and sand) based on ASTM D2487 [54]. In this work, the measured relationship between gravimetric water content and matric suction is converted to that between volumetric water content and matric suction using the equation below.

$$w = \frac{VWC \cdot \rho_w}{\rho_d} \tag{5.29}$$

where VWC is the volumetric water content, w the gravimetric water content, ρ_w the density of water and ρ_d the dry density of soil. The test data about ρ_d of these five types of soils are summarized in Table 5.5.

It is assumed the relative humidity of these soils is 99%, and the temperature is 25ºC. The equivalent grain radius can be obtained based on their gradation using Equation 5.25. Since the RVE structures and contact angles of these soils were not analyzed, it is assumed that these five types of soils have the same microstructure, but have different contact angles. The soil properties are summarized in Table 5.5, and comparison between model predictions and test data is shown in Figure 5.8. Although the good match between model predictions and test data is achieved by adjusting the contact angle and accuracy of model prediction is not verified due to the lack of information about the microstructure

and contact angle of soils, it shows that the proposed model has the ability to capture the SWCC of soils.

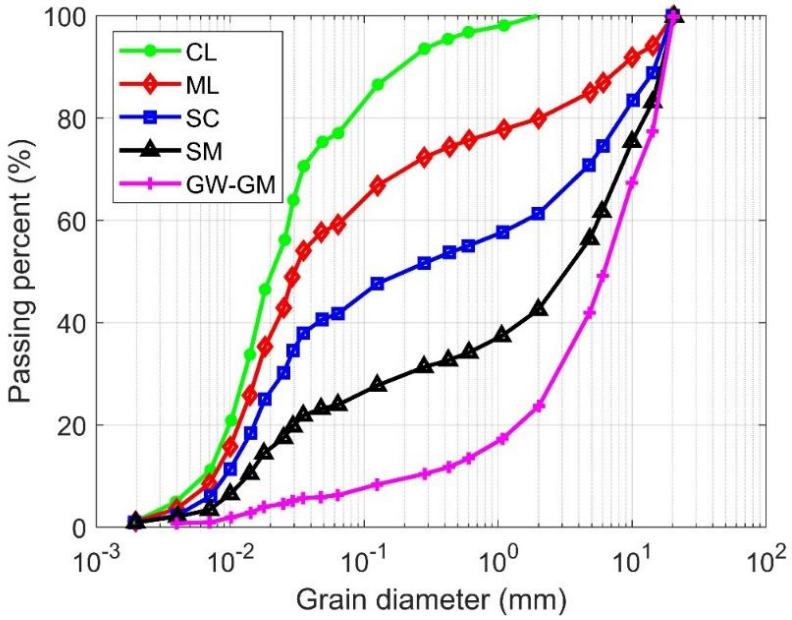

Figure 5.7 Gradation of five types of soils [53].

Table 5.5 Soil properties.

Soil name	Dry density [53] (kg/m^3)	Equivalent grain radius r_{eq} (mm)	Contact angle(°)	RVE volume V (cm^3)	RVE porosity	Complete contact points number in RVE
CL	1550	0.0108	10	0.0101	0.6	13
ML	1710	0.0365	26	0.389	0.6	13
SC	1900	0.1204	28	14.0	0.6	13
SM	1970	0.3939	28	488.9	0.6	13
GW-GM	1950	1.3185	41	18337.1	0.6	13

Note: $V = 8r_{eq}^3$.

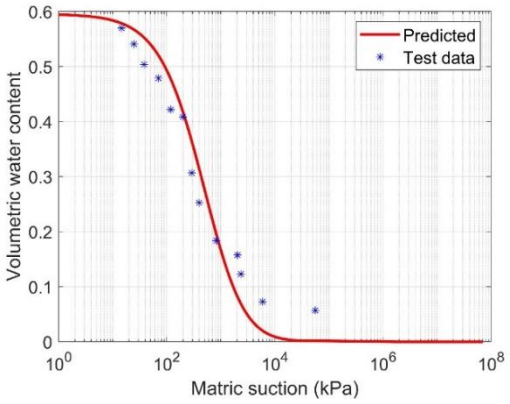

(a) CL

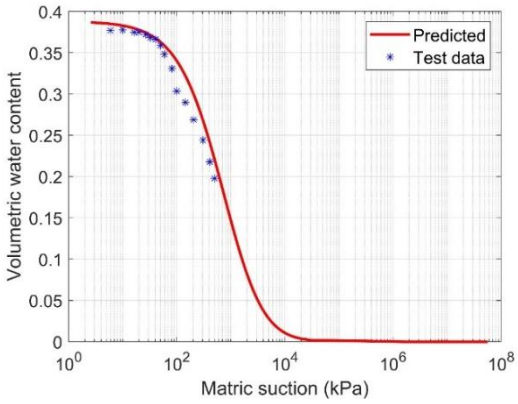

(b) ML

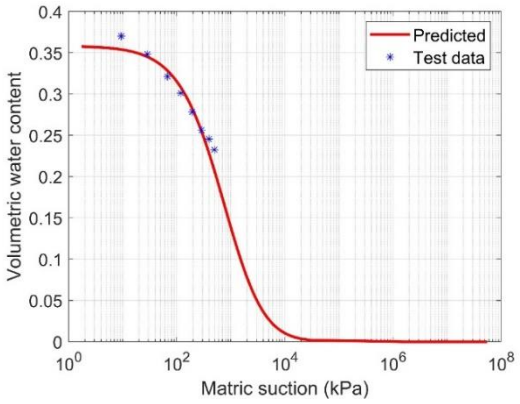

(c) SC

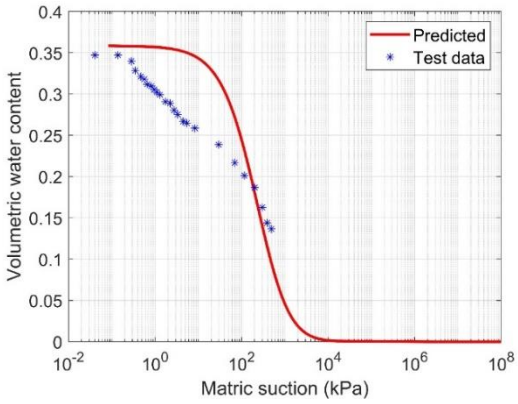

(d) SM

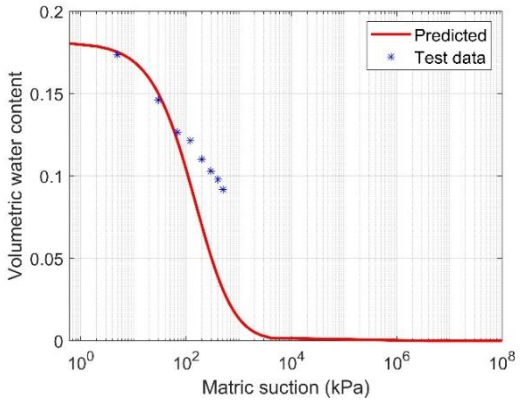

(e) GW-GM

Figure 5.8 Comparison between test data [53] and model predictions.

The effect of equivalent grain radius, contact angle and microstructure of soils on the SWCC are studied by doing parametric analysis. Figure 5.9 shows SWCCs of soils with different grain sizes and contact angles. By comparing curves (r_{eq}=2μm, θ = 10º) and (r_{eq} =2μm, θ = 30º), or curves (r_{eq} =500μm, θ = 10º) and (r_{eq} =500μm, θ = 30º), it can be seen that a large contact angle can lead to a low suction. The curve with a low θ can represent the drying curve, while the curve with a large θ can represent the wetting curve. At a given water content, the suction corresponding to the drying curve is larger than the wetting curves. It shows that the proposed model can capture the SWCC hysteresis. It can also be seen that with the increase of the grain size, the matric suction decreases. This coincides with experimental observations. For example, suction can pull water up a larger distance in a small-radius tube than that in a large-radius tube.

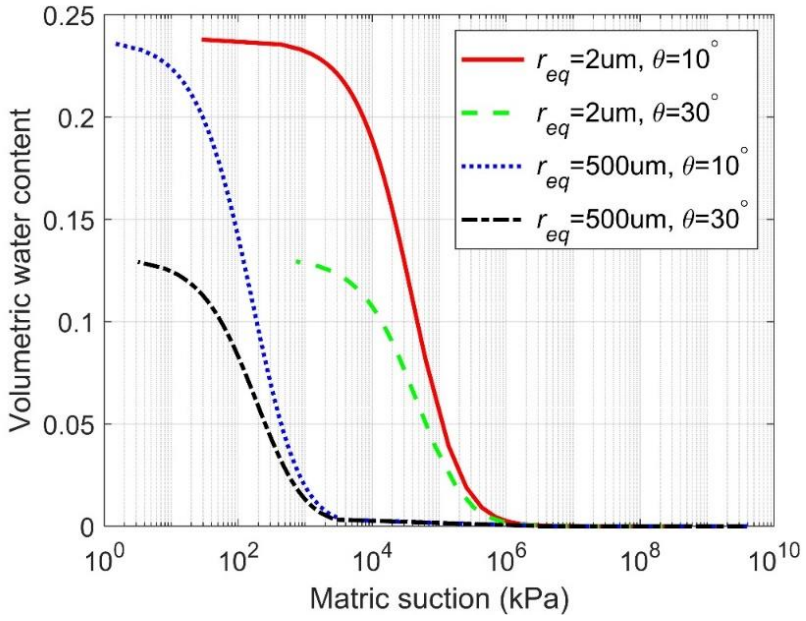

Figure 5.9 Soil-water characteristic curves for soils with BCC structure and γ equal 72mN/m.

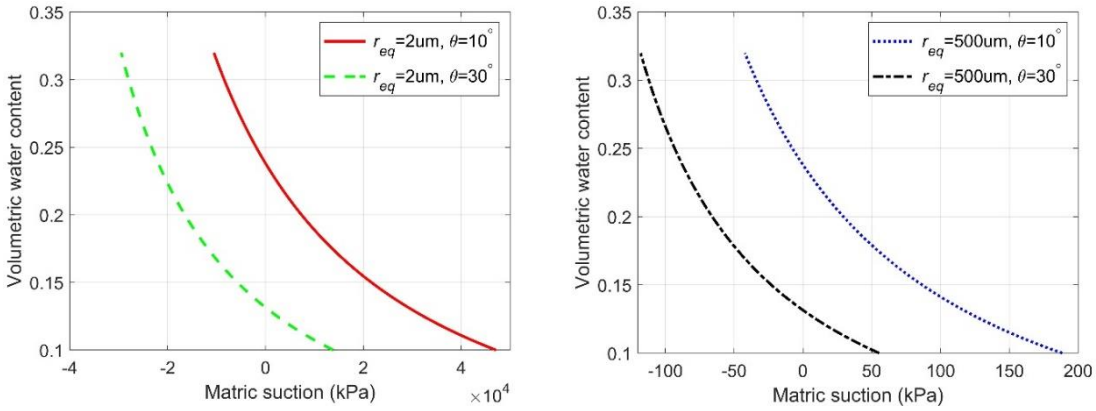

(a) (b)

Figure 5.10 Soil-water characteristic curves for soils with BCC structure and γ equal 72mN/m when the soils approach to be saturated. (a) r_{eq}=2μm; (b) r_{eq}=500μm.

Since in Figure 5.9, the scale of the abscissa is in logarithm, only predictions with positive suction values can be plotted. Figure 5.10 shows the change of matric suction when the soil approaches to be saturated. A negative matric suction means the pressure within the water meniscus (u_w) is larger than the atmospheric pressure (u_a), and if the pressure difference is large enough, two contacted grains can be separated. By comparing Figures 5.10(a) and 5.10(b), it can be found that when the soil approaches to be saturated, (u_w - u_a) decreases with the increase of the grain size or with the decrease of the contact angle. This can explain the swelling and shrinking mechanisms of expansive soils. Expansive soils contain incredibly fine particles. When they approach to be saturated, extremely large pressure difference (u_w - u_a) forces contacted grains separated, which can lead to swelling. When they are drying out, the matric suction is extremely large, as shown in Figure 5.9, so it causes the shrinkage. Such large suction also explains why it is difficult to drain expansive soils.

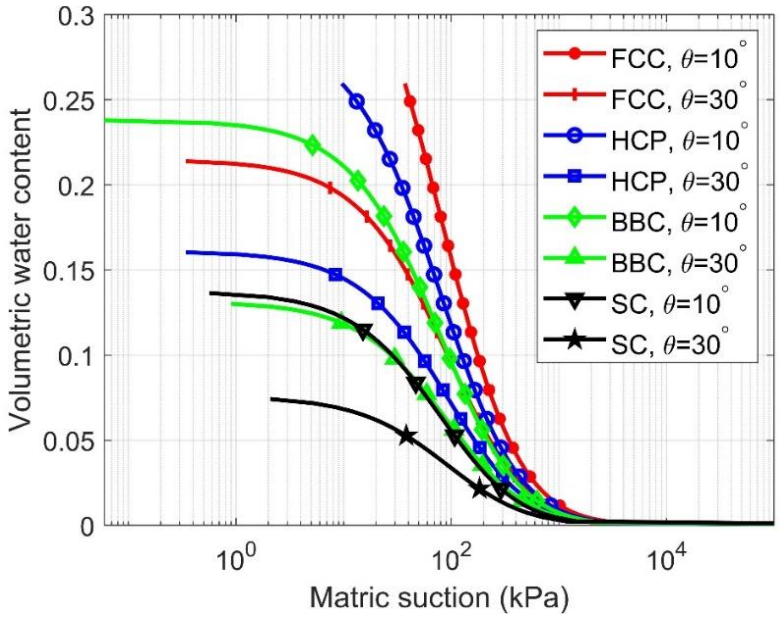

Figure 5.11 Soil-water characteristic curves for soils with different RVE structure and contact angles (r_{eq} = 1mm and γ =72mN/m).

Figure 5.11 shows SWCCs for soils with different RVE and contact angles. By comparing the results for FCC, BBC and SC, it can be found that with the increase of the porosity, the predicted SWCC moves downwards. This has been verified by many phenomena that a high porosity can cause a low suction. For example, because of the suction, the water from underground can move to the ground surface, and to prevent the loss of water, farmers usually loose soils to prevent the evaporation by increasing the soil porosity. Since wetting-drying cycles can increase the porosity of soils, this means the proposed model is capable of capturing the suction decrease after wetting-drying cycles by considering the change of soil RVE structure. In addition, experiments [55] show that at the same suction, the volumetric water content corresponding to a high normal stress is higher than that corresponding to a low net normal stress. A high net normal stress can

cause a low porosity, and from Figure 5.11, it can be concluded that the proposed model can capture the experimental observation well. By comparing SWCCs for FCC and HCP, it can be seen that although the HCP structure has more complete contact points, the slope for HCP is lower that for FCC. That is because the RVE volume of HCP is larger than that of FCC. When the volumetric water content is the same for both structures, the water volume around every contact point in HCP is larger than that in FCC, and the matric suction between contacted grains decreases with the increases of water volume around the contact point.

5.4. Summary

A chemical model is first proposed to determine the adsorbed water film thickness on the grain surface by considering the effect of van der Waals forces and electric double-layer forces. The film thickness can be determined through some easy-to-measure variables, like the relative humidity, water surface tension in air and solid surface curvature. Then, a micromechanics model is proposed to predict the SWCC of soils. The expression for water volume and suction between two contacted spherical grains are derived, and by studying the microstructure of soils, the SWCC can be obtained. Main findings are summarized as below:

(1) The proposed water film thickness model and SWCC model are practical. Every parameter in the models has clear physical meaning and is measurable easily.

(2) The effect of grain size on the water film thickness is negligible when the relative humidity is less than 99%, and the film thickness is in the order of nanometer.

(3) The proposed SWCC model can capture the performance of soils well. It is shown that the huge positive and negative matric suction is responsible for the shrinkage and expansion of expansive soils, which contains very small particles.

(4) Matric suction increases with the decrease of grain size and contact angle of water in soils.

(5) The decrease of matric suction after wetting-drying cycles arises from the change of soil microstructure, and matric suction decreases with the increase of porosity.

In the future, the microstructure of soils and contact angle of water in soils will be further studied.

5.5. References

[1] D.G. Fredlund, H. Rahardjo, Soil mechanics for unsaturated soils, John Wiley & Sons, 1993.

[2] D.G. Fredlund, A. Xing, M.D. Fredlund, S. Barbour, The relationship of the unsaturated soil shear strength to the soil-water characteristic curve, Canadian geotechnical journal 33(3) (1996) 440-448.

[3] P. Lim, S. Barbour, D. Fredlund, The influence of degree of saturation on the coefficient of aqueous diffusion, Canadian geotechnical journal 35(5) (1998) 811-827.

[4] Y. Mualem, A new model for predicting the hydraulic conductivity of unsaturated porous media, Water resources research 12(3) (1976) 513-522.

[5] J. Kim, W. Hwang, Y. Kim, Effects of hysteresis on hydro-mechanical behavior of unsaturated soil, Engineering Geology 245 (2018) 1-9.

[6] D. Mampallil, Some physics inside drying droplets, Resonance 19(2) (2014) 123-134.

[7] W.J. Likos, R. Jaafar, Pore-scale model for water retention and fluid partitioning of partially saturated granular soil, Journal of Geotechnical and Geoenvironmental Engineering 139(5) (2013) 724-737.

[8] L. Gao, T.J. McCarthy, Contact angle hysteresis explained, Langmuir 22(14) (2006) 6234-6237.

[9] D. Karube, K. Kawai, The role of pore water in the mechanical behavior of unsaturated soils, Geotechnical & Geological Engineering 19(3) (2001) 211-241.

[10] K. Kawai, S. Kato, D. Karube, The model of water retention curve considering effects of void ratio, Unsaturated Soils for Asia, CRC Press2020, pp. 329-334.

[11] M. Feng, D. Fredlund, Hysteretic influence associated with thermal conductivity sensor measurements, Proceedings from Theory to the Practice of Unsaturated Soil Mechanics in Association with the 52nd Canadian Geotechnical Conference and the Unsaturated Soil Group, Regina, Sask 14(2) (1999) 14-20.

[12] D.G. Fredlund, A. Xing, Equations for the soil-water characteristic curve, Canadian geotechnical journal 31(4) (1994) 521-532.

[13] L. Kong, H.M. Sayem, H. Tian, Influence of drying–wetting cycles on soil-water characteristic curve of undisturbed granite residual soils and microstructure mechanism by nuclear magnetic resonance (NMR) spin-spin relaxation time (T 2) relaxometry, Canadian Geotechnical Journal 55(2) (2018) 208-216.

[14] A. Baghbani, T. Choudhury, S. Costa, J. Reiner, Application of artificial intelligence in geotechnical engineering: A state-of-the-art review, Earth-Science Reviews 228 (2022) 103991.

[15] Y. Li, S.K. Vanapalli, Prediction of soil-water characteristic curves using two artificial intelligence (AI) models and AI aid design method for sands, Canadian Geotechnical Journal 59(1) (2022) 129-143.

[16] Y. Li, S.K. Vanapalli, Prediction of Soil–Water Characteristic Curves of Fine-grained Soils Aided by Artificial Intelligent Models, Indian Geotechnical Journal (2022) 1-13.

[17] H. Bayat, B. Mazaheri, B.P. Mohanty, Estimating soil water characteristic curve using landscape features and soil thermal properties, Soil and Tillage Research 189 (2019) 1-14.

[18] J.P. Wang, N. Hu, B. François, P. Lambert, Estimating water retention curves and strength properties of unsaturated sandy soils from basic soil gradation parameters, Water Resources Research 53(7) (2017) 6069-6088.

[19] M.D. Fredlund, G.W. Wilson, D.G. Fredlund, Use of the grain-size distribution for estimation of the soil-water characteristic curve, Canadian Geotechnical Journal 39(5) (2002) 1103-1117.

[20] P. Simms, E. Yanful, Predicting soil—water characteristic curves of compacted plastic soils from measured pore-size distributions, Géotechnique 52(4) (2002) 269-278.

[21] M. Wijaya, E. Leong, Modelling the effect of density on the unimodal soil-water characteristic curve, Géotechnique 67(7) (2017) 637-645.

[22] L. Yao, S.K. Vanapalli, Models for predicting the soil-water characteristic curves for coarse and fine-grained soils, Journal of Hydrology 612 (2022) 128248.

[23] R. Braddock, J.Y. Parlange, H. Lee, Application of a soil water hysteresis model to simple water retention curves, Transport in Porous Media 44(3) (2001) 407-420.

[24] Y. Mualem, A conceptual model of hysteresis, Water resources research 10(3) (1974) 514-520.

[25] Q. Zhai, H. Rahardjo, A. Satyanaga, G. Dai, Y. Du, Estimation of the wetting scanning curves for sandy soils, Engineering Geology 272 (2020) 105635.

[26] H.Q. Pham, An engineering model of hysteresis for soil-water characteristic curves, University of Saskatchewan, 2001.

[27] F.H. Chen, Foundations on expansive soils, Elsevier, 2012.

[28] S. Lourenço, D. Gallipoli, C.E. Augarde, D.G. Toll, P.C. Fisher, A. Congreve, Formation and evolution of water menisci in unsaturated granular media, Géotechnique 62(3) (2012) 193-199.

[29] L. Guo, T. Li, G. Chen, P. Yu, X. Peng, D. Yang, A method for microscopic unsaturated soil-water interaction analysis based on DDA, Computers and Geotechnics 108 (2019) 143-151.

[30] P. Zhang, L. Tang, L. Jiang, Z. Deng, Research of quantitative relations of matric suction with water content and dry density, Chinese Journal of Rock Mechanics and Engineering 32(S1) (2013) 2792-2797.

[31] X. Wang, J. Li, A novel liquid bridge model for estimating SWCC and permeability of granular material, Powder Technology 275 (2015) 121-130.

[32] C.T. Beckett, C.E. Augarde, Prediction of soil water retention properties using pore-size distribution and porosity, Canadian Geotechnical Journal 50(4) (2013) 435-450.

[33] R.D. Alves, G. de FN Gitirana Jr, S.K. Vanapalli, Advances in the modeling of the soil–water characteristic curve using pore-scale analysis, Computers and Geotechnics 127 (2020) 103766.

[34] Y. Fu, H. Liao, X. Chai, Y. Li, L. Lv, A Hysteretic Model Considering Contact Angle Hysteresis for Fitting Soil-Water Characteristic Curves, Water Resources Research 57(4) (2021).

[35] T.K. Tokunaga, Physicochemical controls on adsorbed water film thickness in unsaturated geological media, Water Resources Research 47(8) (2011).

[36] A.S.S. Raghuram, B.M. Basha, A.A.B. Moghal, Effect of fines content on the hysteretic behavior of water-retention characteristic curves of reconstituted soils, Journal of materials in civil engineering 32(4) (2020) 04020057.

[37] A.J. Puppala, S.S. Congress, A. Banerjee, Research advancements in expansive soil characterization, stabilization and geoinfrastructure monitoring, Frontiers in geotechnical engineering, Springer2019, pp. 15-29.

[38] A. Banerjee, A.J. Puppala, U.D. Patil, L.R. Hoyos, P. Bhaskar, A simplified approach to determine the response of unsaturated soils using multistage triaxial test, IFCEE 20182018, pp. 332-342.

[39] W. Wray, B. El-Garhy, A. Youssef, Three-dimensional model for moisture and volume changes prediction in expansive soils, Journal of Geotechnical and Geoenvironmental Engineering 131(3) (2005) 311-324.

[40] S. Asuri, P. Keshavamurthy, Expansive soil characterisation: an appraisal, INAE Letters 1(1) (2016) 29-33.

[41] A. Zhou, J. Du, X. Lin, Y. Bu, J. Kodikara, Nanoscale mechanism on lime stabilization of expansive soil, Acta Geotechnica (2022) 1-21.

[42] B.M. Das, B. Das, Advanced soil mechanics, Taylor & Francis New York, 2008.

[43] J.N. Israelachvili, Intermolecular and surface forces, Academic press, 2011.

[44] D.B. Hough, L.R. White, The calculation of Hamaker constants from Liftshitz theory with applications to wetting phenomena, Advances in Colloid and Interface Science 14(1) (1980) 3-41.

[45] D. Or, M. Tuller, Liquid retention and interfacial area in variably saturated porous media: Upscaling from single-pore to sample-scale model, Water Resources Research 35(12) (1999) 3591-3605.

[46] I. Langmuir, The adsorption of gases on plane surfaces of glass, mica and platinum, Journal of the American Chemical society 40(9) (1918) 1361-1403.

[47] W. Thomson, 4. On the equilibrium of vapour at a curved surface of liquid, Proceedings of the Royal Society of Edinburgh 7 (1872) 63-68.

[48] T. Young, III. An essay on the cohesion of fluids, Philosophical transactions of the royal society of London (95) (1805) 65-87.

[49] L.F. Pires, K. Reichardt, M. Cooper, F.A. Cássaro, N.M. Dias, O.O. Bacchi, Pore system changes of damaged Brazilian oxisols and nitosols induced by wet-dry cycles as seen in 2-D micromorphologic image analysis, Anais da Academia Brasileira de Ciências 81 (2009) 151-161.

[50] L.F. Pires, O.O. Bacchi, K. Reichardt, Gamma ray computed tomography to evaluate wetting/drying soil structure changes, Nuclear instruments and methods in physics research section B: beam interactions with materials and atoms 229(3-4) (2005) 443-456.

[51] D. Or, R. Hanks, Soil water and crop yield spatial variability induced by irrigation nonuniformity, Soil Science Society of America Journal 56(1) (1992) 226-233.

[52] G. Campbell, S. Shiozawa, Prediction of hydraulic properties of soils using particle-size distribution and bulk density data, Indirect methods for estimating the hydraulic properties of unsaturated soils (1992) 317-328.

[53] L. Zhang, X. Li, Microporosity structure of coarse granular soils, Journal of Geotechnical and Geoenvironmental Engineering 136(10) (2010) 1425-1436.

[54] ASTM Committee D-18 on Soil and Rock. Standard Practice for Classification of Soils for Engineering Purposes (Unified Soil Classification System) 1. ASTM international, 2017.

[55] G.A. Miller, C.N. Khoury, K.K. Muraleetharan, C. Liu, T.C. Kibbey, Effects of soil skeleton deformations on hysteretic soil water characteristic curves: Experiments and simulations, Water Resources Research 44(5) (2008).

6. CONCLUSIONS

In this work, three energy-based models and one micromechanics model are proposed. The energy-based models are used to predict the fatigue cracking happened in the asphalt concrete layer and rutting occurred in the asphalt concrete layer and base layer. Compared with stress or strain based models, the energy-based models are independent of the loading mode. Therefore, the parameter values determined using strain-controlled test data apply to the stress-controlled loading condition. The micromechanics model is used to predict the soil-water characteristic curve. Compared with existing SWCC models, the micromechanics model proposed has the potential to predict the SWCC, rather than fit the SWCC. That is because every parameter in the proposed model has a clear physical meaning and is measurable easily.